Tip-Enhanced Near-Field Scattering and Photothermal Expansion in Observing Light-Matter Interaction at Nanoscale

by

Haomin Wang

A Dissertation

Presented to the Graduate and Research Committee

of Lehigh University

in Candidacy for the Degree of

Doctor of Philosophy

in

Department of Chemistry

Lehigh University

August 2020

Approved and recommended for acceptance as a dissertation in partial fulfillment of the requirements for the degree of Doctor of Philosophy

Haomin Wang
Tip-Enhanced Near-Field Scattering and Photothermal Expansion in Observing Light-Matter Interaction at Nanoscale

07/17/2020

Defense Date

Dissertation Director
Prof. Xiaoji Xu

Approved Date

Committee Members:

Prof. Xiaoji Xu

Prof. Dmitri Vezenov

Prof. Nathan Wittenberg

Prof. Xiaohui Frank Zhang

ACKNOWLEDGMENTS

I started my Ph. D. career as a fresh college graduate in 2015 when I was 22 and first set foot on the continent of America. Around that time, I met Xiaoji, who later become my advisor. I also met a bunch of same-year classmates and colleagues in Lehigh, and become close friends with some of them. Just escaped from a gloomy undergraduate life, things at that time were all sugar-coated. During my first year in Lehigh, I had a lot of free time to spend with my friends exploring this new land, learning how to drive a car, buying things with old-school checks, applying for my first credit card, purchasing my first gaming console using my first paycheck… At that time, I would never imagine becoming a hard-working Ph. D. candidate who would spend 10+ hours a day in the lab in most days of a year, finishing up the Ph. D. degree with a 100+ pages dissertation.

But here I am, after a 5-year journey which converted me from who simply sought the Ph. D. career as a getaway to who cherish and acknowledge this journey, during which many beautiful things have been lost, yet many meaningful things have been gained. It was hard to tread a long and boring trip alone, with so many peers in either America or my home country who had already left the school and started to chase lives that look colorful and vibrant. Gradually, I started to get used to how heavy the Ph. D. degree means, and this heaviness is nontrivial at all. It is so fair that to feel the pleasure of exploring science, advancing technologies, and a sense of accomplishment, one must sacrifice more or less in other aspects of life. What I could do, after all, was to try my best to engrave my name on one plaque.

I am extremely thankful for people who provided guidance and support along this journey, including my advisor Xiaoji and my academic committee members Prof. Dimitri Vezenov, Prof. Nathan Wittenberg, and Prof. Xiaohui Frank Zhang. Your engagements and

proficiencies have guided me on the right track and shaped this dissertation. Moreover, I thank Prof. Dmitri Vezenov, who taught me rigorous physical chemistry through classes and other formal and informal interactions. This experience did not only enrich my knowledge base, but also inspired me to work hard to become a rigorous and meticulous researcher. Especially, I cannot say enough thanks to my advisor Xiaoji, who continuously taught me knowledge and skills since the day I joined the Xu lab. Many works presented in this dissertation were born from his brilliant ideas. I appreciate the enthusiasm for research that he has and hope I can get that enthusiasm in the future, too.

The majority of this dissertation was written up during the self-quarantine period caused by the COVID-19 pandemic. Paradoxically, I felt more connected with people during the pandemic than the normal time, when I was too busy to keep in touch with whom I love. I acknowledge these people who support me during this uncertain time, including my mother and father, my family members, and several old best friends from college and high school. I heard a lot of good words from you and your support is extraordinarily helpful for me during this time and is very much appreciated. I am courageous to confront any hurdles on the road with your help and support.

For hurdles that are not controllable by individuals, such as the global pandemic and many other bad things happening right now, the 5-year Ph. D. training taught me to keep an open mind, pinpoint major problems, and act wisely. Most importantly, it taught me to keep calm when things get out of control. For that, let me finish this part with famous lyrics from the old song Que Sera Sera:

“Que Será, Será. Whatever will be will be. The future’s not ours to see. Que Será, Será”.

Haomin Wang
06/01/2020
At Saucon Village

Table of Contents

List of Figures

APPENDICES

List of Tables

ABSTRACT

The Nobel Prize in Physics was awarded to Gerd Binnig and Heinrich Rohrer in 1986 for the invention of scanning tunneling microscope. Soon after, inventions of a host of scanning probe techniques followed the success of scanning tunneling microscope. For the first time, achieving atomic-level imaging and manipulating single atoms become unparalleled feasible, as evidenced by a series of famous images of single atoms from the IBM lab. The core of scanning probe methods is to scan a sharp tip over a sample surface. The idea is straightforward: to measure the small sample, one needs a spatial ruler with an even smaller scale. Spatial resolution in most scanning probe methods is directly correlated with the tip radius, which now can be routinely fabricated down to one nm. For tips with metallic coating, an end radius of 20-30 nm is what one often gets.

Remarkably, when shining light onto a metallic tip, the light-field is "squeezed" close to the sharp apex with a large enhancement factor. The spatial confinement of the tip-enhanced light field is often sub-wavelength and depends on the tip radius as well. In this case, the tip is not only a spatial detector but also a lightning rod, bringing up new capabilities of measuring light-matter interactions. With the tip-enhanced sub-wavelength focus spot, the spatial scale of traditional light spectroscopy can be reduced to the nanoscale. This scale reduction is especially beneficial for longer wavelength applications such as infrared to overcome Abbe's diffraction limit.

One of the major goals of this dissertation is to review combinations of infrared spectroscopy and the scanning probe methods, and understand how the tip-enhanced light field is utilized in such combinations to detect nanoscale light-matter interactions. In light of recent technical breakthroughs, our work on developing novel *in situ* spectro-microscopy techniques, which spanned five years at Lehigh University, is also introduced,

demonstrated, and discussed. Along the way, nanoscale responses to the tip-enhanced light field are illustrated by an abundance of colormap images and pinpoint spectra that reveal light-matter interactions in unprecedented details.

This doctoral dissertation is composed of 5 chapters and two appendices, which are arranged as follows:

Chapter 1 contains introductory materials that are useful for understanding the generation of the tip-enhanced light field. Basic formula and properties of surface plasmons are reviewed. One of the most-used simulation tools in the field of nanoplasmonics is introduced. The end of Chapter 1 deals with the photothermal effect, which is vital for the mechanical detection of light absorption.

In Chapter 2, the working mechanism of atomic force microscopy is reviewed. In addition, technical combinations of the tip-enhanced light field with different working modes of the atomic force microscopy and their pros and cons are introduced and discussed. In the end, limitations of current techniques are discussed.

In Chapter 3, our invention of peak force scattering near-field optical microscopy is introduced in detail. The major advantage of this novel technique over current scattering near-field microscopies is the ability to measure optical nearfields in 3D directly. This unique capability is demonstrated in characterizing polaritonic materials, which is covered throughout the chapter. The work introduced in Chapter 3 has been published as Wang, Haomin, *et al. Nature Communications,* 2018, 9.1: 1-11. and Wang, Haomin, *et al. Nanoscale*, 2020, 12, 1817-1825.

In Chapter 4, our invention of liquid-phase peak force infrared microscopy is introduced. Two technical obstacles for achieving nanoscale infrared spectroscopy in the liquid phase are discussed at the beginning. Later, our ways to overcome these obstacles are presented.

Demonstration of the liquid-phase peak force infrared microscopy is performed on polymer blends, proteins, yeast cell wall particles, and polaritonic materials. Part of the work introduced in Chapter 4 has been published as Li, Wenqian, Wang, Haomin, *et al*. *Langmuir*, 2020. and Wang, Haomin *et al*. *Nano Letters,* 2020, *20* (5), 3986-3991.

At last, Chapter 5 presents several technical improvements of current optical scanning probe methods, including the utilization of a low-repetition-rate laser and a stabilized device for interferometric detection in scattering-type scanning near-field optical microscopy, and implementation of peak force visible microscopy. Part of the work introduced in Chapter 5 has been published as Wang, Haomin, *et al*. *Nature Communications,* 2016, 7.1: 1-8.

Technical details of building and running peak force scattering-type near-field optical microscopy and liquid-phase peak force infrared microscopy are included in Appendix I and Appendix II.

Chapter 1 Tip-Enhanced Light Field: Formation and Application

In this chapter, phenomena and basic principles of plasmonic enhancement will be introduced. Plasmonic enhancement originates from surface plasmons, which are coherent and collective oscillations of electrons usually formed at the interface between dielectrics and metals. Surface plasmons can squeeze the light field into a tiny volume that spans in the nanoscale and significantly enhance the local field intensity. The short-wavelength and high-intensity nature of localized surface plasmons serve as the keystone in techniques that utilize the plasmonic-enhanced light field. Importantly, the tip-enhanced light field can probe nanoscale light-matter interactions with much higher resolution than the optical diffraction limit. In the last section, the photothermal effect, which is vital for signal generation in techniques based on detecting thermal expansions induced by the tip-enhanced field, is reviewed.

1.1 A review of surface plasmons

The world people live in is filled with all kinds of light-matter interactions. Some light-matter interactions are intuitive for our cognition, including reflection, refraction, and absorption – all of which can be described superficially by straight light rays or simple equations. Other light-matter interactions, such as new color generation in nonlinear optics, are not so intuitive. Surface plasmons are among these not-so-intuitive processes, not only because the idea of "squeezing" light field is impossible with the ray interpretation of light, but also due to the lack of visible evidence by human eyes.

The presence of surface plasmons can be revealed by examining Maxwell equations at a planar interface between two media with dielectric functions of $\varepsilon_1(\omega)$ and $\varepsilon_2(\omega)$, as shown

in Figure 1.1. In order to obtain interface waves that propagate along the interface, $\varepsilon_1(\omega)$ and $\varepsilon_2(\omega)$ have to satisfy the following relationship:[1]

$$\varepsilon_1(\omega)\varepsilon_2(\omega) < 0, \text{ and } \varepsilon_1(\omega) + \varepsilon_2(\omega) < 0 \qquad \textbf{(1.1)}$$

If we consider the light propagating from the air onto a metal, with $\varepsilon_1(\omega) = 1$, Equation 1.1 means that $\varepsilon_2(\omega)$ must be negative. It turns out that many metals that can be described by free-electron gas models have negative real parts of dielectric functions in the visible spectrum, which explains why surface plasmons were first experimentally demonstrated on aluminum and magnesium in 1959.[2,3] Nonetheless, surface plasmons are not only limited to metals. As Equation 1.1 suggests, surface plasmons can be formed when $\varepsilon_2(\omega) < 0$, the condition is also true for semiconductors and 2D materials, in the spectrum that ranges from visible to THz.[4] At a relatively large interface shown in Figure 1.1, surface plasmons have a non-zero wavevector along the interface. These traveling surface plasmons are often denoted as surface plasmon polaritons (SPPs).

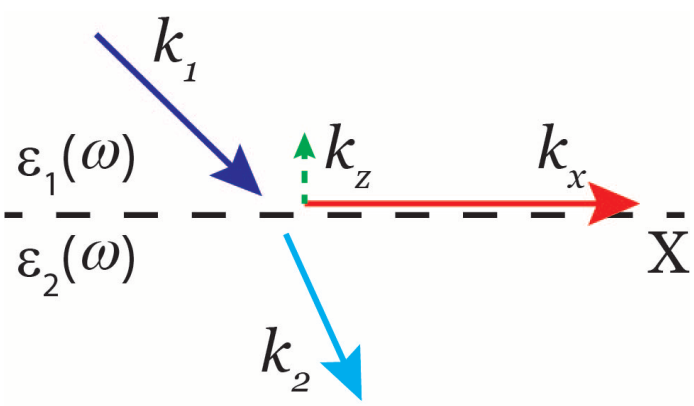

Figure 1. 1 Schematics of the interface between two media with dielectric functions $\varepsilon_1(\omega)$ and $\varepsilon_2(\omega)$. Electromagnetic wave propagations are represented by wavevectors k. Surface plasmons propagation can be separated into two directions: in-plane (k_x) and out-of-plane (k_z). For surface plasmons to present, k_x must be real and k_z must be imaginary.

Surface plasmons can also be generated in a localized manner without propagation. These plasmons are localized surface plasmons (LSPs). In LSP generation, the size of the interface is at the nanoscale and is smaller than the incident wavelength. As a result, surface plasmons manifest as collective vibrations of free-electron gas of individual nanostructures. Figure 1.2 illustrates and compares the formation of SPP and LSP. SPP and LSP are similar in many aspects, as LSP is the solution from Maxwell equations for bounded nanostructures. One significant difference between SPP and LSP is the ability of spatially confining the light field. In the case of SPP, polaritons can travel up to tens of microns in the planar direction and decays in the perpendicular direction with 1/e decay length about 200 nm.[5,6] In comparison, LSP generation can further confine the light field into a region with the size comparable to that of the nanostructure. Although there is a lack of analytical or empirical formulae for the decay length of LSPs, experimentally observed decay lengths of LSPs are 40-50 times shorter than that of SPPs.[7] For example, the light field can be focused on a small volume of 10 nm by impinging on a silver nanoparticle with a 20-nm diameter.[8] Therefore, LSP is more effective for "squeezing" the light field into a small volume than SPP.

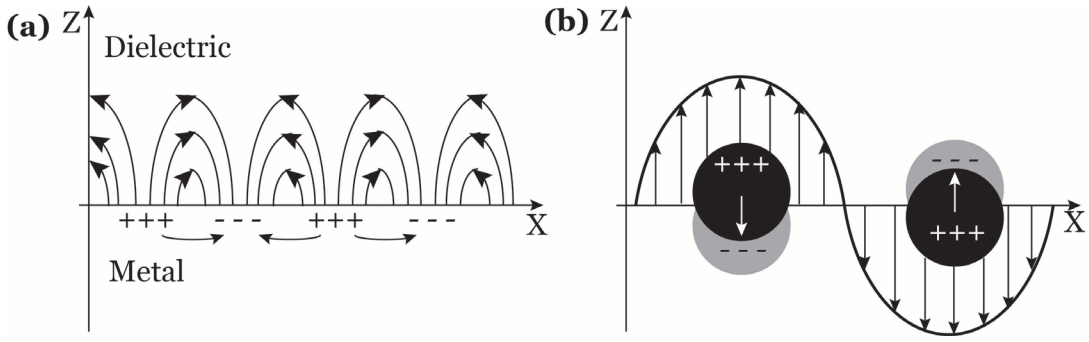

Figure 1. 2 Comparison between SPP and LSP. SPP at a planar interface is illustrated in (a), and LSP between two adjacent nanoparticles is shown in (b). Arrowheads indicate the direction of the electric field. Charge distributions are indicated by "+" and "-." The figure is reproduced from literature[7].

1.2 Plasmonic enhancement – calculation and simulation

Compared with incident light field or photons, two traits of surface plasmons – the short-wavelength property and the ability to confine light field – are apparent. It is worthwhile to understand these properties from a theoretical point of view, as it gives out clear pictures of both SPP and LSP.

Again, we can write down the Maxwell equation for the interface:[1]

$$\nabla^2 E(r,\omega) - \frac{\omega^2}{c^2}\varepsilon(r,\omega)E(r,\omega) = 0 \qquad \textbf{(1.2)}$$

in which r is the cartesian coordinate ($r = (x, y, z)$), ω is the frequency of incident light, c is the speed of light, E is the electric field, and ε is the dielectric function. As shown in Figure 1.1, we consider a 2D Y-normal plane that is perpendicular to the interface between media 1 and 2. As a result, $\varepsilon(r,\omega) = \varepsilon_1(\omega)$ if $z > 0$ and $\varepsilon(r,\omega) = \varepsilon_2(\omega)$ if $z < 0$. For P-polarized (that is, polarized in the image plane of Figure 1.1) light field, E_1 and E_2 in two media can each be decomposed into two subfields that lie along the direction of X and Z, and are written as:

$$E_j = E_{j,x}e^{ik_x x - i\omega t} + E_{j,z}e^{ik_{j,z}z} \quad \text{with} \quad j = 1,2 \qquad \textbf{(1.3)}$$

Here, SPPs share the wavevector k_x along the interface, $k_{j,z}$ represents for wavevectors of surface plasmons traveling along the Z-direction. By applying proper boundary conditions in solving Equation 1.2, we obtain the formula for k_x:

$$k_x = \sqrt{\frac{\varepsilon_1(\omega)\varepsilon_2(\omega)}{\varepsilon_1(\omega) + \varepsilon_2(\omega)}}\frac{\omega}{c} \qquad \textbf{(1.4)}$$

Equation 1.4 describes the dispersion relation of SPPs. If we set $\varepsilon_1(\omega) = 1$ for the air/vacuum, and use Drude-modeled dielectric function of gold for $\varepsilon_2(\omega)$,[1,9] the dispersion relation of SPP in gold can be drawn in Figure 1.3.

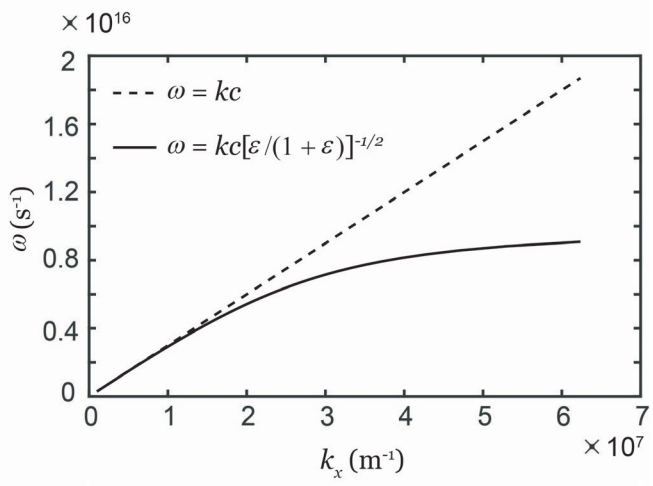

Figure 1. 3 Dispersion relation of SPP in gold. The dispersion relation of the light in the air/vacuum is illustrated with the dashed line.

As Figure 1.3 shows, k_x of SPPs is larger than the k in air/vacuum; in other words, the long wavelength of light in air/vacuum is shortened in SPPs. This trend is preserved and exaggerated in the case of LSPs, although discretized dispersion relations (e.g. dipolar mode and quadrupolar mode for nanoparticles) are usually found for LSPs within nanostructures.[10-12] Multiple modes corresponding to the specific geometry of nanostructures in the dispersion relation of LSP are present.

SPPs are collective vibrations of electrons that travel along a relatively large interface and do not confine the light field as much as LSPs do. For a small plasmonic particle with radius a far less than the wavelength of light, its behavior under the illumination can be modeled as an electric dipole, and the light field outside the particle along the dipolar axis is dominated by the polarizability α:[4,13]

$$\alpha = 4\pi a^3 \frac{\varepsilon - \varepsilon_m}{\varepsilon + 2\varepsilon_m} \qquad \textbf{(1.5)}$$

In Equation 1.5, ε is the dielectric function of the material, and ε_m is the dielectric constant of the surrounding medium. The polarizability α is maximized when ε reaches to $-2\varepsilon_m$,

which is fulfilled in different spectral regions for different materials. The situation is called localized surface plasmon resonance (LSPR). In this case, A large polarizability α corresponds to a greatly enhanced field intensity around the nanoparticle. For examples, enhancement factors of 10^4 for the field intensity are routinely achieved around isolated nanoparticles.[14] For metals, this condition is met in the visible spectrum, which makes metal nanostructures suitable for visible-range plasmonic applications.

LSPs are utilized in a number of plasmonic devices, many of which are composed of individual nanoparticles such as nanospheres, nanopolyhedrons, nanocore-shells, nanoframes, and periodical nanostructures such as nanopillars, nanoneedles, and nanorods.[4,15] To characterize field enhanced hotspots caused by LSPR from complicated geometries, numerical simulation methods are widely applied in the field. One of the popularly used methods is finite-difference time-domain (FDTD), which was developed by Kane S. Yee in 1966.[16] FDTD separates the simulation region into many small lattices (Yee lattices) and solves Maxwell differential equations in a leap-frog algorithm for each discretized lattice until convergence has been achieved.[17] Although details of the FDTD algorithm are complicated, the workflow of FDTD solver is straightforward: First, constructing a nanostructure of interest. For periodic plasmonic arrays, this structure could be a single repeat unit. Second, meshing the FDTD simulation region into small grids. At last, finalizing simulation parameters before starting the FDTD simulation. Several commercial-available programs specialize in FDTD simulation of plasmonics, Lumerical FDTD provided by Lumerical incorporation is one of them. Using Lumerical FDTD software, one can adjust and customize the geometry and the material of the nanostructure, light source properties, as well as boundary conditions in a graphical interface. In this way, the FDTD simulation is simplified as an input-output process through a black box. Figure 1.4 displays a simulation window of a gold nanoparticle with

a diameter of 100 nm in Lumerical FDTD, and the simulation result showing the field enhancement induced by LSPR. An enhanced dipolar field along the light polarization is present. The use of simulation tools can help calculate and illustrate the effect of plasmonic enhancement and provide confirmatory information to experimental results.

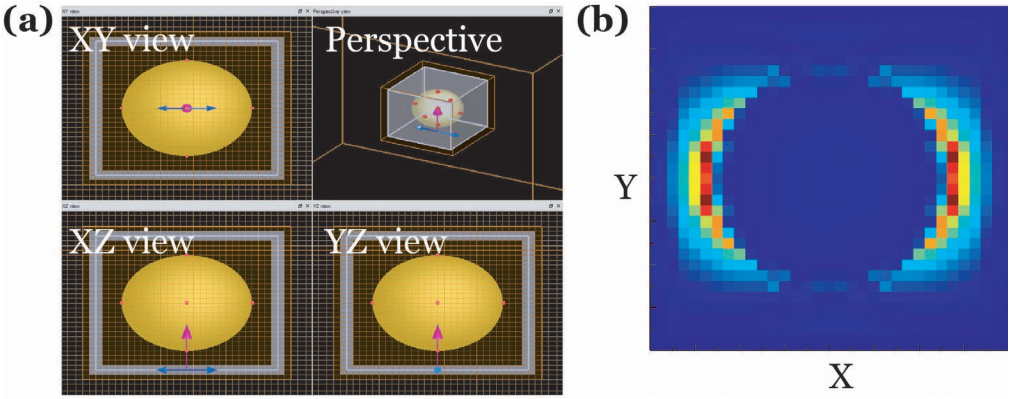

Figure 1. 4 An example of an FDTD simulation using Lumerical FDTD software.The simulation geometry from different view angles is shown in (a). The object is a gold nanosphere with a diameter of 100 nm. Yellow grids indicate the mesh. The light direction is shown by the red arrow, with blue arrows indicating the polarization. The 502 nm light is propagating toward +Z, with the polarization in the XY plane. FDTD-simulated colormap (in the XY plane at Z = 0) of the light field around the nanosphere is shown in (b).

1.3 Plasmonic enhancement in bypassing the diffraction limit

In 1873, German physicist Ernst Abbe discovered the optical diffraction limit: No matter how delicate the optical instruments are, an optical system such as an optical microscope cannot resolve features with dimensions less than half of the light wavelength.[18] The optical diffraction limit can be understood by thinking of a length measurement process: to measure something short, one needs a ruler with a shorter scale. However, the focus spot is always diffracted limited due to the diffraction nature of the light, objects with sizes less than the focus spot cannot be resolved using traditional optical microscopic methods.

Otherwise, if one could "squeeze" the light field into a smaller volume than the focus spot, a better spatial resolution would be achieved.

Such a small light field volume is naturally fulfilled by the plasmonic enhancement of LSP. This effect is sketched in Figure 1.5. LSPs in an array of nanostructures have been utilized to not only bypass the optical diffraction limit, but also provide excellent sensing capabilities from the strong confined light field. For example, in surface enhanced Raman scattering (SERS), originally small Raman signal can be enhanced by factors of 10^6-10^7 by using rough metal substrates that support LSPs.[19] By using resonance enhancement, the enhancement factor for SERS signal can be further boosted up to 10^{15}.[20]

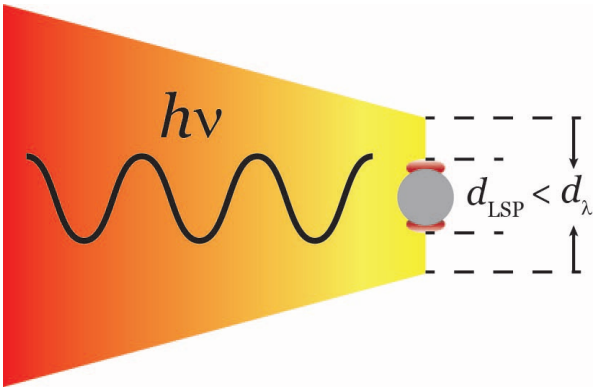

Figure 1. 5 Reduction of the volume of light field. The light field is focused on a plasmonic particle. The field distribution caused by LSP has a spot size d_{LSP} that is comparable to that of the nanoparticle and is smaller than the diffracted limited spot size of d_λ.

The spatial confinement due to LSPs is more eminent for infrared (IR) than visible light, given the longer wavelength in the IR region. On the other hand, light-matter interactions in the IR region contain rich information about molecular vibrations. They thus have been widely used in identifying chemical compositions and states of biological groups.[21] Besides, phonon polaritons, dielectrics' counterpart to SPPs in metals, are often observed and investigated in mid-infrared.[22] To reach a high spatial resolution in IR imaging and spectroscopy, a convenient way is to use the intense light field around nanoparticles as a

local emitter in exciting and even detecting light-matter interactions. The only problem remains, from the viewpoint of instrument design, is how to maintain the LSP field enhancement in a stable and reproducible way in measuring other nanoscale objects. In other words, in measuring complex samples that have different nanoscale features, one would expect that the small volume of the enhanced light field can be freely moved to approach to and detach from nanoscale features of interest.

The problem is solved by using a tiny metallic tip as the plasmonic nanostructure in atomic force microscopy (AFM).[23] The advantages of using AFM are in three aspects. First, AFM has one of the highest spatial resolutions among many state-of-the-art techniques. Its resolution is mostly determined by the tip geometry, which can be engineered either mechanically or chemically to achieve the atomic resolution. Therefore, AFM can easily map out the nanoscale morphology of the sample, which is a good reference point for further investigations on light-matter interactions. Second, the AFM tip coated with metals is an excellent plasmonic nanostructure for confining and enhancing the light field, especially at its sharp apex. This effect is shown by an FDTD simulation of the light field around a conical gold tip in Figure 1.6. When the light polarization matches the axis of the AFM tip, an intense and confined light field is formed right underneath the tip. The confined light field around tapered plasmonic nanostructures is often dubbed as "nearfield" in optics, due to its evanescent nature with a short decay range (less than the wavelength of light). At last, AFM has a variety of working schemes, and many of them allow precise control of the tip position in all 3 directions in space.

Currently, major types of methods that utilize a scanning tip-enhanced optical nearfield include tip-enhanced Raman spectroscopy (TERS),[24] scattering-type scanning near-field optical microscopy (s-SNOM),[25] photothermal induced resonance (PTIR) microscopy,[26] photoinduced force microscopy (PiFM) [27] and peak force infrared (PFIR) microscopy.[28] In

these techniques, the optical diffraction limit is overcome and often surpassed by factors of hundreds. Except for TERS, all techniques above were proposed to study linear IR-induced light-matter interactions. Thus, they are often referred to as AFM-IR. These IR nanoimaging/spectroscopy methods and our representative works in the PFIR-related instrument development will be introduced in detail in the following Chapters.

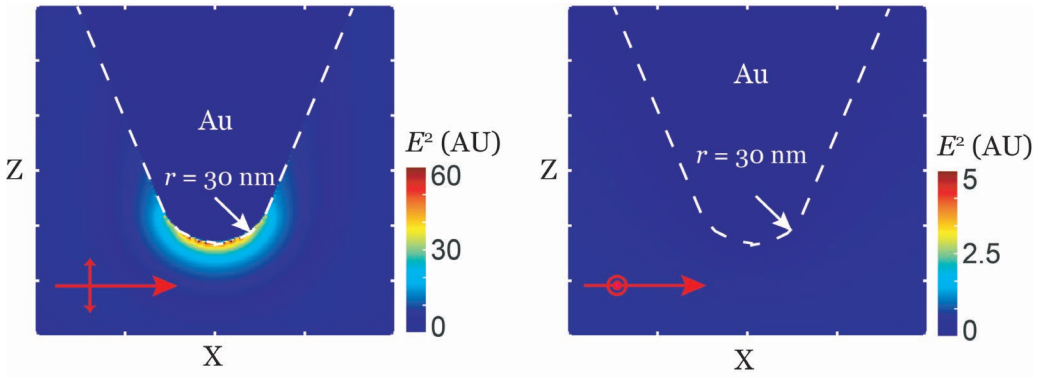

Figure 1. 6 Tip-enhanced light field. The left panel shows the strong tip-enhanced light field (nearfield) at the apex of a conical gold tip with an end radius $r = 30$ nm in the air. This field confinement is induced by a P-polarized 7-μm IR light (simulated as a plane wave) propagating from the left. The propagation and the polarization direction are indicated by red arrows. The right panel shows the same FDTD simulation result when the IR light is S-polarized.

1.4 Photothermal effect

Three general phenomena are associated with energy transfer in light-matter interactions: scattering, emission, and absorption. In light absorption, the absorbed light energy is converted to thermal energy through various nonradiative relaxation routes. Such processes give rise to a variety of photothermal effects including refractive index change, absorbance change, photoacoustic wave generation, temperature increase, and photothermal expansion.[29] The magnitude of many photothermal effects is proportional to the incident light intensity. For example, the proportionality between the photothermal expansion and the intensity of incident field has been revealed and studied for both bulk

and nanoscale materials in various theoretical and experimental studies.[30-32] This proportionality ensures that the magnitude of photothermal expansion can be approximated by assessing the local intensity of the light field. Later, we will see how signals in general AFM-IR methods are also linked to this estimation.

The short time scale of photothermal expansion is important for its applications. In the case of plasmonic nanoparticles, the relaxation time of heat dissipation is on the scale from ps to ns.[33,34] For nanoscale objects, the simulated relaxation time of thermal expansion is on the order of ns.[35] This time scale is fairly short compared with that of the detection event in AFM-IR. In various AFM-IR methods, the speed of detection is mainly limited by the resonance frequency of the cantilever, which is usually in hundreds of kHz. The time scale of the detection event is thus on the scale of μs. The short time scale of photothermal expansion enables to detect the photothermal expansion as a "steady" state in AFM-IR. Except for s-SNOM, signal generations in commonly used methods of AFM-IR (PTIR, PiFM, PFIR) have been demonstrated to originate from the photothermal expansion.

Upon absorption, the light energy is transferred into the sample. Inside the sample, an enhanced light field is generated, which later turns into thermal energy, and a portion of heat manifests as photothermal expansion. However, the photothermal expansion has never been experimentally revealed in AFM-IR, due to the small expansion of only tens of pm.[31] Instead, we can monitor the enhanced field that is generated inside the sample, and use the intensity of that field as a measure of photothermal expansion since they are proportional to each other.

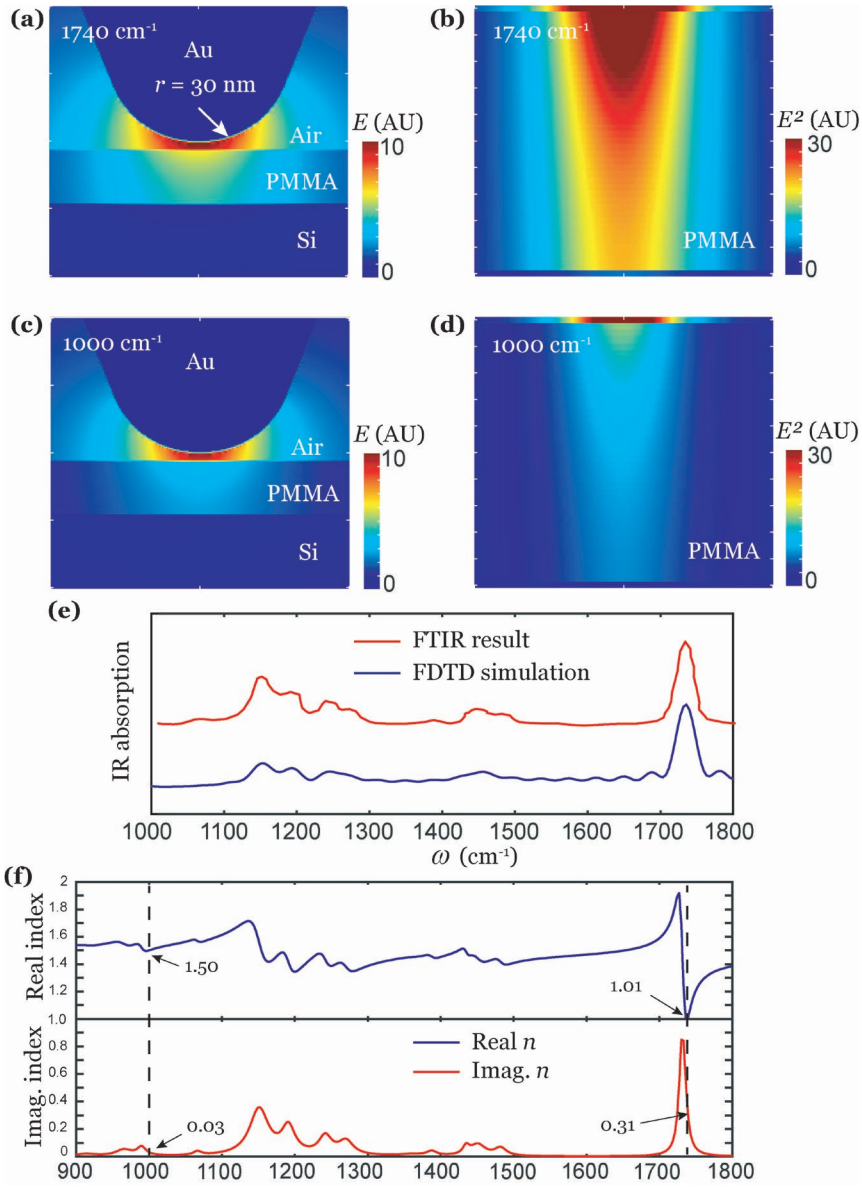

Figure 1. 7 Mechanism of signal generation in photothermal expansion based AFM-IR methods is illustrated by FDTD simulation. Simulation results of the field amplitude are shown in (a) and (c) at 1740 cm^{-1} (absorbing) and 1000 cm^{-1} (non-absorbing), zoomed-in images of the field intensity inside the 20-nm PMMA layer are shown in (b) and (d), respectively. IR spectrum is simulated by collecting transmission data at a monitor plane inside PMMA (which is 1-nm under the PMMA top surface) and compared with the experimental FTIR spectrum in (e). FTIR spectrum of PMMA is reproduced from literature[36]. The real and imaginary parts of the refractive index of PMMA used in the

simulation are plotted in (f). Dashed lines indicate two wavenumbers used in FDTD simulations used in (a-b).

In Figure 1.7, an FDTD simulation is executed to extract the field intensity inside a 20-nm film of poly(methyl methacrylate) (PMMA), when it is put close to a gold conical tip. At a non-absorbing frequency, a small intensity is present inside PMMA; at an absorbing frequency, an intense field is formed within the sample. The plot of light transmission inside PMMA vs. incident frequency overlaps well with the IR absorption of PMMA, since the imaginary part (the lossy term) of the dielectric function of PMMA [37] is accounted for in the FDTD calculation. Figure 1.7 is important, as it mimics the energy distribution that leads to the photothermal expansion, and demonstrates the chemical sensitivity of AFM-IR methods that are based on detecting the photothermal expansion. An empirical formula is then proposed for the signal S in PTIR, PiFM, and PFIR:

$$S \propto \alpha_s(\omega) I_{inc} \tag{1.6}$$

in which $\alpha_s(\omega)$ is the absorption coefficient of the sample, and I_{inc} is the incident field intensity. Equation 1.6 is the basis of studying the sample's IR property using general AFM-IR methods.

Chapter 2 Realization of Tip-Enhanced Light Field through Atomic Force Microscope

In this chapter, working mechanisms of AFM and general AFM-IR techniques, including s-SNOM, PTIR, and PiFM will be explained and discussed. Although the tip-enhanced light field is employed in all methods, different AFM-IR techniques utilize various AFM working schemes and detection methods, leading to different mechanisms of signal generation. Because of these variances, s-SNOM is often used to detect optical near-field properties, such as surface plasmons and phonon polaritons. In contrast, PTIR and PiFM are usually used to identify IR absorption properties. At the end, limitations of these techniques will be discussed.

2.1 Working modes in atomic force microscopy

Atomic force microscopy (AFM) is one of the two prominent scanning probe microscopies developed by Binnig, Rohrer, Gerber, and Weibel at IBM in the 1980s. Compared with its sister technique of scanning tunneling microscopy (STM), which only applies to conductive samples, AFM can measure a broader range of samples that are either conductive or insulative.[23,38-40] The spatial resolution of STM and AFM is directly related to the geometry of scanning tip, and both microscopic methods share the same instrumental scheme: a fixed setpoint of a measurable quantity, raster scanning, and a negative feedback loop to maintain the setpoint. What distinguishes AFM from STM is the measurable quantity: In STM, tunneling electric current is measured; In AFM, mechanical force is measured. In order to measure both stationary and dynamic force, the tip used in AFM is fixed onto a vibrational cantilever, which offsets and oscillates to compensate the force exerted on the tip and is, in turn, used as a detector to extract the force property of samples.

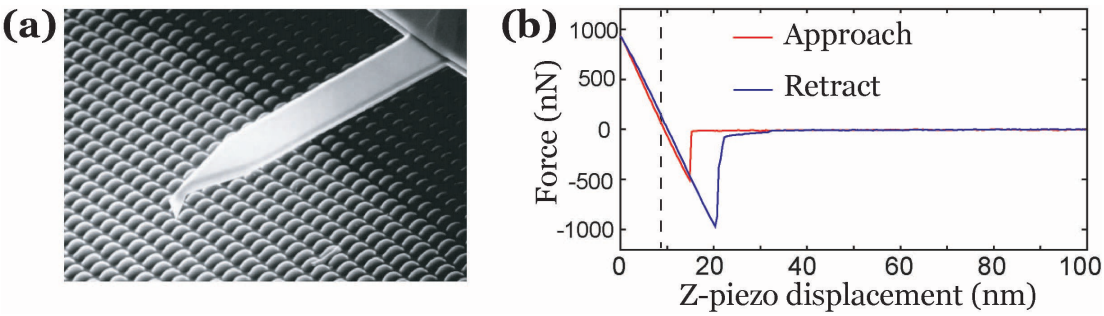

Figure 2. 1 Cantilever and force curve in AFM measurement. An SEM image of the tip fixed on a long cantilever is shown in (a). Copyright: ©American Physical Society 2003.[40] (b) An experimentally collected force curve from Bruker Multimode 8 AFM. In the experiment, an AFM tip (RTESP-150, Bruker Nano) was engaged into and then retracted from the surface of the silicon wafer.

An SEM image of an AFM tip with cantilever and a general force curve (force vs. Z-piezo displacement) are shown in Figure 2.1. The force curve resembles a collective shape of multiple intermolecular forces, both long-range and short-range, including Lennard-Jones potential, Morse potential, and van der Waals force.[40] In addition, the force curve is non-monotonic. It exhibits an attractive regime with negative forces at the long-range and a repulsive regime with positive forces at the short-range. The force curve is also nonsymmetric for approaching and retracting. Useful information can be extracted from the force curve, including Young's modulus, surface adhesion, deformation, and energy dissipation, by using different theoretical models in different cases.[42]

There are two major working modes of AFM: contact mode and tapping mode. In contact mode, the force between the tip and sample is held constant at the setpoint, which usually falls into the repulsive regime, while the tip is scanned over the sample surface. The tip-sample force is actively controlled by a Z-piezo in a negative feedback loop, which lifts the cantilever when the force gets higher than the setpoint and lowers the cantilever down if the force becomes smaller. Consequently, the surface morphology is traced by the offset applied on Z-piezo at each (X, Y) position. In tapping mode, the cantilever is mechanically

driven at its eigenmode and can be described as a driven harmonic oscillator in the free air. When brought close to the sample, the tip-sample force gradient causes the resonance frequency to shift and leads to a reduction of oscillation amplitude, which is characterized by a damped driven harmonic oscillator model.[40] The oscillation amplitude is held as the setpoint in the negative feedback loop. It was demonstrated that tapping mode works best in the attractive regime of the force curve.[43] Figure 2.2 illustrates and compares contact mode vs. tapping mode.

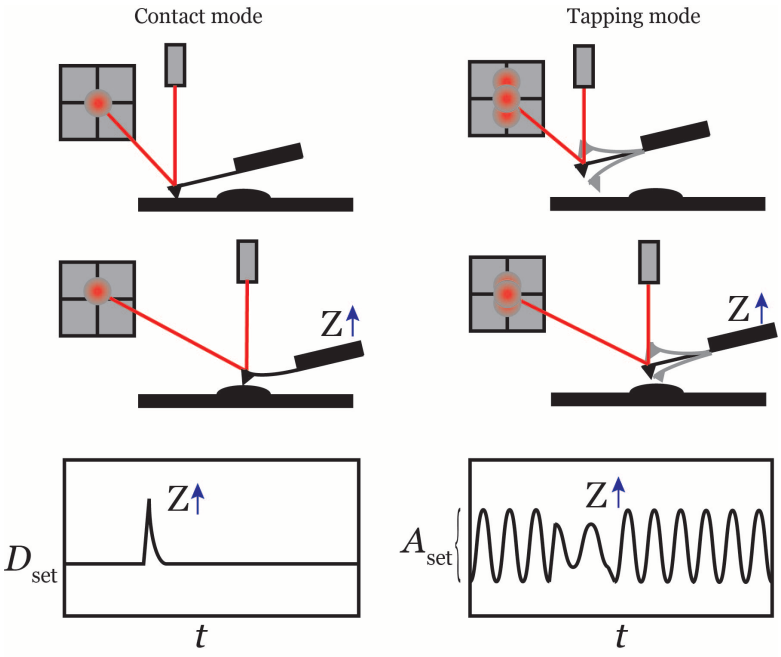

Figure 2. 2 Comparison between contact mode and tapping mode AFM. The force between the tip and sample is measured by monitoring the cantilever bending through detecting the directional change of a diode laser in a quadrant light detector. The tip is scanning from the left, and a DC setpoint D_{set} is used. Once the tip encounters a bump, the cantilever bends upward, and an increase of tip-sample force is detected. The Z-piezo quickly lifts the cantilever to release the force back to D_{set}. In tapping mode, the setpoint A_{set} is set in the tapping amplitude. The Z-piezo moves the tip up and down to maintain a constant A_{set}. The figure is partially reproduced from literature[44].

Several drawbacks are associated with both contact and tapping mode AFM. In contact mode, force measurement depends on the DC deflection of the cantilever, which is susceptible to low-frequency noises (1/f noise) such as thermal vibration.[40] Besides, the contact force is often kept as a large value in the repulsive regime, which means a high possibility that tip can indent, scratch, and damage the sample and itself. Moreover, the spatial resolution of contact mode is often limited by the stick-slip motion of the tip.[45,46] Some issues in contact mode are solved in tapping mode. By dynamically driving the cantilever at a high frequency, tapping amplitude is less subject to the 1/f noise; by operating in the attractive and non-contact regime, the possibility of tip and sample damage is also reduced.[47] However, tapping mode AFM does not provide force information other than topography and phase. The phase information is related to many parameters in complicated ways[48-50] and sometimes elusive. On the other hand, contact AFM can be easily coupled with other modalities, like shear force and electric current measurements, while they are not allowed in tapping mode. Operating tapping mode AFM in the liquid phase is also problematic, as the quality factor of each eigenmode of the cantilever is dramatically damped in the liquid.[51]

Some of the disadvantages above are resolved by using peak force tapping (PFT) mode, also known as pulsed-force mode.[52] PFT works in an intermediate way between contact and tapping modes: it allows the tip to contact the sample intermittently. Unlike tapping mode that usually operates in the attractive and non-contact regime, PFT engages the tip onto and separates it from the sample surface periodically at frequencies (from 0.25 to 10 kHz) well below the cantilever's eigenmodes (hundreds of kHz in the air). As a result, the cantilever is not on resonance, and a force curve can be measured accurately within each tip-sample engaging and separation cycle. The setpoint in PFT is called "peak force," which can be modified in a range from pN to nN, to either ensure a minimized tip-sample contact

or to reveal more mechanical information by exerting a high peak force setpoint. The working mechanism of PFT is sketched in Figure 2.3.

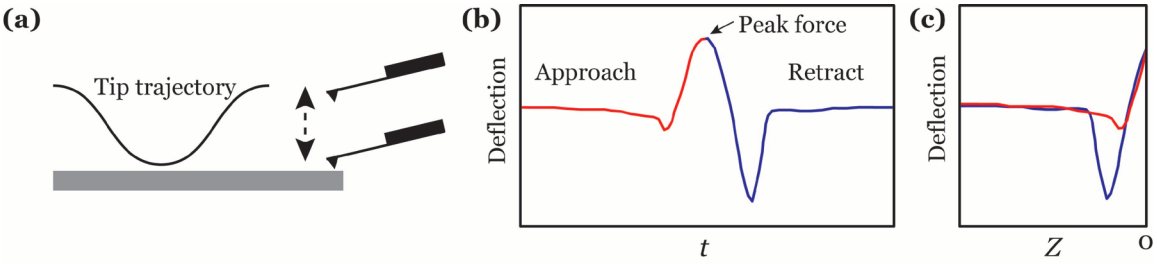

Figure 2. 3 The working mechanism of peak force tapping. In PFT, the tip or sample is driven up and down by a sinusoidal waveform; thus, the tip trajectory relative to the sample surface is shown as a sine wave in (a). The force curve obtained from one PFT cycle is shown in (b), where the cantilever deflection is plotted in the time domain. In (c), the same cantilever deflection is plotted in the tip-sample distance domain, which contains important information about the mechanical properties of the sample and explicit tip-sample distance correspondence to (b). The figure is reproduced from literature[44].

Force curves measured in PFT carry rich information about the sample's mechanical information. Topography, Young's modulus, adhesion, energy dissipation, and sample deformation are mapped out simultaneously in PFT mode.[53] The measurement of electric property can also be implemented with PFT owing to the short but direct tip-sample contact period. Furthermore, the tip-sample distance information contained in force curves can also be used to determine the real-time tip-sample distance, which is vital for studying the tip-sample distance dependence of certain properties. On the other hand, the tip-sample contact happens in a short time of tens of μs. Therefore, the high spatial resolution similar to that of tapping mode is still preserved. As a result, PFT mode has been used in measuring a number of meaningful samples, including quantifying elastic modulus of hardened cement paste and shale,[54,55] imaging chemical and biological sites on living cells,[56,57] identifying chemical composition in block co-polymers,[58] resolving fine structures of membrane proteins and amyloid fibrils,[59,60] and mechanical mapping of

nanobubbles.[61,62] The extensive library of research has exemplified the efficacy of PFT mode in both mechanical measurement and spatial resolution, on rough and delicate samples, in the air and water.

In the rest of this chapter, several abovementioned AFM-IR techniques will be introduced. They are s-SNOM operated with tapping mode, PTIR operated with contact mode, and PiFM operated with tapping mode. In the following chapters, we developed two novel techniques – peak force scattering-type near-field optical microscopy (PF-SNOM) and peak force infrared (PFIR) microscopy. The adoption of PFT mode in these novel methods enhances the detection performance and enables serendipities in analyzing nanoscale light-matter interactions.

2.2 Scattering-type scanning near-field optical microscopy

The development of SPM techniques during the 1980s also enabled advances in scanning near-field optical microscopy, which is known as SNOM or NSOM. The early implementation of SNOM is to bring an aperture probe into close vicinity to the sample, and the same aperture on an optical fiber excites and detects optical near-field effects. The spatial resolution of the aperture SNOM is determined by the radius of aperture, which is usually made at the end of metal-coated optical fibers.[63] However, the size of the aperture cannot be made very small, since a smaller aperture means a decrease in the transmission efficiency of the fiber. Therefore, the spatial resolution of the aperture SNOM is still limited to about $\lambda/10$ in practice.[64] Later, it was demonstrated that an "apertureless" scheme also works in SNOM: the tip-enhanced light field (scattering light) around a sharp metallic apex is not bound to the optical diffraction limit.[65] The apertureless SNOM is popularly denoted as scattering-type scanning near-field optical microscopy (s-SNOM) and has made the aperture SNOM eclipsed since its invention. Applications of s-SNOM

are broad, ranging from plasmonic devices, polymers, minerals, plasmonic and polar 2D materials, and biological samples.[66-78]

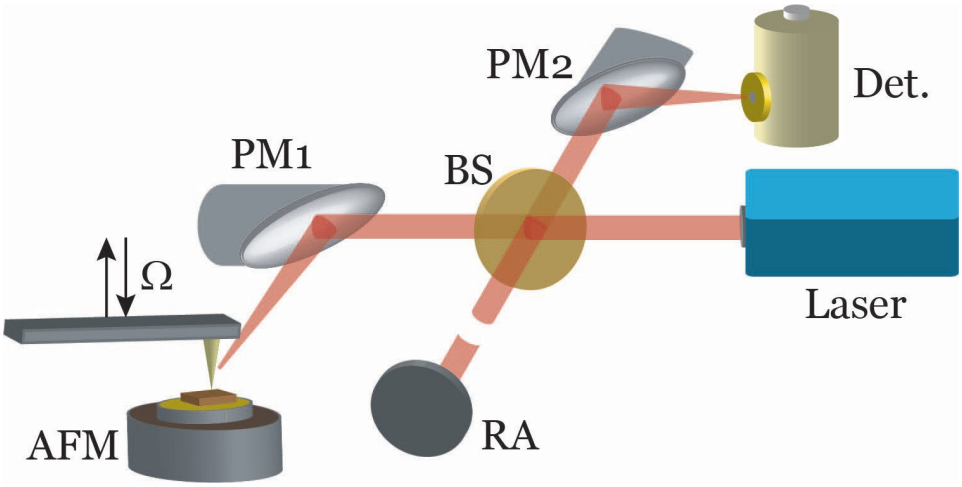

Figure 2. 4 A general s-SNOM setup.PM: parabolic mirror; Det: Detector; BS: beam splitter; RA: reference arm; Ω: tapping frequency.

A general s-SNOM setup is shown in Figure 2.4. It is composed of a laser source that outputs continuous waves (usually in infrared), a beam splitter, a focusing element (in Figure 2.4 it is a parabolic mirror) that directs and focuses the light into the tip-sample region, an AFM operated in tapping mode with the cantilever oscillating at a frequency of Ω, a far-field light detector, and a reference arm that allows interferometric detection of the back-scattered light from the tip-sample region. In s-SNOM, the far-field radiation from the laser source is firstly converted into near-field radiation within the tip-sample domain. The intense light field can trigger tip-sample near-field interactions to happen, and the resulting scattering collected by the same focusing element (parabolic mirror 1) travels back towards the beam splitter and interferes with the original far-field radiation. The interference light field is then guided into and detected by the far-field light detector.

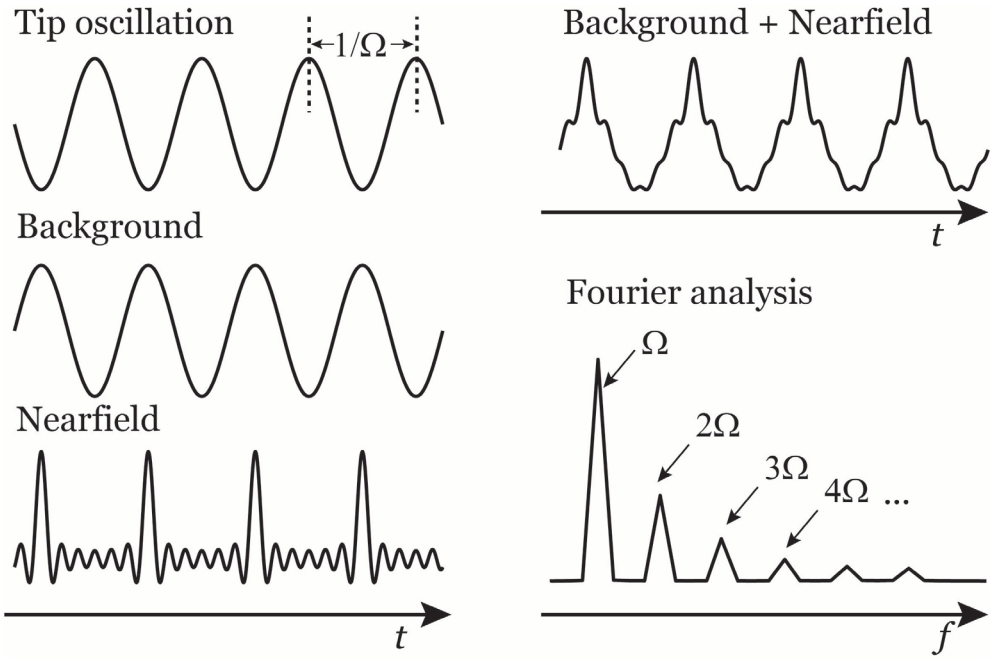

Figure 2. 5 Signal generation in s-SNOM. The tip is oscillating harmonically at a frequency Ω. The background scattering is modulated harmonically, while the near-field scattering (simulated) increases at lower turning points and diminishes at a long tip-sample distance. The amplitude of near-field scattering is extracted by performing a Fourier analysis on the total signal and picking the amplitude from a high harmonic ($\geq 2\Omega$) component.

Note that the back-scattered light contains more information than the needed near-field scattering. For example, the scattered light from the tip shaft and sample surface is also registered in the scattered light and contributes to the signal background. The background is suppressed by performing Fourier analysis on the detected light signal. Because the cantilever is oscillating harmonically at a frequency Ω, the background scattering should be modified by the harmonic frequency of Ω as well. On the other hand, the near-field interaction only happens when the tip is brought near to the sample, that is, around the lower turning point of the tip oscillation. This near-field nature of tip-sample interactions will add anharmonicities into the harmonically modulated background. Consequently, the magnitude of near-field interactions can be assessed by analyzing non-harmonic terms in

the Fourier analysis of detected total signals. This process is shown in Figure 2.5. In practice, the Fourier analysis is performed by a lock-in amplifier that demodulates the signal from the detector at the fundamental frequency of Ω in real-time. Higher demodulated harmonics are more background-free and contain purer near-field signal. However, the amplitude of higher harmonics is also significantly lower. As a result, harmonics of 2-4 are usually adopted as s-SNOM signals.

Besides the amplitude, the optical phase of near-field scattering is also obtainable from interferometric detections, which completes the full profile of the optical nearfield around the tip-sample region. Commonly used interferometric methods include a homodyne scheme[79] and a pseudo-heterodyne scheme.[80] Both methods are for single-frequency light detection since the s-SNOM signal comes from the elastic light scattering. In addition to the detection purpose, the reference arm also allows advanced applications, such as the synthetic optical holography[81] and nano-FTIR with a broadband laser source.[82]

Unlike other AFM-IR techniques that mechanically detect the photothermal expansion, s-SNOM uses far-field light detection, and its signal can be derived from plasmonic optics. A general model used in s-SNOM is called the image dipole model, in which the end of the AFM tip is treated as a dipole, and tip-sample interactions in the nearfield are treated as interactions between the tip dipole and the induced dipole in the sample.[83] Another model is termed as the finite dipole model, in which the tip is modeled as an isolated spheroid.[84] In terms of accuracy, the finite dipole mode is better, since it is more accurate in the approximation of the tip geometry.[84-86] For the sake of simplicity, the image dipole model is introduced here to understand the signal source in s-SNOM. As an elastic scattering process, the field amplitude E_s detected in s-SNOM can be estimated as the product of the effective polarizability α_{eff} and the amplitude of incident light E_{inc}, which is shown in the following equation:

$$E_s \approx \alpha_{\text{eff}} E_{\text{inc}} \quad \textbf{(2.1)}$$

Equation 2.1 holds in both image and finite dipole models. In the image dipole model, the effective polarizability α_{eff} is a function of the polarizability of the tip (α) and the sample (β), the tip radius r, and the tip-sample distance d. The expression of α_{eff} is written as:

$$\alpha_{\text{eff}} = \frac{\alpha}{(1 - \frac{\alpha\beta}{16\pi(r+d)^3})} \quad \textbf{(2.2)}$$

The tip's polarizability α is given by $\alpha = 4\pi r^3(\varepsilon_{\text{t}} - 1)/(\varepsilon_{\text{t}} + 2)$, with ε_{t} being the permittivity of the tip, in a form that is equivalent to the dipolar plasmonic enhancement in Equation 1.5. The induced polarizability β of sample is given by $\beta = (\varepsilon_{\text{s}} - 1)/(\varepsilon_{\text{s}} + 1)$, with ε_{s} being the permittivity of the sample. Equation 2.2 indicates that if the same tip and tapping condition are used (with constant α, r, and d), the s-SNOM signal becomes a function of β, which relates to the sample's permittivity. Equation 2.2 is derived based on the steady-state approximation at a stable tip-sample distance. In reality, s-SNOM signals come from the Fourier analysis of the modulated light scattering, which is generated dynamically in numerous tapping cycles. Therefore, the phase measured in s-SNOM cannot be directly used to represent the sample's IR absorption, which is correlated with the imaginary part of the permittivity.[87] The same reason explains why s-SNOM is widely applied in nanophotonics, where the near-field intensity is most interested, but much less used in the chemical identification for unknown samples. When applying s-SNOM on spectra measurements, one often gets dispersive profiles around IR absorption peaks.[66,88]

2.3 Photothermal induced resonance

Photothermal induced resonance (PTIR) microscopy is the most representative AFM-IR method due to its early commercialization.[26,89] The PTIR signal was proved to be proportional to the IR absorption of the sample, through both experimental and analytical

demonstrations.[90] Figure 1.7 in Chapter 1 also hinted at this relation. PTIR provides comparable IR absorption measurements to results from traditional FTIR methods with a much-improved nanoscale spatial resolution.[31,35,91]

In PTIR operation, once the energy is absorbed, the sample volume expands due to the photothermal effect. For nanoscale objects, such expansion has a short relaxation time on the order of ns.[35] The short expansion generates a transient force impulse to the cantilever, which is always in contact with the sample surface in contact mode AFM. The stimulated cantilever exhibits induced vibrations and the magnitude of vibrations is proportional to the IR absorption of the sample.[87] The detection of the cantilever's vibration is thus equivalent to detecting the photothermal expansion. In this way, no far-field light detector is needed, as the vibration of cantilever is simultaneously recorded by a built-in quadrant photodiode in most AFMs. On the other hand, since the photothermal expansion is quick and short, a pulsed laser source is used in PTIR to generate many cantilever vibration events and enable the signal averaging.

Except for the omission of the far-field light detector, the beam splitter, and the reference arm, the experimental setup of PTIR is similar to that of s-SNOM in Figure 2.4, using a pulsed laser source. Two geometries are used for the delivery of pulsed light field into the tip-sample region. One way is to use side illumination, where the light is directed into the tip-sample region from one upper side of the cantilever (s-SNOM uses this way); The other way is to use bottom illumination with a prism as the sample stage. For the latter case, the direction of the light beam is adjusted to fulfill the total internal reflection condition, which generates a strong evanescent field along the Z-axis at the surface of the prism. When the sample thickness is smaller than the light wavelength, a strong tip-enhanced field also occurs in the total internal reflection configuration.[51] The benefits of using the prism are in three aspects: First, laser alignment is simplified compared with the side

illumination. In the side illumination, the focus spot needs to scan in all X, Y and Z directions to locate the tip; In the total internal reflection configuration, the spot only needs to scan in two directions of X and Y, once the position of the prism is fixed. In addition, the evanescent field also enhances the field intensity,[92] thus allowing a larger alignment tolerance by using a relatively loose focus spot. Second, unwanted light-cantilever interactions are avoided by the total internal reflection, as the light intensity is mostly confined in the tip-sample region.[87] At last, because the light is delivered through the prism, the strong IR attenuation of water is minimized. The use of prism can enable the instrumentation of PTIR in the aqueous phase.[51,93,94] A schematic of the total internal reflection and the signal generation of PTIR is illustrated in Figure 2.6.

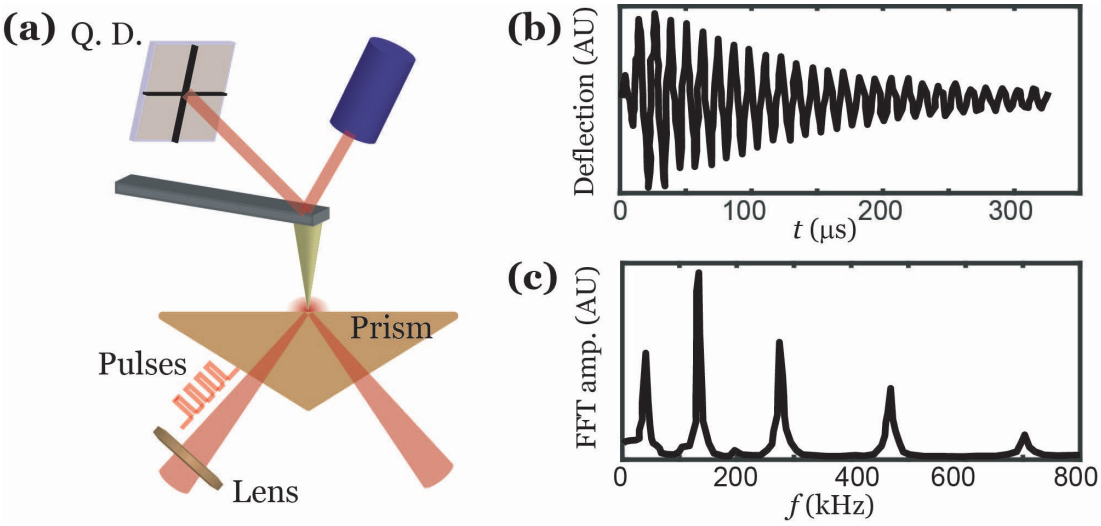

Figure 2. 6 Signal generation in PTIR. A scheme of total internal reflection is shown in (a), where laser pulses incident from the bottom of a prism to form the total internal reflection. The PTIR signal is from the transduction of incident energy → heat → photothermal expansion → cantilever oscillation → quadrant detector (Q. D.) signal. An example of the cantilever oscillation detected by Q. D. and its Fourier transform is shown in (b) and (c). The PFIR signal can either obtained by the maximum oscillation observed in (b) or one of the contact resonance's amplitudes in (c). Panels (b) and (c) are reproduced from literature[95].

A better signal to noise ratio can be achieved in PTIR by modulating the laser pulses at a repetition rate of one of the contact resonances of the cantilever. This technique is resonantly enhanced and sometimes referred to as resonantly enhanced infrared nanoscopy (REINS).[32,51]

Compared with s-SNOM, applications of PTIR skew more towards chemical and biological samples as IR absorptions in these cases are most interested. PTIR has been used in imaging metal-organic frameworks (MOFs), perovskites, polymers, proteins, bacteria, and cells. These works have been grouped and introduced in several seminar reviews.[87,89,90,96]

2.4 Photoinduced force microscopy

Photoinduced force microscopy (PiFM) provides another route to achieve nano-IR imaging and spectroscopy based on tapping mode AFM.[27] Conventional PiFM setup uses the side illumination, but the total internal reflection geometry is also feasible. The signal generation in PiFM is not as straightforward as that in PTIR, which directly detects the push force on the cantilever after short light pulses. In PiFM, the first two fundamental resonant modes (Ω_1 and Ω_2, $\Omega_1 < \Omega_2$) of the cantilever are exploited for unique purposes: the Ω_2 mode is used for tapping mode control to map the topography and the mode at Ω_1 is used for detecting light-induced effects.

Tapping with the second mode Ω_2 gives out a sinusoidal motion of the tip at the same frequency. In PiFM operation, an external laser is modulated at a rate of $\Delta = \Omega_2 - \Omega_1$. Similar to the amplitude modulation in radio waves, modulating the photoinduced force gradient at the frequency of Δ is equivalent to an amplitude modulation term on the waveform with the carrier frequency of Ω_2. Therefore, a sideband signal with a frequency at $\Omega_1 = \Omega_2 - \Delta$ is generated and enhanced by the first fundamental oscillation mode at Ω_1. This sideband coupling process is depicted in Figure 2.7. The sideband coupling detection

is found to be more sensitive to the photoinduced force and displays a steeper dependence on the tip-sample distance, enabling a better signal-to-noise ratio in PiFM than the direct coupling detection with the modulation frequency of Ω_1.[27,97,98] In practice, the tapping amplitude in PiFM is set to a small value (< 10 nm) to minimize the tip-sample distance and maximize the photoinduced force's contribution to the modulated cantilever motion.

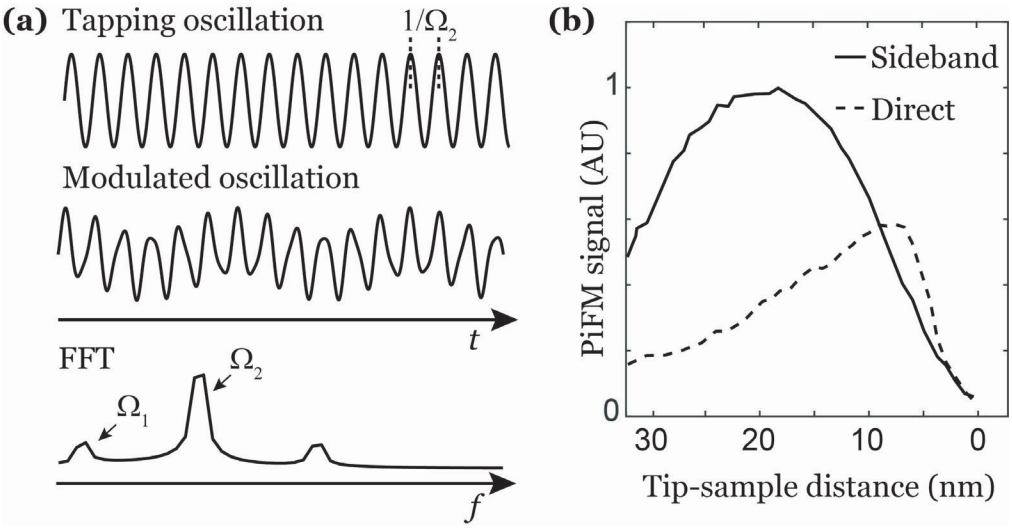

Figure 2. 7 Signal generation in PiFM. In (a), the AFM tip is tapping at the frequency Ω_2, and an amplitude modulation term with the frequency of $\Delta = \Omega_2 - \Omega_1$ is added to modulate the tapping waveform. As a result, signals at the sideband (Ω_1) is generated after FFT. In (b), two modulation methods are experimentally compared in PiFM. The "Direct" method means modulating the laser pulses at Ω_1 and detecting at the same frequency. Sideband configuration provides systematically stronger signals within a wide tip-sample distance range than the direct configuration. The non-monotonic trend in both cases results from the competence between the photoinduced force and general intermolecular forces. Panel (b) is reproduced from literature[27].

In the early works of PiFM, the photoinduced force in PiFM was believed and modeled to come from dipole-dipole interactions between the tip and sample.[27,97,98] However, later theoretical and experimental works indicate that the dipole-dipole force is too weak to detect in PiFM, and the majority of the photoinduced force is from the photothermal

expansion.[99-101] Asides from ongoing debates on the origin of photoinduced force, PiFM provides complimentary nano-IR imaging capabilities to PTIR and s-SNOM. A variety of studies have been conducted using PiFM, including block copolymers, zeolites, photovoltaic samples, and plasmonic and polaritonic devices.[102-107]

2.5 Limitations of current techniques

So far, the working mechanisms of s-SNOM, PTIR, and PiFM have been described in this chapter. All techniques take advantage of the tip-enhanced light field as the scanning probe and bring the resolution of IR imaging and spectroscopy down to the nanoscale. Nonetheless, each method has its drawbacks, which come from limitations of the signal detection scheme and intrinsic restrictions from AFM operation modes.

The spatial resolution of PTIR is mainly limited by contact mode AFM. As mentioned in section 2.1, the tip may easily scratch the sample and wear itself in contact mode operations. The presence of friction force also causes the tip to move in a "stick-slip" motion, which significantly worsens the spatial resolution. As a result, PTIR can only achieve a spatial resolution of 25 – 100 nm in routine experiments. The other limitation associated with PTIR is the relatively low signal to noise ratio, as one often observes stripes and artifacts in PTIR images. A way to increase the signal to noise ratio is to use multiple laser pulses to enhance the signal at one of the contact resonances. The effectiveness of resonant enhancement depends on quality factors (Q factors) of contact resonance modes of the cantilever. However, in the liquid phase, quality factors get damped significantly due to the strong drag by liquid molecules.

The spatial resolution limitation is improved in PiFM by operating with tapping mode AFM. As a result, a spatial resolution of 10-20 nm is routinely achieved. In PiFM, the tapping amplitude is often set to a small value to maximize the contribution of photoinduced force. Problems caused by this preference are twofold: a low tapping

amplitude often leads to a close tip-sample configuration, which can damage the tip and sample; The uneven sample surface often causes tapping conditions to change, and a stable tip-sample distance (on average) is hard to maintain. This instability is especially problematic for PiFM, as the signal dependence on the tip-sample distance is steep at close range (Figure 2.7). Besides, from the viewpoint of instrument design, it is hard to combine tapping mode with other modalities. Some desirable quantities like electric and mechanical properties cannot be measured simultaneously with PiFM, while these quantities can be easily measured with PTIR. At last, PiFM requires cantilevers to have two well-defined eigenmodes, which limits PiFM's application in water since the quality factor is significantly reduced in the liquid phase.

s-SNOM also operates with tapping mode AFM and can routinely achieve 10-20 nm spatial resolution. On the one hand, s-SNOM share the same limitations of tapping mode as PiFM: s-SNOM cannot measure other properties, and it is even harder for s-SNOM to operate in water, because the s-SNOM signal comes from the light detection, but the mid-infrared light is strongly absorbed by water. On the other hand, s-SNOM has its limitations. As a permittivity-sensitive method (Equation 2.2), s-SNOM is often used to characterize optical nearfields around nanoplasmonic and nanopolaritonic structures. Nevertheless, because the tip-sample distance is constantly changing in tapping mode and the lock-in detection is used, s-SNOM can only map out amplitudes and phases as single demodulated values in a 2D image on the XY plane. The dependence of the optical nearfield on the tip-sample distance is averaged out and lost after the averaging. Such information is indispensable for reconstructing 3D optical nearfields and better understanding the device's behavior in space.

With these limitations in mind, it is natural to think about better ways of performing nano-imaging and spectroscopy. It turns out that some of the limitations can be addressed by a

better AFM operation mode, and some of the limitations can be lifted by using a better excitation and detection scheme. In Chapters 3 and 4, two novel methods that we developed – one aims to complete the s-SNOM and the other aims to replace PTIR and PiFM in water – will be introduced and explained along with a plethora of demonstrations.

Chapter 3 Three-Dimensional Anatomy of Optical Nearfield in Mid-Infrared

In this chapter, our works on developing ways of obtaining three-dimensional (3D) optical nearfield are presented. The chapter starts with an introduction about the need for characterizing 3D nearfields, then a reconstruction algorithm in s-SNOM is described and demonstrated. This reconstruction method allows obtaining 3D near-field information by making use of a series of Fourier components from a 2D s-SNOM scan. Finally, and most importantly, the development of peak force scattering-type near-field optical microscopy (PF-SNOM) is reported. PF-SNOM can directly collect 3D near-field data into a data cube, enabling layer-by-layer tomographic imaging and vertical analysis. Near-field properties along the Z-axis for polaritonic boron nitride nanotube and silicon carbide were investigated, and the resonant conditions of a circular nano-disk of hexagonal boron nitride were experimentally observed using PF-SNOM. In addition, we also demonstrated multi-modal capabilities from peak force tapping. Near-field properties obtained in PF-SNOM contain one more spatial dimension than those measured in the regular s-SNOM and help inspire unprecedented insights into near-field light-matter interactions.

3.1 The necessity of mapping 3D optical nearfield

The ability to map nearfields in detail in nanophotonic applications becomes crucial as the feature size becomes ever finer, especially when general theoretical modeling is still far from practical and nearfield is highly dependent on nanoscale geometry. The knowledge of nanoscale nearfield is vital for reconstructing vector maps of both electric and magnetic fields and designing nanophotonic and sensing applications.[108]

s-SNOM has been employed in many subwavelength nanophotonic studies since its superior functionalities and spatial resolution. However, s-SNOM imaging does not

provide information on the nearfield along the vertical direction, which strongly depends on the tip-sample distance. This limitation is intrinsic for conventional s-SNOM due to the lock-in demodulation scheme and tapping mode operation, as discussed in Section 2.5. In other words, near-field images obtained by conventional s-SNOM are merely 2D representations of actual 3D nearfields. The approach curve method is used to infer the vertical near-field signals to get around this limitation in s-SNOM.[83,109-111] In this method, a demodulated non-fundamental harmonic is recorded as the oscillating cantilever is approaching the sample surface. By performing the approach curve pixel-by-pixel, volumetric data can be obtained and processed to assess 3D nearfields. This method is time-consuming and may lead to wrong interpretations of actual near-field properties.[112]

Therefore, mapping 3D optical nearfields remains a challenge for s-SNOM. In the following sections, we will describe how to address this issue in two ways. The first way is to use a reconstruction algorithm that takes advantage of a series of demodulated harmonics from the conventional s-SNOM measurement.

3.2 Reconstruction method in s-SNOM

3.2.1 Reconstruction algorithm

One of the non-fundamental harmonics from the lock-in demodulation is used as the s-SNOM signal, based on the assumption that the background is mainly contained in the fundamental harmonic. Therefore, it is plausible to assume a contribution coefficient η, which describes the contribution from near-field signals in the first harmonic. Furthermore, the total near-field signal $S_{\mathrm{NF}}(x, y, z)$ in 3D space should be composed of the near-field signals in the first harmonic, plus all other non-fundamental harmonics that are assumed to be purely near-field:[112]

$$S_{\mathrm{NF}}(x,y,z) = \eta(x,y)A_1(x,y)\sin[\sin^{-1}\left(1-\frac{z}{z_o}\right)+\Phi_1(x,y)] + \sum_{n=2}^{N} A_n(x,y)\sin[n\sin^{-1}(1-\frac{z}{z_o})+\Phi_n(x,y)] \quad \textbf{(3.1)}$$

Here, we consider a scanning process that scans (x, y) positions on the sample surface, so $\eta(x, y)$ represents the site-specific contribution coefficient of near-field signals to the first harmonic, A_n and Φ_n are the amplitude and phase demodulated from the lock-in amplifier for n^{th} harmonic, and z_0 is half of the tapping amplitude. The real-time tip-sample distance z is thus provided by $z = z_0[1 - \sin(2\pi\Omega t)]$, and the inverse sin term in brackets solves for the time variable t. The total number of harmonics N goes to the infinity in principle, while in our experiment, $N = 11$, which is limited by the number of demodulation channels or the bandwidth of the lock-in amplifier. Equation 3.1 contains 3D spatial information of nearfields, and S_{NF} can be mapped out in the 3D space once $\eta(x, y)$ is known.

Experimentally, demodulated A_n and Φ_n values can be extracted directly from the lock-in amplifier, and the tapping amplitude z_0 is set as a constant by AFM. The next step is then solving for $\eta(x, y)$. To simplify the notation, consider the point measurement only, where the near-field signal only depends on η and z. We can then construct an integral metric M:[112,113]

$$M = \int_{4r}^{2z_0} \left(\frac{dS_{\mathrm{NF}}(\eta,z)}{dz}\right)^2 dz \quad \textbf{(3.2)}$$

Equation 3.2 presents a metric M as the integral of the square of near-field interaction slopes along the z direction. This definite integral is integrated within a distance range from $4r$ to $2z_0$, with r being the tip radius. The idea of constructing the metric M is to estimate the change of near-field signals as the function of tip-sample distance z in terms

of $dS_{\mathrm{NF}}(\eta, z)/dz$. Due to the near-field nature of the tip-enhancement, near-field signals should diminish at a long tip-sample distance range, nominally at a tip-sample distance that is greater than $4r$. Therefore, within the distance from $4r$ to $2z_0$ (which is the upper turning point in the tapping), a negligible value of M should be expected. By minimizing the value of M for each scanned pixel, one can obtain the contribution coefficient $\eta(x, y)$ that best represents the portion of near-field signals in the first harmonic demodulation. Lastly, the 3D near-field signal $S_{\mathrm{NF}}(x, y, z)$ can be reconstructed using Equation 3.1. The workflow of this reconstruction process is depicted in Figure 3.1.

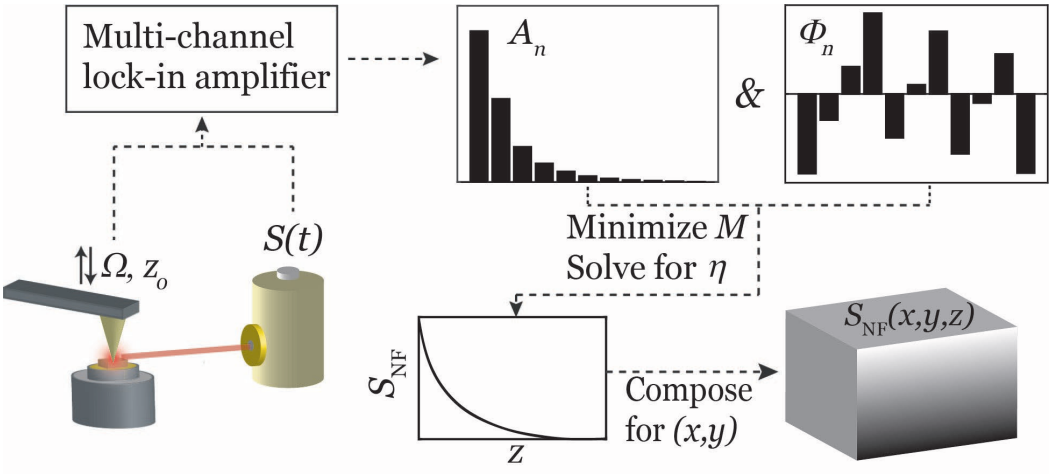

Figure 3. 1 The workflow of the reconstruction method in s-SNOM.The scattered light $S(t)$ from the tip-sample region is detected by an optical detector. Then, the $S(t)$ is routed into a multi-channel lock-in amplifier, which demodulates the signal at the fundamental frequency Ω of the tip tapping. Demodulated A_n and Φ_n are later used to compose a tentative S_{NF} with a guessing value of η, and the value of η is optimized in the process of minimizing the metric M. Lastly, $S_{\mathrm{NF}}(z)$ is reconstructed by the optimized η, and the same procedure is applied to all scanned pixels to obtain a 3D data cube $S_{\mathrm{NF}}(x, y, z)$.

The reconstruction method was firstly demonstrated by Le and Xiaoji in point measurements.[113] In point measurements, the tip is fixed on a position of interest, and a total of 18 harmonics ($N = 18$) is collected to perform the reconstruction. Because the used lock-in amplifier (HFLi, Zurich Instrument) only has six demodulation channels, these 18

harmonics are obtained in three sequential measurements, with six harmonics obtained from each. The data is then saved and processed for the η numerically using a custom MATLAB script. Representative values of η are between 0.2-0.3, indicating the presence of near-field signals in the first harmonic is not negligible, although the first harmonic is discarded in standard s-SNOM. Later, we speeded up the process of signal acquisition by obtaining 11 harmonics simultaneously from two parallel lock-in amplifiers, which makes it possible to perform the reconstruction for an entire scanned image.[112] In the image scan mode, 11 harmonics and the real-time position of scanning piezo in (x, y) are stored. The data is then processed for each (x, y) position to attain an $S_{\mathrm{NF}}(x, y, z)$ cube.

3.2.2 Measuring phonon polaritons by reconstruction s-SNOM

The $S_{\mathrm{NF}}(x, y, z)$ data cube contains plentiful information. First of all, sectioning the cube along the Z-axis is equivalent to perform tomographic imaging. Figure 3.2 shows the tomographic imaging of a polaritonic boron nitride nanotube (BNNT),[114] which is about 1.2-μm long, 80-nm wide, and 25-nm in height. Overall, reconstructed near-field images show similar contrast to the standard s-SNOM image, and the signal intensity decays as the tip-sample distance increases. The spatial signal variations along the BNNT are signatures of the mid-infrared surface phonon polaritons. On the other hand, one effect in large-distance tomographic images is noticeable: strong near-field signals persist along two long edges of the BNNT. The positions are indicated by two white arrows in Figure 3.2(a). These two intense near-field signal regions roughly span 40 nm from the edge of BNNT.

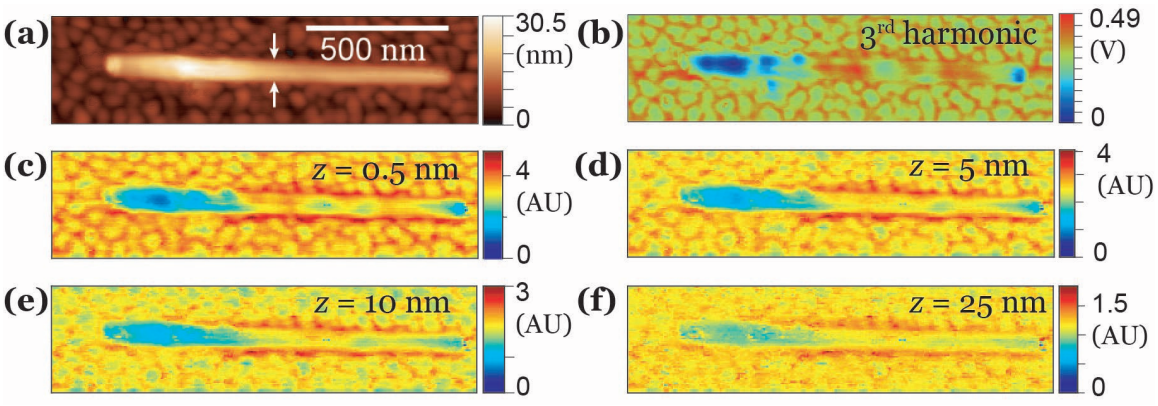

Figure 3. 2 Tomographic imaging of BNNT by reconstruction s-SNOM.(a) AFM topography of a BNNT sitting on a rough gold substrate. (b) Standard s-SNOM image from the 3rd harmonic demodulation under 1400 cm^{-1} light illumination. (c-f) Reconstructed near-field images at the tip-sample distance z = 0.5, 5,10, and 25 nm, respectively.

Additional field enhancement along the long edges of BNNT is better understood by sectioning the 3D data cube across the tube, and the result is shown in Figure 3.3(b). Peak near-field intensities are reproduced at two BNNT edges, which is attributed to the presence of phonon polaritons that are at side faces of the BNNT). Vertical near-field signals $S_{NF}(z)$ of these bounded phonon polaritons are investigated. Averaged $S_{NF}(z)$ curve along the one edge of the BNNT is shown in Figure 3.3(c). To rule out any effects caused by the substrate, an averaged $S_{NF}(z)$ is also obtained and subtracted from the previous $S_{NF}(z)$ curve. Finally, we can obtain a background-free $S_{NF}(z)$ curve for bounded phonon polaritons in Figure 3.3(d). The $S_{NF}(z)$ curve does not show the characteristic exponential decay. Instead, it shows a linear decay for $z < 50$ nm and exhibits ups and downs at a larger z range. This anomalous decay behavior is due to the tip-sample geometry displayed in Figure 3.3(d) inset: the bound electromagnetic fields generated by bounded phonon polaritons are tangentially detected by the tip and add to local $S_{NF}(z)$. The ability to resolve the presence of the bound electric field in elevated imaging planes is a unique feature of the reconstruction s-SNOM.

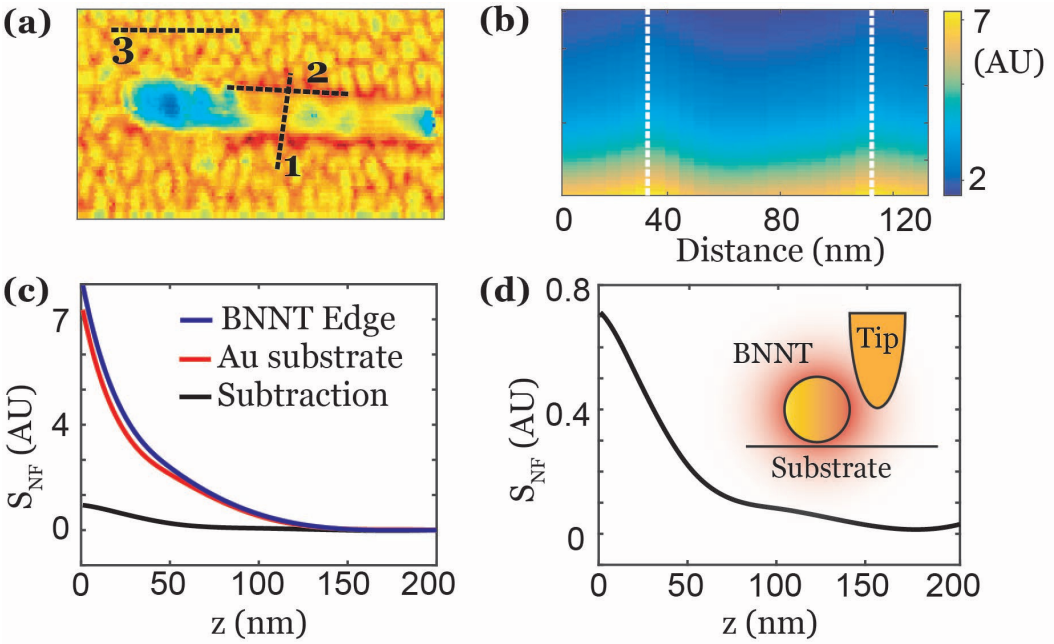

Figure 3. 3 Revealing bound phonon polaritons on the edge of BNNT.(a) The same reconstructed near-field image of BNNT, as in Figure 2(c). The image is enlarged asymmetrically for better illustration. (b) Near-field section in the XZ plane along the Y-axis, the position is shown as the line cut 1 in (a). Edge locations of BNNT are illustrated by two white dashed lines. (c) Vertical interaction curves $S_{\mathrm{NF}}(z)$ averaged from two line cuts, which are indicated by the line cuts 2 and 3 for the BNNT edge (blue) and the Au substrate (red), respectively. The subtraction between the two $S_{\mathrm{NF}}(z)$ is shown as the black curve to represent the near-field behavior of bounded phonon polaritons of BNNT. The subtraction curve is enlarged in (d). Inset in (d) shows the tip-BNNT geometry of detecting bound phonon polaritons.

Compared with the approach curve method, the reconstruction s-SNOM is faster and free of ambiguities caused by the averaging effect in the lock-in demodulation.[112] Even so, the reconstruction s-SNOM is still far from ideal. For example, to get a larger signal for higher harmonic demodulation, the tapping amplitude z_0 must be set to a small value to maximize near-field interactions. This treatment can inevitably introduce artificial anharmonicities into the scattered signal. Another limitation is from the viewpoint of cost: a multi-channel lock-in amplifier or a series of lock-in amplifiers are needed in the

reconstruction s-SNOM since many (> 10) harmonics are required in the tedious optimization process of η. In sum, there is still room for a better 3D near-field mapping technique.

3.3 Peak force scattering-type near-field optical microscopy

3.3.1 PF-SNOM working principle

Now that the tip-sample distance dependence is lost during the lock-in demodulation in s-SNOM, it is intuitive to think of a way to replace the lock-in detection scheme with a tip-sample distance-sensitive signal acquisition route. The lock-in detection is specifically adopted to separate the harmonically modulated background from non-harmonically modulated near-field signals in tapping mode AFM. Therefore, a non-tapping AFM operation should be used to get around the lock-in detection. Contact mode AFM does not work for this purpose, because the tip is always in contact with the sample during the operation, mixing small near-field signals with compound backgrounds in the optical scattering. The ideal AFM mode should still be able to modulate the tip-sample distance in a non-tapping way and is compatible with practical background-removal methods.

The demands are met by the peak force tapping (PFT) mode. Details of PFT operation has been discussed in Section 2.1. In brief, the cantilever is held stationary in PFT, when the sample stage oscillates vertically at a low frequency in a sinusoidal manner. As a result, the tip-sample distance $z(t)$ is definite at any given time point with the known snap-in time point t_s, the detachment time point t_d and the peak force time point t_p:[53,86]

$$z(t) = \begin{cases} A - A\cos\left[2\pi f\left(t - t_p\right)\right] + VD(t), & t < t_\mathrm{s}\ and\ t > t_\mathrm{d} \\ 0, & t_\mathrm{s} \le t \le t_\mathrm{d} \end{cases} \qquad \textbf{(3.3)}$$

In Equation 3.3, A is the PFT amplitude in nm, f is the PFT frequency in Hz, V stands for the deflection sensitivity (in the unit of nm/V) of the cantilever, and $D(t)$ is experimentally monitored deflection signal of the cantilever in V. All parameters in Equation 3.3 can be

obtained experimentally. In an ordinary PFT tapping, $A = 150$ nm, $f = 2$ kHz, and $V = 30$ nm/V. With a definite $z(t)$ established, it is convenient to convert the detected scattering signal $S(t)$ in the time domain into the tip-sample distance domain $S(z)$ as well.

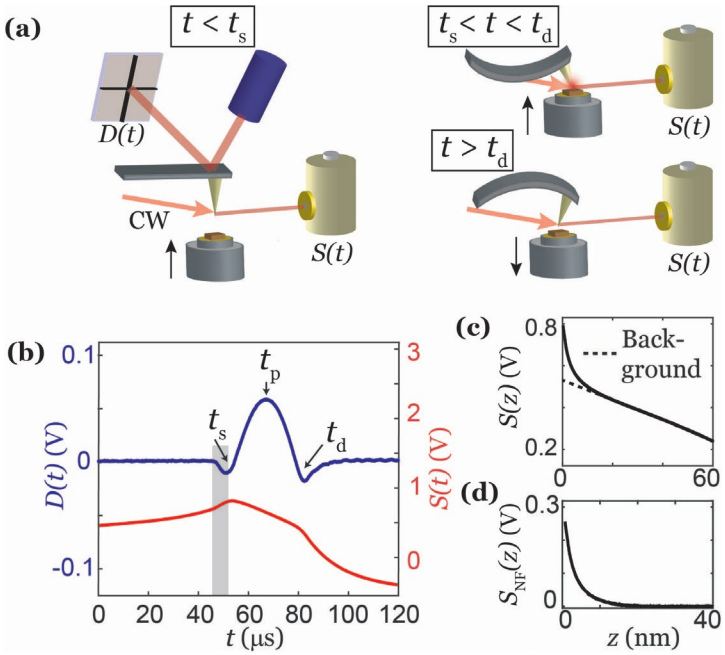

Figure 3. 4 Signal generation in PF-SNOM.(a) In PF-SNOM, the cantilever deflection signal $D(t)$ and the scattering signal $S(t)$ are simultaneously registered by the quadrant detector and the light detector. At time $t < t_s$, the sample is moving towards the tip, and a flat $D(t)$ and a small but increasing $S(t)$ are detected. At time $t_s \leq t \leq t_d$, the tip is in contact with the sample, and the upward bending of cantilever causes an increase in $D(t)$. At time $t > t_d$, the adhesion drags the cantilever to bend downward, which causes a decrease in $D(t)$. Arrows along the sample stage indicate the direction of the stage motion. CW: continuous wave. (b) Simultaneously registered $D(t)$ (blue) and $S(t)$ (red) on a gold substrate under 1600 cm^{-1} illumination. The snap-in, peak force, and detachment time points t_s, t_p and t_d are labeled. A sudden increase right before the t_s in $S(t)$ can be observed in the shaded region. (c) The plot of $S(z)$ in the tip-sample distance domain. The sharp increase of the near-field signal remains, and a linear far-field background can be fitted out. The background-free $S(z)$ is utilized as the pure near-field signal $S_{NF}(z)$ shown in (d), which accounts for the tip-sample dependence.

Remarkably, the $S(z)$ curve carries near-field signals. One example of experimentally collected $S(z)$ is shown in Figure 3.4(b), in which a sharp increase of scattering signal raised by the short-range near-field interaction is observed. Within regions of a long tip-sample distance, $S(z)$ shows a linear decrease as z increases – an expected behavior of far-field background. Therefore, the near-field signal $S_{\mathrm{NF}}(z)$ can be isolated from $S(z)$ by subtracting the linear far-field background. $S_{\mathrm{NF}}(z)$ at different (x, y) locations can be obtained in the same way and a 3D data cube of $S_{\mathrm{NF}}(x, y, z)$ is composed for in-depth near-field analysis. The working mechanism and signal generation of PF-SNOM are summarized and illustrated in Figure 3.4. A technical drawing of the PF-SNOM setup and MATLAB scripts used to process raw data are provided in Appendix I.

3.3.2 Studying 3D nearfields of boron nitride nanotube by PF-SNOM

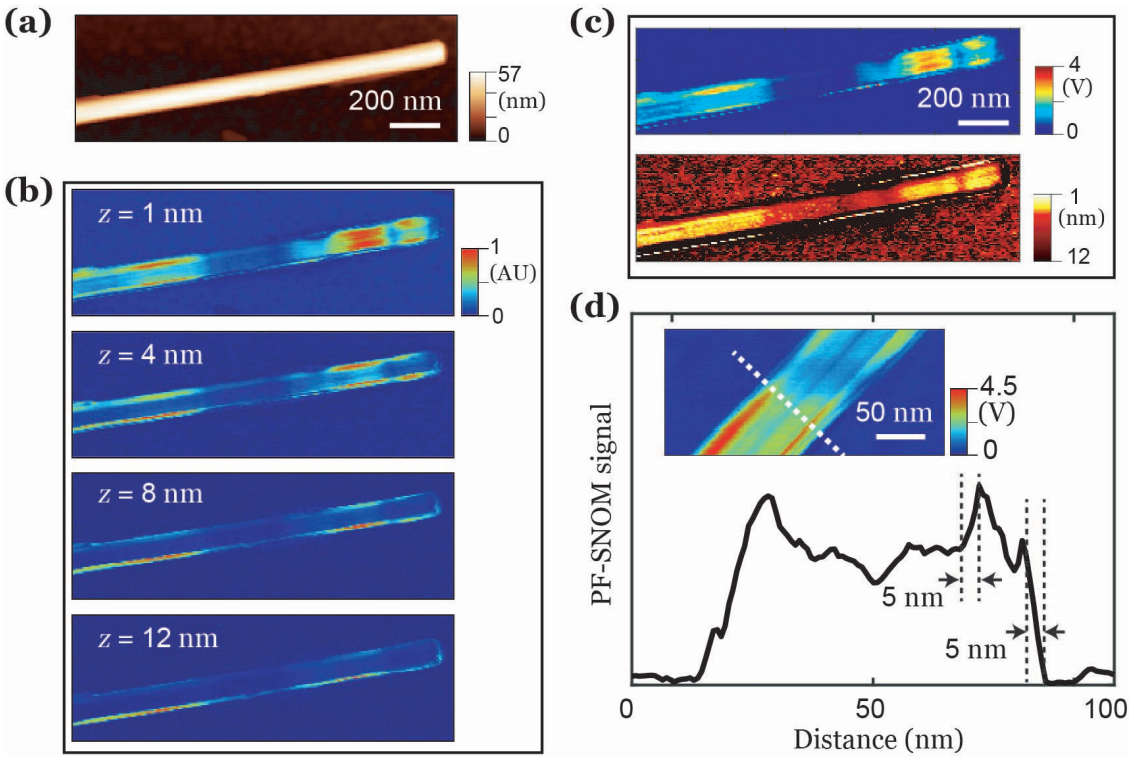

Figure 3. 5 Tomographic imaging and the spatial resolution of PF-SNOM.(a) AFM topography of a polaritonic BNNT. (b) Tomographic near-field images of the BNNT. The section tip-sample distance is increased from 1, 4, 8 to 12 nm, with decreasing signal

intensities. The spatial distribution of the phonon polaritons is revealed. (c) The total intensity and the decay range map obtained from tomographic images assuming an exponential decay. (d) The PF-SNOM signal profile across the BNNT (shown as the inset), a spatial resolution of 5 nm is obtained by estimating the distance between 10%-90% maximal signals across an edge.

Once again, polaritonic BNNTs are measured to benchmark PF-SNOM. Figure 3.5 displays tomographic near-field images of a single BNNT, along with total intensity and a decay range map on the same area, assuming an exponential decay for all sites. Strong near-field interactions along long edges of the tube are present, similar to the observation of bound electromagnetic fields from reconstruction s-SNOM. It is also observed that the decay range of sites with strong near-field signals is much smaller than that of other areas with weak near-field signals, which confirms the strong near-field confinement of phonon polaritons. Furthermore, a spatial resolution of 5 nm is estimated from PF-SNOM signals along the edge of BNNT (Figure 3.5(d)), even though the tip radius is estimated to be 30 nm. The much-improved spatial resolution of 5 nm over 10-20 nm of traditional s-SNOM results from the gap-mode enhancement when the plasmonic tip and the sample are very close.[115] Because the tip-sample distance in PF-SNOM is well-defined, one can section the 3D near-field data cube at a minimal tip-sample distance (e.g., $z = 1$ nm) to get high-resolution gap-mode enhanced near-field images. The vertical resolution in determining the real-time z is estimated to be 0.12 nm in PF-SNOM. The ability to fine-tune the tip-sample distance is not attainable in traditional s-SNOM.

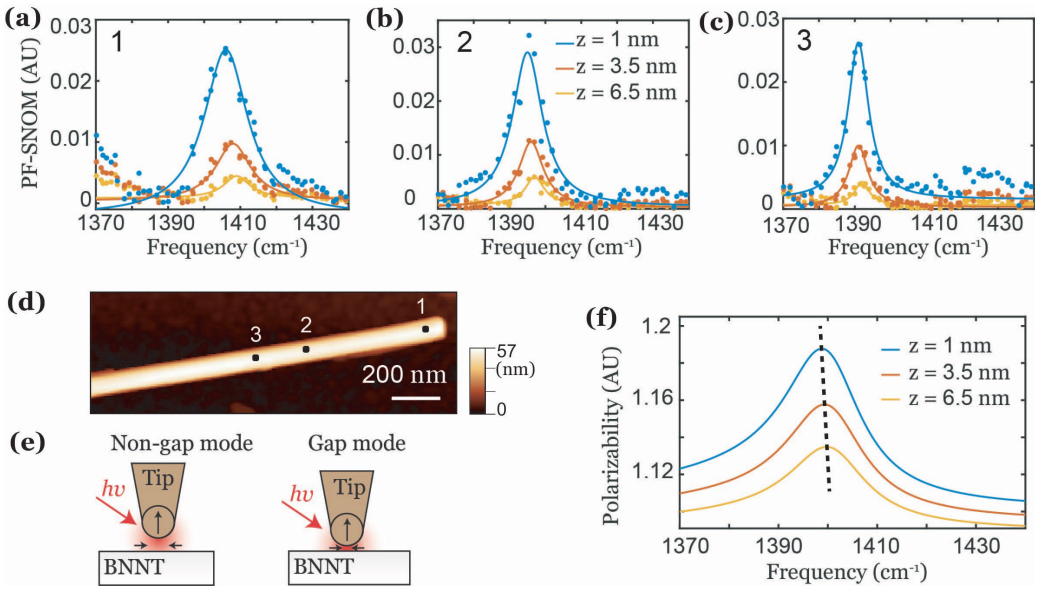

Figure 3. 6 The spectral behavior of phonon polaritons in the vertical direction.(a-c) Near-field spectra collected on locations 1-3 on the BNNT. Spectra are plotted in three different sectioning heights: 1 (blue), 3.5 (orange), and 6.5 (yellow) nm. Raw data are shown in dots, along with corresponding Lorentzian peak fittings. (d) Three measuring locations are labeled along the BNNT. (e) A comparison between the non-gap mode (when z is large) and the gap-mode (when z is small). In the gap-mode, the field between the tip and sample is more intense and confined. (f) Calculated near-field polarizability α_{eff} from the image dipole model used in s-SNOM (see Section 2.2). A redshift of the peak of phonon polaritons is labeled by a dashed line as the tip-sample distance z decreases.

Other than tomographic imaging, the spectral response of BNNT is also investigated by PF-SNOM, and the spectral dependence on the tip-sample distance is found. Figure 3.6(a-c) display spectra measurements on three different locations that are labeled in Figure 3.6 (d). Near-field spectra on three locations on the same BNNT show distinct peaks: as the measuring location moves further from the tube terminal, the resonance peak of phonon polaritons ω_p firstly redshifts from 1407 to 1396, then to 1391 cm^{-1}. This redshift is attributed to the fact that polaritons with lower energies and longer wavelengths are relatively low-loss; thus, they are more present at spatial locations where the distance to the reflecting terminal is far. Focusing on the spectra of each measuring spot, a unanimous

feature becomes clear: ω_p redshifts as the tip-sample distance decreases. The spectra property is detailed by fitting each spectrum using Lorentzian function, and the results of the resonance peak ω_p and full width at half maximum (FWHM) are listed in Table 3.1 below:

Table 3. 1 Extracted near-field spectra properties.

Location / z (nm)	Location 1		Location 2		Location 3	
	FWHM (cm^{-1})	ω_p (cm^{-1})	FWHM (cm^{-1})	ω_p (cm^{-1})	FWHM (cm^{-1})	ω_p (cm^{-1})
1	13.7 ± 2.4	1406 ± 1	10.3 ± 2.1	1395 ± 1	7.3 ± 0.8	1391 ± 1
3.5	12.3 ± 3.1	1408 ± 1	8.5 ± 2.0	1396 ± 1	6.6 ± 1.8	1391 ± 1
6.5	11.1 ± 4.1	1409 ± 1	7.4 ± 2.5	1397 ± 1	5.8 ± 2.7	1392 ± 1

Table 3.1 enlists two interesting features that were rarely touched in previous s-SNOM studies. The first redshift phenomenon observed when the tip-sample distance z decreases is again demonstrated by data, although the shift is very small (1-3 cm^{-1}). It is worthwhile to mention that the tip-sample distance term also appears in the image dipole model characterizing near-field signals observed in the light scattering, which was introduced in Section 2.2 and presented in Equation 2.2. To illustrate the spectral behavior as a function of the tip-sample distance, a calculation based on the image dipole model is carried out, and the redshift is reproduced in Figure 3.6(f). The convergence between experimental data and model prediction suggests that the observed redshift is likely from the interplay between the change in the sample's permittivity and the tip-sample distance. The second property comes from changes in FWHM: the linewidth (FWHM) broadens as z decreases. However, the image dipole model fails to reproduce this effect. We attribute this linewidth broadening effect to the formation of more relaxation channels when the tip-sample distance z is so small that an intense gap-mode enhancement with a large optical density of states is generated. This enhanced relaxation outcome is conceptually similar to the Purcell effect of fluorophores coupled to a resonant cavity,[116] and is also observed in

plasmonic-enhanced relaxation phenomena.[117,118] The image dipole model does not account for the formation of more relaxation channels when z is small. Later, on the measurement of silicon carbide sample, a more remarkable linewidth broadening is discovered. A revised image dipole model with a lossy term is then proposed to reproduce the broadening effect.

3.3.3 Vertical near-field spectral features of silicon carbide explained by modified image dipole and finite dipole models

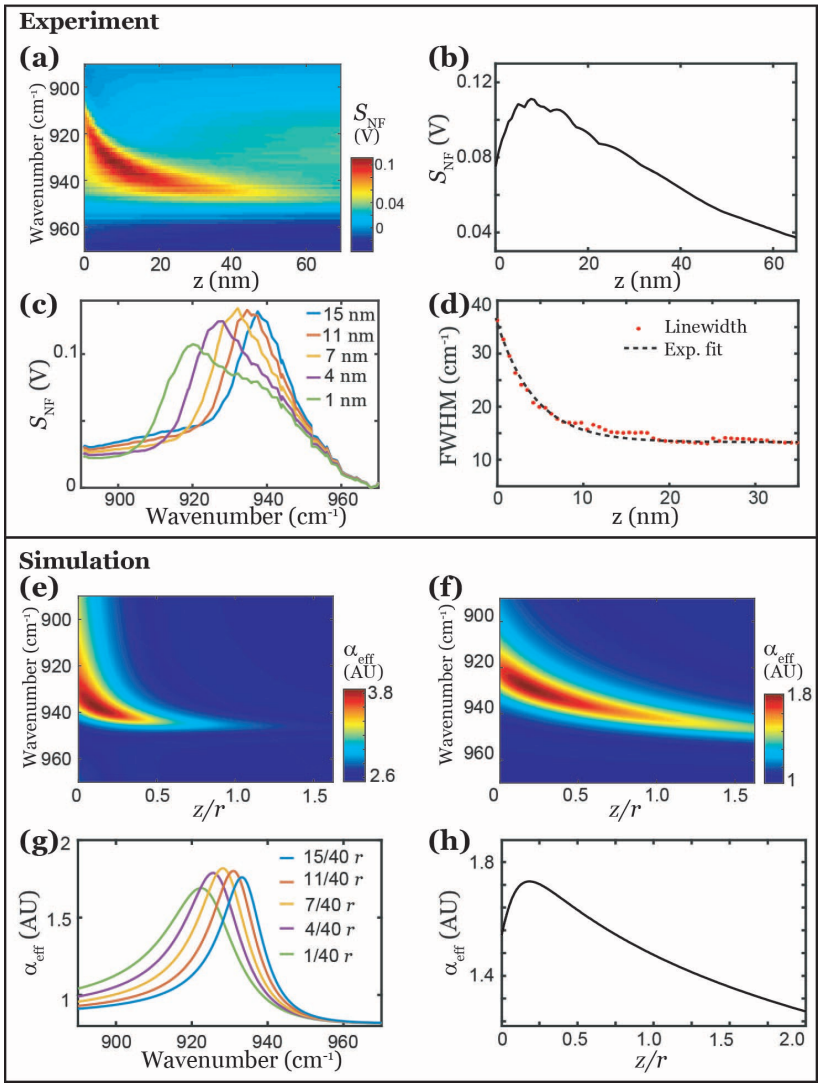

Figure 3. 7 Modified s-SNOM models based on PF-SNOM results. (a) Experimentally collected 2D near-field response of SiC. The scattering signal S_{NF} is represented by the

false-color intensity, and the X and Y-axis stand for the tip-sample distance z and the incident frequency, respectively. (b) A plot of S_{NF} vs. z sectioned along the X-axis from (a). (c) Near-field scattering spectra of SiC at five different z's, sectioned along the Y-axis from (a). (d) A plot of linewidth (FWHM) vs. z, overlapped with an exponential fit curve. (e-f) Simulated near-field responses in terms of effective tip-sample polarizability α_{eff} by using modified image dipole and finite dipole models. (g-h) A close look at the modified finite dipole model simulated result in (f). The linewidth broadening and the peak shift is reproduced in (g), and the anomalous vertical near-field interaction is reproduced in (h). The X-axis in (e), (f), and (h) is z/r, with r being the tip radius used in the simulation.

Silicon carbide (SiC) is a material that supports mid-infrared phonon polaritons.[119,120] The spectral response of SiC is recoded by PF-SNOM as well. Results are shown in Figure 3.7(a) as a false-color map of the scattering intensity, with the X-axis being the tip-sample distance z and the Y-axis being the incident frequency. Sectioning Figure 3.7(a) along the X-axis gives out an interaction curve at a selected incident frequency in Figure 3.7(b), and an anomalous non-monotonic trend appears in vertical interaction curves. This trend was not reported before, because vertical near-field responses are averaged out in the conventional s-SNOM. Similarly, near-field spectra sectioned along the Y-axis is plotted in Figure 3.7(c), where a large redshift and the linewidth broadening effect are revealed as z decreases. Although the image dipole model can predict the presence of the redshift as z becomes small,[120] neither the image dipole nor the finite dipole model can reproduce the linewidth broadening and the anomalous signal drop at close tip-sample distances.[86]

The anomalous signal drop at the close tip-sample distance may result from the phenomenon that the strong light field of phonon polaritons is damped by the engaging metallic tip.[121-123] To conceptually capture the increased damping at small z, we can modify both the image dipole and the finite dipole models by including a z-dependent term to the polarizability of the tip. This damping term characterizes the energy conversion from the nearfield to other dissipative energies, such as radiative emission via the tip acting as an

antenna. Using the image dipole (Equation 2.2) as the example, we can rewrite the tip's polarizability as:

$$\alpha_{\mathrm{mod}}(z) = 4\pi r^3 \frac{\varepsilon_{\mathrm{t}} - 1}{\varepsilon_{\mathrm{t}} + 2} e^{i\phi(z)} \tag{3.4}$$

Here, a damping term $e^{i\phi(z)}$ is introduced. The phase factor $\phi(z)$ represents the magnitude of the damping effect, as a larger $\phi(z)$ corresponds to larger damping. Therefore, $\phi(z)$ should reach the maximum when $z = 0$ and become zero when z is large. Because the exact form of $\phi(z)$ is not known a priori, for the sake of simplicity, we use an exponential form of $\phi(z) = ae^{-z/b}$ with adjustable parameters a and b to describe the damping phase factor. Substitute Equation 3.4 into Equation 2.2, we have:

$$\alpha_{\mathrm{eff}}(z) = \alpha_{\mathrm{mod}}(z)\left(1 - \frac{\alpha_{\mathrm{mod}}(z)\beta}{16\pi(r+z)^3}\right)^{-1} \tag{3.5}$$

Equation 3.5 is used to calculate the scattering spectra of SiC, and the result is shown in Figure 3.7(e). Compared with the unmodified image dipole model, Equation 3.5 successfully reproduces the linewidth broadening effect when z becomes small. The finite dipole model can also be modified by a similar treatment, and a simulation result from the modified finite dipole model is displayed in Figure 3.7(f). Figure 3.7(f) is very close to the experimental result in Figure 3.7(a), and specific comparisons are made between experimental results and simulations in terms of sectioned spectra (Figure 3.7(c) and 3.7(g)) and interaction curves (Figure 3.7(d) and (h)). The similarity between these results confirms that the linewidth broadening effect and the non-monotonic vertical near-field behaviors are all related to the tip-damping.

3.3.4 Correlative imaging enabled by PF-SNOM

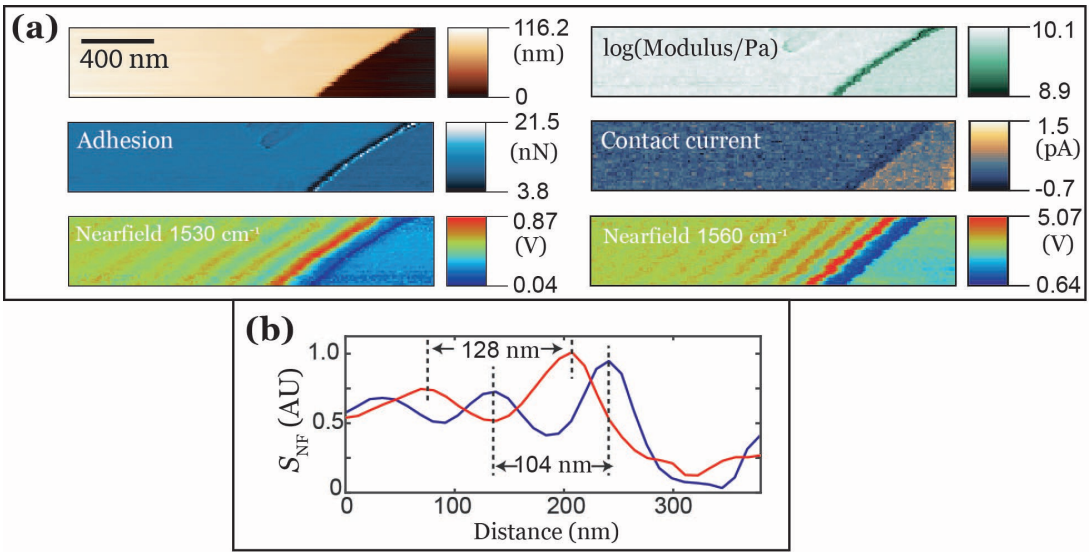

Figure 3. 8 Correlative multimodal imaging of PF-SNOM.(a) Correlative multimodal images from PF-SNOM measurement on the edge of a hexagonal boron nitride flake. The substrate is silicon. Multi-channel properties including logarithm of Young's modulus, adhesion, contact current and optical nearfield. (b) Line profiles of near-field fringe patterns on the edge of sample. Two periodicities of 128 and 104 nm are extracted from near-field images at 1560 and 1530 cm^{-1}, respectively.

Thanks to the dynamic tip-sample contact of PFT mode, mechanical and electric properties can be mapped simultaneously with optical nearfields using PF-SNOM. Figure 3.8(a) shows such multimodal measurements of a flake of hexagonal boron nitride with an 83-nm thickness on a silicon substrate. Topography, Young's modulus, adhesion, contact current, and near-field images at 1530 and 1560 cm^{-1} are obtained correlatively in the same sample region. Such correlative studies are not supported by the conventional s-SNOM with tapping mode AFM.

3.4 Revealing resonant conditions of an *h*-^{11}BN disk by PF-SNOM

3.4.1 Observation of two types of PhPs

Phonon polaritons (PhPs) are plasmon polaritons' counterparts in dielectric materials. Like plasmon polaritons, PhPs have a much more compressed wavelength than photons

and enable a locally enhanced electromagnetic field. Recent advances of 2D materials unveil a series of 2D materials that support PhPs,[22,124,125] one of the popular polaritonic 2D materials among them is the hexagonal boron nitride (*h*-BN). *h*-BN holds an anisotropy between in-plane and out-of-plane permittivities, which allows PhPs to travel inside the volume as so-called hyperbolic phonon polaritons.[72,126-128] The ultralow-loss hyperbolic PhPs are also observed in isotopically pure *h*-BN.[128] Photonic metamaterials are made of polaritonic building blocks such as disks, cones, and slabs, in which nearfields of each building block can interfere with each other. Thus, it is essential to understand the vertical near-field properties of nanoscale polaritonic structures. The 3D near-field mapping capability of PF-SNOM has been demonstrated on simple polaritonic samples such as BNNT and SiC. In this section, we will use PF-SNOM to reveal near-field properties on a micro-disk made of isotopically pure *h*-^{11}BN.[129]

The symmetry of circular optical nano-resonators results in symmetrical fringe patterns with high quality factors when on-resonance.[130-133] The investigated *h*-^{11}BN micro-disk, in our case, has a diameter of 9 μm and a thickness of 70 nm. The topography of the micro-disk is shown in Figure 3.9(a). Also, 3D near-field data cubes at a series of incident frequencies are obtained by PF-SNOM, and tomographic images from the XY-plane sectioning are displayed in Figure 3.9(b-d).

At first glance, near-field PhPs manifest as concentric circular fringes, which is in line with regular s-SNOM results.[129] The tip-enhanced light field specifically excites local PhPs that travel omnidirectionally. Then, traveling PhPs get bounced back at the disk edge and interfere with new-generated PhPs at the tip position. This process is conceptually similar to generating ripples by a pebble (tip) in a pond. As a result, circular fringe patterns are observed on the *h*-^{11}BN micro-disk. On the other hand, tomographic near-field images at different tip-sample distances *z* reveal extra details. As the sectioning *z* is increased from

1 to 5, then to 10 nm, the spatial distribution of fringes evolves as well. This evolution is not noticeable for tomographic images at 1420 cm^{-1} in Figure 3.9(b), however, fringes at 1425 and 1427 cm^{-1} in Figure 3.9(c-d) exhibit discernable changes: as z increases, the size of the most centralized fringe shrinks. In other words, excited PhPs at different tip-sample distances hold different polariton momenta. In sum, we can group our findings on tomographic near-field fringes into two categories: For the first category, such as at 1420 cm^{-1}, fringes do not change as a function of z; For the second category, such as at 1425 and 1427 cm^{-1}, fringes can evolve as a function of z. The latter category indicates that PhPs with various momenta are excited at different tip-sample distances.

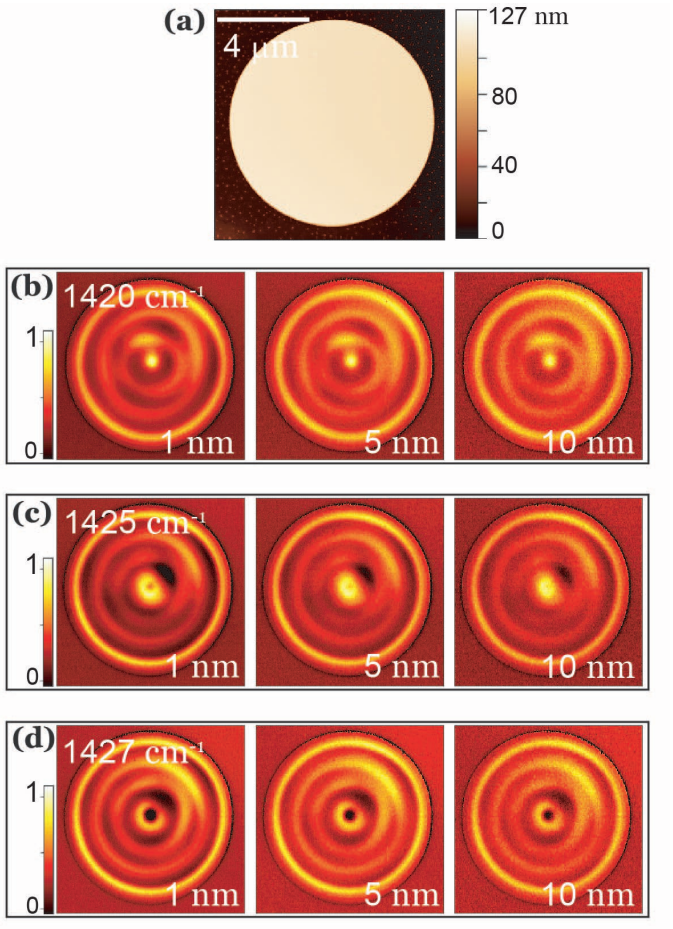

Figure 3. 9 Fringe patterns, vertical near-field signals, and dispersion relation of *h*-^{11}BN micro-disk. (a) AFM topography of an *h*-^{11}BN micro-disk with a diameter of 9 μm and a

thickness of 70 nm. (b-d) Normalized tomographic near-field images at tip-sample distances $z = 1, 5$ and 10 nm (in column) and incident frequencies $\omega = 1420, 1425$ and 1427 cm^{-1} (in row).

Spatial periodicities of the circular fringes observed in tomographic near-field images are extracted to obtain the dispersion relation of a plot of incident frequency (ω) vs. polariton momentum (q_p). The results are shown in Figure 3.10(a). Experimentally observed q_p exhibits a zig-zag trend along the predicted dispersion relation of PhPs based on the Drude-Lorentz model for dielectrics.[72] In the zoomed-in region of 1420-1430 cm^{-1} in Figure 3.10(b), previously observed two-category properties are reproduced in the dispersion relation: the momentum q_p of excited PhPs converges to fixed values of 2.5×10^4 and 2.85×10^4 cm^{-1} at incident frequencies ω around 1420 and 1428 cm^{-1}; Between these two values, however, q_p exhibits a dependence on z: decreasing q_p is observed as z increases. It is sensible to assume q_p has the z-dependence: the tip-enhanced light field can couple more momentum into the material and excite PhPs with larger q_p if the tip-sample distance z is small. This z-dependence is also illustrated by an FDTD simulation shown in Figure 3.10. But, why does the q_p not change with z at some incident frequencies such as 1420 and 1428 cm^{-1}? Later, we will explain this discrepancy by considering resonant conditions caused by the circular geometry of the h-^{11}BN disk.

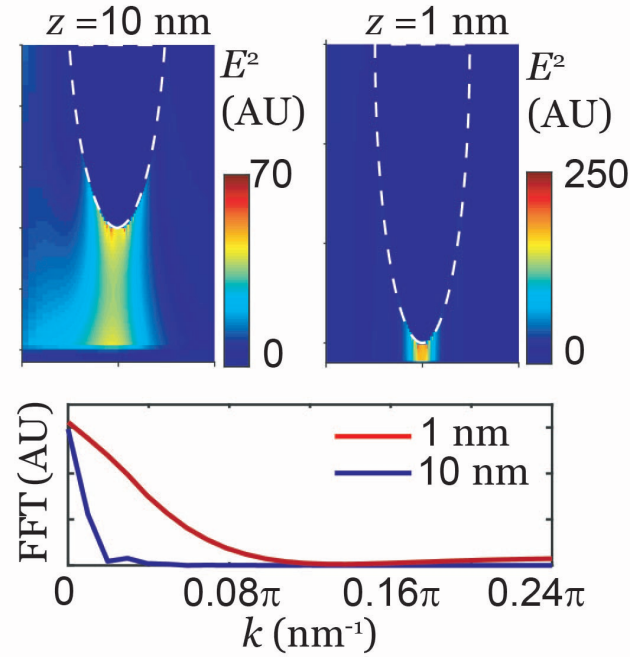

Figure 3. 10 Injecting momentum as a function of the tip-sample distance.FDTD simulations are conducted for two tip-sample distances at z = 10 and 1 nm. A close tip-sample distance at z = 1 nm provides not only a more confined and intense light field but also couples more injecting momentum, as shown in the comparison in the wavevector k space in the lower part. The tip used is a gold tip with a 30-nm end radius, the sample is silicon, and the incident frequency is 1403 cm^{-1}.

3.4.2 Formation of geometric resonances

Like a circular membrane of a musical drum that supports harmonic overtones,[134] the circular disk of h-^{11}BN has its resonant conditions. Vibrations close to one of the resonant conditions will be significantly enhanced. Resonant conditions of a circular disk had been solved analytically by examining standing wave solutions to a 2D wave equation.[132] The solution is expressed in terms of Bessel functions with polar coordinate $(r_\mathrm{p}, \theta_\mathrm{p})$:[129]

$$\rho = J_s(k_{sn} r_\mathrm{p} + \phi)\left[A\cos(s\theta_\mathrm{p}) + B\sin(s\theta_\mathrm{p})\right]e^{i\omega_\mathrm{a} t} \qquad \textbf{(3.6)}$$

in which ρ is the spatial charge density that is proportional to the spatial waveform of PhPs, J_s is the Bessel function of s^{th} (s = 0 or 1) order, ϕ is a correction phase factor that

accounts for the extra phase shift occurs on the reflection, A and B are arbitrary complex amplitudes, and ω_a is the angular frequency. The wavevector k_{sn} of PhPs is solved in:

$$J_s'(kr_0 + \phi) = 0 \tag{3.7}$$

with r_0 being the radius of the disk. k_{sn} equals to the n^{th} root in Equation 3.7. Considering the presence of the AFM tip and the generation of tip-induced PhPs, the majority of scattering signals is from the so-called roundtrip component, which is circularly symmetric and independent of θ_p.[132] Finally, experimentally observed fringe patterns are proportional to ρ^2 at resonant conditions, which is expressed as:

$$\rho^2 = J_s^2(k_{sn}r + \phi) \tag{3.8}$$

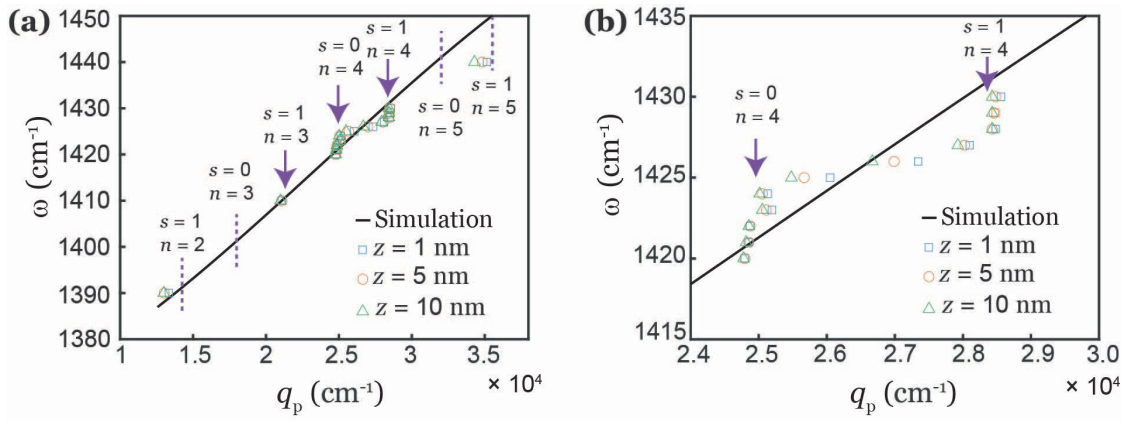

Figure 3. 11 Dispersion relation of PhPs confined in the disk.(a) The dispersion relation of the h-^{11}BN micro-disk extracted from tomographic near-field images. Experimental data (shown as markers) are overlaid with calculated dispersion relation (black curve). Calculated k_{sn} corresponding to three observed resonant conditions are shown as purple arrows; others are shown as dashed purple lines. Mode numbers (s, n) are displayed along with arrows and lines. Details in the 1420 – 1430 cm^{-1} region are enlarged in (b).

Therefore, we can solve a series of k_{sn} in Equation 3.7 and plug solved k_{sn} series back into Equation 3.8 to calculate observed fringe patterns. Solved k_{sn}'s are plotted in Figure 3.11 as vertical arrows and lines. Three k_{sn}'s with the mode number (s, n) of (1,3), (0,4), and

(1,4) coincide with experimental observed q_p's at 1410, 1420, and 1428 cm^{-1}. Because tip-launched PhPs at these three incident frequencies have momenta q_p's that are close to the disk's intrinsic geometric resonances with $k_{1,3}$, $k_{0,4}$, and $k_{1,4}$, the geometric resonance with k_{sn} can strongly enhance q_p's that match k_{sn}. For example, no matter how the incident momentum changes as a function of the tip-sample distance, only the portion of momentum that matches k_{sn} gets enhanced. This is the reason why experimentally observed q_p at 1410, 1420, and 1428 cm^{-1} does not change with z at geometric resonances. The simulation based on Equation 3.8 also replicates experimentally observed fringe patterns at three resonant conditions, as shown in Figure 3.12. These results confirm that the two types of PhPs showing different z-dependence in the h-^{11}BN micro-disk originate from the intrinsic geometric confinement of the micro-disk. At non-resonant conditions, the momentum of PhPs q_p drops as the tip-sample distance z increases; at resonant conditions, q_p keeps the same for a range of z.

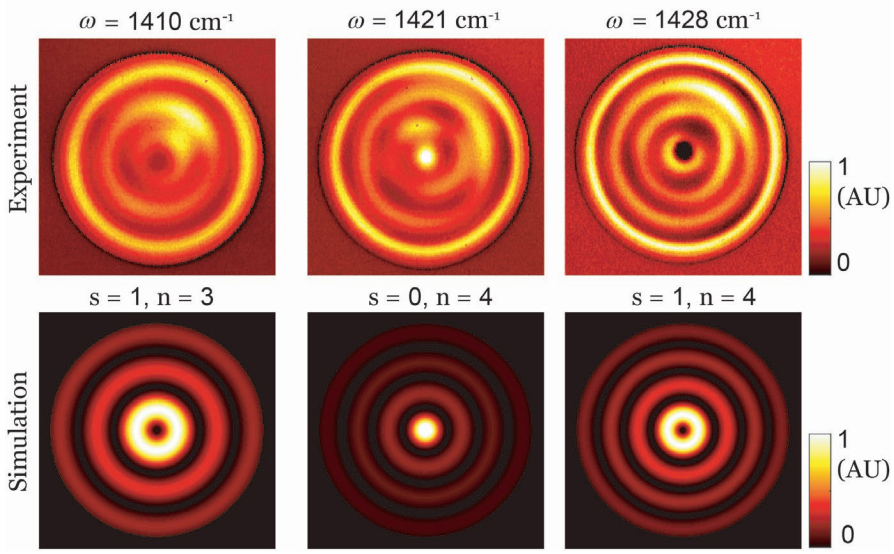

Figure 3. 12 Comparison between experimental observed and modeled fringes.Near-field images sectioned at $z = 1$ nm are shown in the upper row, and their corresponding simulations based on Equation 3.8 are shown in the lower row.

3.4.3 An *h*-^{11}BN edge with no geometric confinement

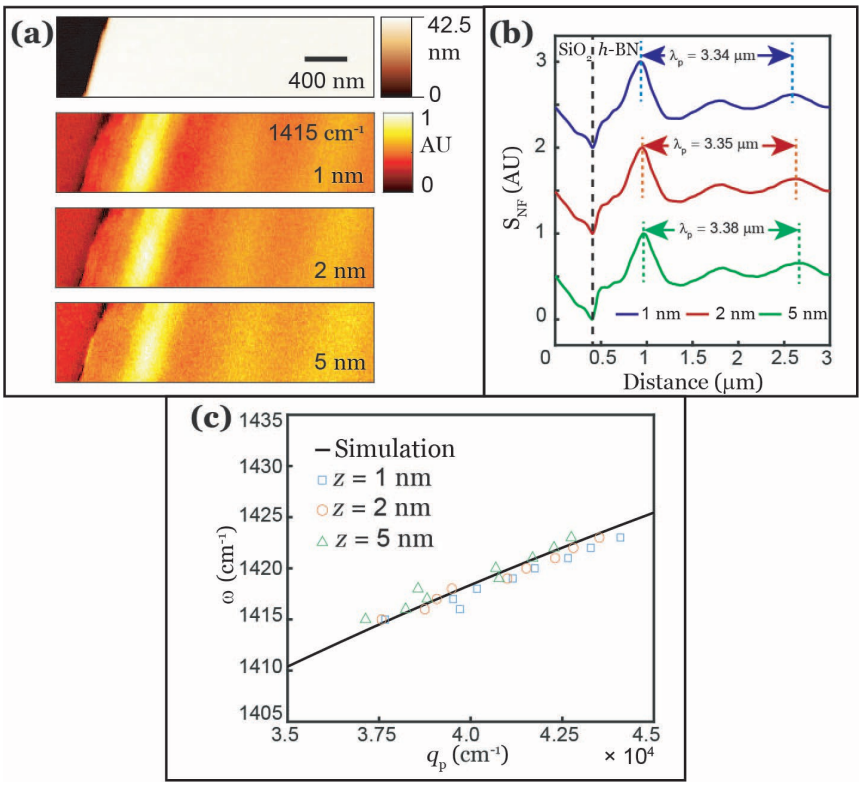

Figure 3. 13 Near-field analysis on the edge of an *h*-^{11}BN flake. (a) AFM topography and tomographic near-field images at 1415 cm^{-1} of an *h*-^{11}BN flake with a thickness of 40 nm. (b) Averaged profiles of near-field signals along the orthogonal direction to the edge. An increase of polariton wavelength λ_p (decreasing q_p) is observed as z increases. (c) Experimentally observed dispersion relation of PhPs overlaid with the simulation. q_p exhibits z-dependence at all investigated frequencies.

We have observed the focusing of PhPs' momenta by the geometric confinement of a micro-disk, it is then intuitive to investigate PhPs' momentum of an *h*-^{11}BN structure without any geometric confinement, such as a simple reflective edge. Figure 3.13 shows near-field images and the extracted dispersion relation of PhPs on the edge of an *h*-^{11}BN flake. As expected, no focusing effect of PhPs is observed, and changing the tip-sample distance z can fine-tune the polariton momentum q_p at every investigated incident frequency. In conclusion, the ability of PF-SNOM to map 3D nearfields results in two

gains: On the one hand, it allows fine-tuning of polariton momentum by changing the tip-sample distance; On the other hand, it provides a tool to detect whether the polaritonic structure is on-resonance. Neither of these two gains is achievable in the regular s-SNOM.

3.5 Summary and outlook

This chapter deals with two ways of obtaining 3D near-field scattering signals. One way is to improve over the conventional s-SNOM – devising a reconstruction algorithm to numerically reconstruct 3D near-field information, based on raw data from lock-in demodulation. The other way is more radical, and it uses completely different AFM working mode and signal acquisition method to attain 3D nearfield in a data cube experimentally. In practice, the second PF-SNOM method is preferred not only because it has a better spatial resolution, but also due to that the most important parameter used in mapping the 3D nearfield – the tip-sample distance – is controllable and well-defined in peak force tapping. As the cantilever is held stationary in peak force tapping, it has almost-zero kinetic energy before the tip-sample contact, leading to a highly sensitive response to the force exerted between the tip and sample. Thus, the practical tip-sample distance zero is accurately detected in the time domain by the cantilever motion of the snap-in moment.

The PF-SNOM results of BNNT and SiC samples suggest that the tip-enhanced light field is not just a scattering transmitter for probing the nearfield; it also acts as a damper at a short tip-sample distance. Anomalous vertical near-field behaviors obtained from BNNT and SiC samples cast an inevitable question on the reliability of traditional s-SNOM data. If the vertical near-field curve is not monotonic, how reliable is the s-SNOM signal, which is the averaged result from changing tip-sample distances, on representing actual nearfields? In this regard, PF-SNOM can remove the ambiguity caused by anomalous vertical nearfields and decipher a more accurate representation of near-field properties.

PF-SNOM has been demonstrated on fine-tuning phonon polaritons by changing the tip-sample distance and determining the resonant conditions from geometric constraints. These findings open doors for the study of a wide range of applications that rely on both spectral and spatial selectivity. For example, the highly confined hotspots generated under resonant conditions could serve as a platform for chemical sensing. For different molecules, the polaritonic nanostructure could also be tailored to match their specific IR absorptions.[133,135] Besides, the mode quantification of circular *h*-BN disks could also pave the way for fabricating momentum filters for selectively exciting and transmitting PhPs with the desired momentum. As a multi-modal technique that can perform in situ correlative nanoscale imaging, PF-SNOM has a vast application prospect in such systems.

In conclusion, the development of reconstruction s-SNOM and PF-SNOM adds a missing block of capturing vertical near-field signals into existing s-SNOM techniques. For the first time, 3D optical nearfields are completely characterized by the tip-enhanced light field in AFM. As one more dimension of near-field information becomes available, new physics that were rarely studied before can be unearthed, from which a wide range of photonic applications will benefit.

Chapter 4 Super-Resolution Infrared Spectro-Microscopy in the Liquid Phase

Realizing super-resolution IR imaging and spectroscopy in water has long been a tempting but challenging goal to pursue due to the diffraction limit and the strong background absorption by water. In this chapter, we will present a method based on detecting the photothermal expansion, named liquid-phase peak force infrared (LiPFIR) microscopy, to tackle technical difficulties met in the aqueous system and achieve the nanoscale super-resolution. This chapter will first start with a review of general PFIR microscopy in the air environment, followed by a brief overview of obstacles for implementing nano-IR methods in the aqueous phase. Then, ways of transforming PFIR into the aqueous phase are presented. Later, we benchmarked LiPFIR microscopy by using it to monitor physical, chemical, and biological transformations that occur in water, heavy water, and ethanol environments. Surprisingly, phonon polaritons, which are usually imaged by near-field scattering methods such as s-SNOM in the air, were firstly imaged in water by LiPFIR. A summary and outlook section is provided at the end.

4.1 Peak force infrared microscopy

Two types of IR nanoscopic techniques of photothermal induced resonance (PTIR) and photoinduced force microscopy (PiFM) have been introduced in Chapter 2. Their limitations have also been discussed in Section 2.5, as PTIR suffers from a poor spatial resolution caused by the tip scratching, and the PiFM signal tends to be unstable for uneven samples and requires special probes with high quality factors, while such requirement is extremely hard to meet in the liquid environment.

An alternative method using peak force tapping (PFT) was developed by Xu's group at Lehigh University and published in 2017, which is termed as peak force infrared (PFIR)

microscopy.[28] PFIR adopts a similar excitation scheme to PTIR but in a much gentler manner. In PFT, the tip only contacts with the sample intermittently, with an in-contact period of several tens of μs in every tapping cycle. Within each in-contact period, an external IR pulse is brought to the tip-sample region to excite the absorbing sample. Similar to PTIR, the energy absorbed is then quickly turn into the photothermal expansion and pushes the cantilever to vibrate at its contact resonances. The magnitude of this pulse-induced cantilever vibration is used as the signal in PFIR, which has been experimentally proved to be proportional to the sample's IR absorption. The signal generation mechanism of PFIR is illustrated in Figure 4.1.

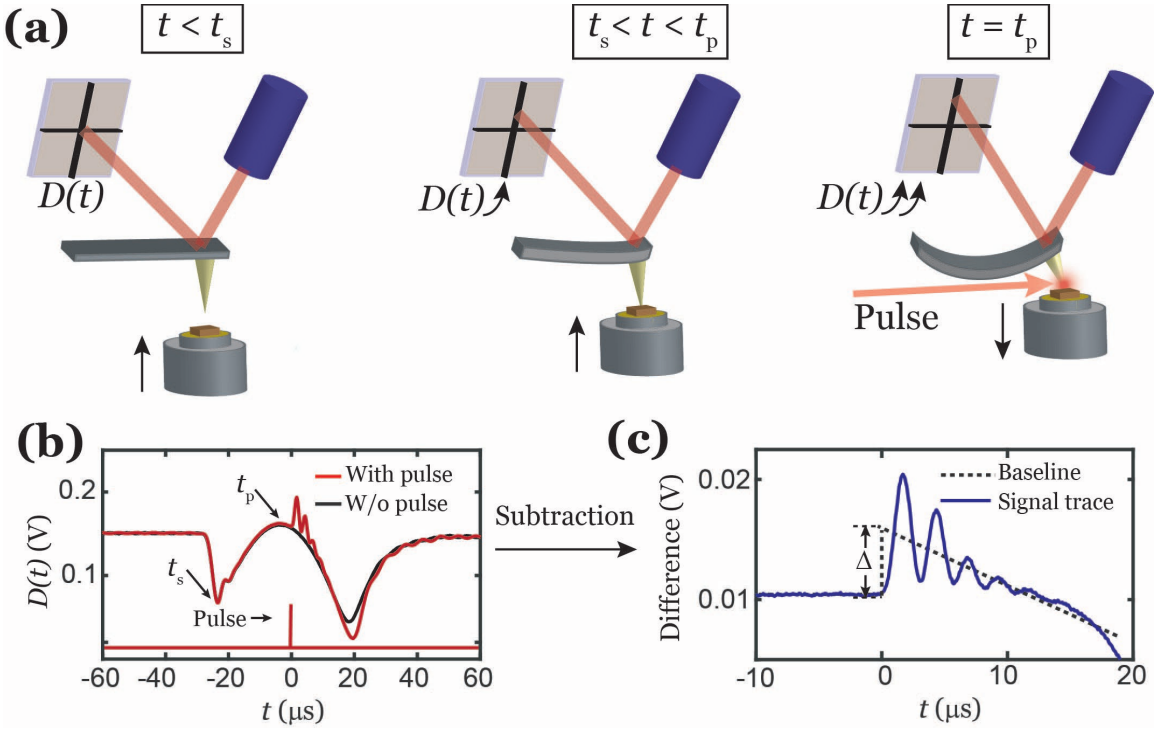

Figure 4. 1 Signal generation in PFIR. (a) In PFIR operation, when the cantilever is far away from the sample ($t < t_s$), the cantilever does not bend, and a small and constant $D(t)$ is recorded by the quadrant detector. After the snap-in point ($t > t_s$), the tip becomes in-contact with the sample, and a slight upward bend of the cantilever is recorded in the deflection signal $D(t)$. At the peak force point ($t = t_p$), an external IR pulse is guided into the tip-sample region, and the absorbing sample can push up the cantilever through the

photothermal expansion. Thus, a large increase in $D(t)$ is observed, and the cantilever starts to vibrate. (b) Experimentally monitored $D(t)$ at two conditions – with and without the pulse illumination. The pulse arrives at the peak force time point t_p. Subtracting the normal force curve (without pulse) from the excited force curve (with pulse) gives out a laser-induced deflection trace shown in (c). This self-subtraction scheme is realized by triggering the laser at half of the PFT frequency, so the force curve with and without pulse will be generated alternatively in time. The direct photothermal expansion Δ or the amplitude of ringdowns from Fourier transform is used as the PFIR signal.

Unlike the contact mode PTIR, the PFT mode PFIR limits the tip-sample in-contact time and therefore is less likely to scratch and damage the tip and the sample. Another difference in PFIR is the time window for the signal generation is much shorter than that of PTIR. The time window is mainly determined by the tip-sample in-contact period, which is usually tens of μs in PFIR. After the tip retraction, the cantilever's oscillation will be quickly damped, and the cantilever goes back to the stationary state for the next tapping cycle. While in PTIR, the cantilever's vibration can last for hundreds of μs (see Figure 2.6), which may make the AFM feedback loop unstable and damage the tip and sample. Most importantly, advanced PFT operations in commercial AFM are well-tuned and calibrated, allowing for the accurate peak force control and a much higher spatial resolution than that in contact mode. Sub-10 nm spatial resolutions were reported by using PFIR on a variety of samples: on block copolymer and boron nitride nanotube samples, a resolution of 10 nm was obtained;[28] on oil shale samples, a spatial resolution of 6 nm is demonstrated.[136] Such a high spatial resolution enables PFIR to image chemical compositions in unprecedented detail. For example, PFIR images of zymosan particles derived from cell walls of *Saccharomyces cerevisiae* are displayed in Figure 4.2, where polysaccharide backbones and protein-rich sites are mapped out around a bud scar *in situ*.[137]

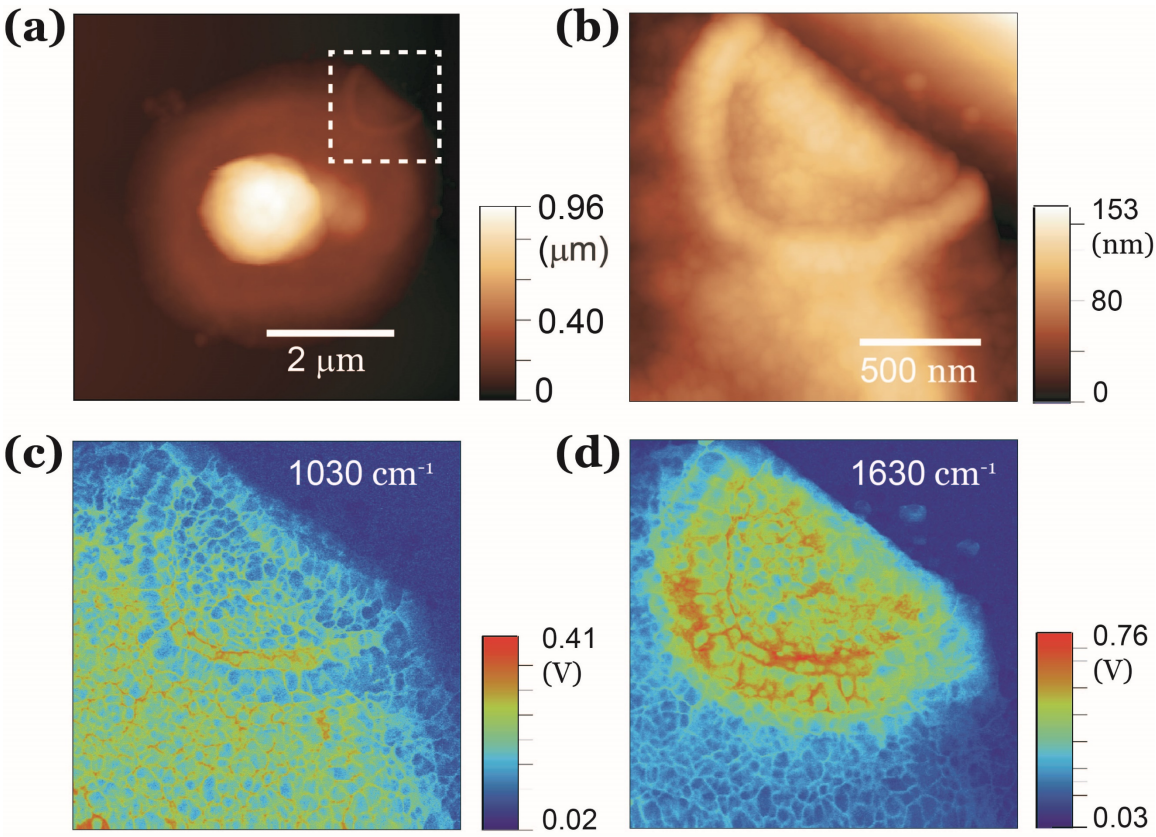

Figure 4. 2 PFIR measurements on a zymosan particle.(a) AFM topography of a zymosan particle. A bud scar is located on the upper right corner and is indicated by a white box. (b) Zoomed-in topography image of the bud scar, the imaging area is 1.3 × 1.3 μm². (c-d) PFIR images at 1030 (sugar chain) and 1630 cm^{-1} (amide), respectively. The zymosan surface is found to be polysaccharide-rich, and the interior of the bud scar is found to be protein-rich. Polysaccharides and proteins co-localize both inside and outside the bud scar and form a mesh-like backbone for the zymosan particle.

To systematically evaluate three nano-IR imaging techniques of PTIR, PiFM, and PFIR, Table 4.1 is made to compare three methods in multiple aspects. PFIR has the highest spatial resolution among the three and is most versatile for a wide range of samples.

Table 4. 1 Comparison between three nano-IR imaging techniques.

	PFIR	PTIR	PiFM
AFM mode	Peak force tapping	Contact	Tapping
Spatial resolution (nm)	6-10	25-100	<10-20
Laser power (W)	10^{-5}	10^{-4}-10^{-2}	10^{-4}-10^{-3}
Tip contamination	Low	High	Low
Rough & sticky surface compatibility	Yes	No	Challenging
Access to mechanical information	Yes	Partial	No
Liquid-phase compatibility	Yes	Yes	Challenging

4.2 Obstacles for IR measurement in the aqueous phase

The measurement of IR absorption provides information on the identity of molecular functional groups and their corresponding chemical environments. IR tools, such as FTIR, have long been popular methods for chemical identification. However, when measuring the IR property of the sample in the aqueous phase, two major problems appear. The first problem is generic for all IR methods: the spatial resolution is limited to the diffraction limit. The second problem is more stringent for the aqueous phase, as the absorption from water strongly attenuates the desired IR radiation, which is either used to excite the sample or to extract optical signals from. Thus, from the perspective of instrument design,

these two major problems can be separated into three parts: 1. The diffraction limit; 2. The light delivery; 3. The light detection.

During Chapters 2-4, a series of IR imaging and spectroscopy techniques were introduced and demonstrated. One common trait of all these super-resolution techniques is that a tip-enhanced light field is used as a scanning probe to bypass the diffraction limit. The same method can be used to enhance the spatial resolution in the aqueous phase as well. Additionally, in PTIR, PiFM, and PFIR, IR absorption is mechanically detected on-site by the cantilever motion, no optical detector is needed, which simplifies the instrument design since the light detection is no longer an issue. In most aqueous AFM operations, the whole cantilever is immersed inside the liquid. The problem remains, then, is how to deliver the exciting light field efficiently into the tip-sample region, where the sub-wavelength plasmonic enhancement can be generated.

The light delivery problem for IR spectroscopy in the aqueous phase can be solved using the geometry of attenuated total reflectance (ATR).[138] In ATR configuration, IR beams are guided to the top surface of an ATR crystal at an incident angle that is greater than the critical angle. As a result, evanescent waves are generated from total internal reflection. The penetration depth of the evanescent waves depends on the light wavelength. It is usually around several microns, which means the energy is only distributed within a close range to the surface of the ATR crystal – where the sample is, leading to a reduced background IR absorption by water. By measuring the energy loss of incident beams, the sample's IR absorption profile can be recovered. Generally, ATR crystals are made of IR-transparent materials with high refractive indices, such as germanium, zinc selenide, diamond, and silicon. Figure 4.3 calculates the field enhancement and the penetration depth for the interface between water and germanium at 6.25-μm incident wavelength in

total internal reflection conditions.[92] The closer the incident angle to the critical angle, the larger the field enhancement, and the higher the penetration depth is.

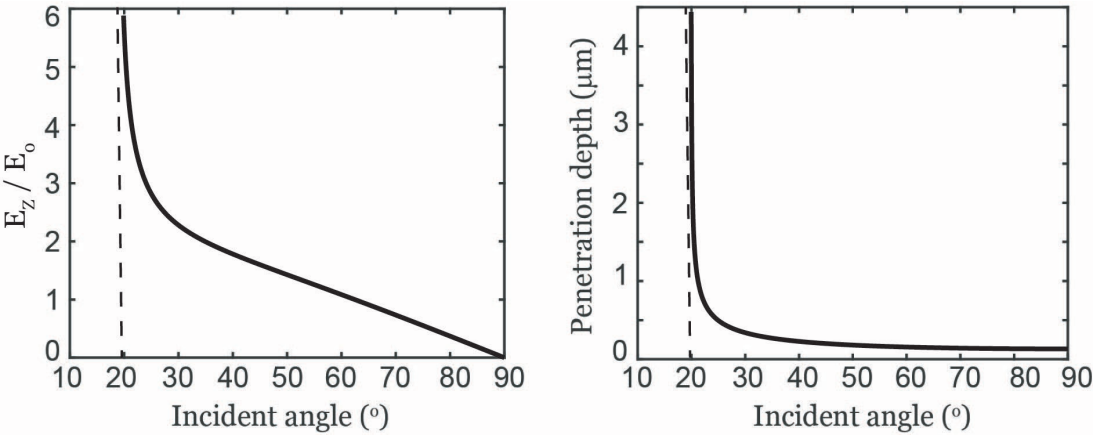

Figure 4. 3 Calculated field enhancement (left panel) and penetration depth (right panel) for total internal reflection.The field enhancement is represented by the ratio between the amplitude of the vertical field E_Z and the incident field E_0. The critical angle at 19° is shown as vertical dashed lines in two figures.

It is then worthwhile investigating whether the evanescent field in the ATR geometry can be used to deliver the light field into the tip-sample region. An FDTD simulation is conducted for the ATR geometry in Figure 4.4. Remarkably, the evanescent field can be further enhanced and confined by the plasmonic tip, leading to a light field distribution similar to that in ambient conditions with the side illumination (Figure 1.7). The chemical sensitivity in the ATR geometry is also demonstrated by the simulated spectrum of PMMA, in which the water absorption diminishes. The simulation results suggest a nanoscale chemical imaging tool based on the tip-enhanced light field is plausible in the aqueous phase.

Some PTIR setups use zinc selenide prisms to achieve total internal reflection conditions in the ambient environment (see Section 2.3), and the ability of PTIR to work in the aqueous condition for imaging cells, protein aggregates and polymer patterns had already

been demonstrated.[51,93,94] However, the spatial resolution in these studies was low due to the intrinsic limitations of PTIR (see Section 2.5). Besides, the strong drag felt by the cantilever in the aqueous systems can significantly lower the quality factor (Q) of cantilever resonances, causing an inevitable drop in the signal to noise ratio. This effect also renders the PiFM method tricky to implement in the aqueous phase, since the cantilever easily loses its well-behaved high-Q eigenmodes in water. So far, only large samples with thicknesses of hundreds of nm and sample that absorbs strongly in IR like PMMA were measured by PTIR in fixed liquid environments of water or heavy water.

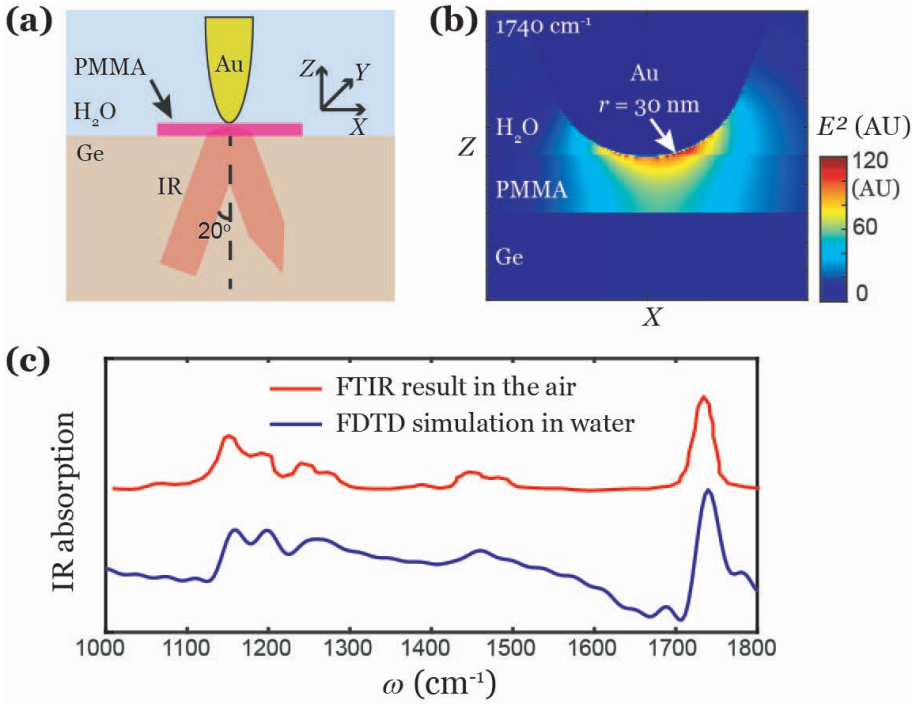

Figure 4. 4 FDTD simulation of the tip-enhanced light field in water and its chemical sensitivity. (a) The scheme used in the FDTD simulation. A 20-nm thick PMMA layer is put on the top surface of germanium, and a gold tip with an end radius of 30 nm is in contact with the sample. IR beams are illuminated from the bottom at an incident angle of 20° to achieve total internal reflection. (b) Simulated tip-enhanced field under absorbing 1740 cm^{-1} illumination. A strong, slightly distorted enhanced field is presented underneath the tip. (c) Simulated IR spectrum of the PMMA layer. Characteristic peaks of PMMA are reproduced.

On the other hand, the development of a liquid-phase IR nanospectroscopy is still tempting, because so many life-related chemical and biological transformations happen in aqueous systems. These systems are often delicate, multi-component, and intricate. Tracking them with IR would be ideal because IR is generally non-destructive and label-free. The rest of this chapter will deal with the development and demonstrations of liquid-phase peak force infrared microscopy, which delivers *in situ* monitoring of physical, chemical, and biological transformations with sub-10-nm spatial resolution.

4.3 Liquid-phase peak force infrared microscopy

4.3.1 Working principle of LiPFIR microscopy

The signal generation mechanism of liquid-phase peak force infrared (LiPFIR) microscopy is almost the same as that of PFIR and is drawn in Figure 4.5. However, two improvements over the original methods used in PFIR have been made. First, the single-pulse excitation scheme is replaced by the multi-pulse excitation. Matching the repetition rate of IR pulses to the cantilever's contact resonances results in an enhanced signal-to-noise ratio.[139] This enhancement is especially desirable for LiPFIR because induced cantilever oscillations are smaller than that obtained in ambient conditions (Figure 4.5(b-c)). Second, the self-subtraction scheme is no longer in use in LiPFIR. Instead, laser pulses are introduced during every PFT tapping cycle, and laser-induced cantilever vibrations are extracted by mathematical treatments (Figure 4.5(c)). This adjustment doubles the speed of signal acquisition in LiPFIR. A germanium (Ge) prism is used as the ATR crystal, and IR beams are brought from the bottom at an incident angle of 21°. The tip and sample are all immersed into water inside a fluid chamber during experiments.

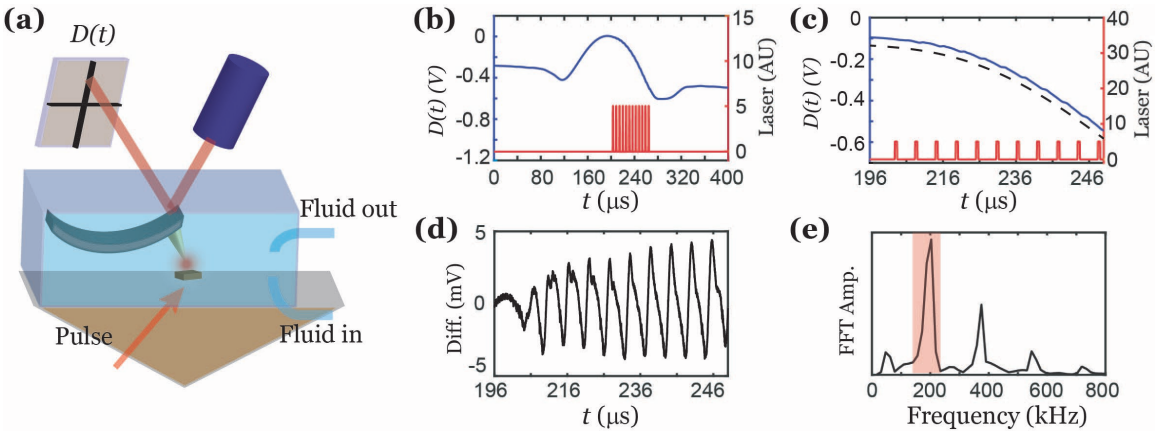

Figure 4. 5 Signal generation in LiPFIR. (a) The ATR geometry used in LiPFIR. The cantilever is immersed in a fluid chamber on top of the Ge prism. The cantilever deflection $D(t)$ is monitored simultaneously with the timing of input laser pulses. (b) Simultaneously recorded $D(t)$ and laser pulses in the time domain. A train of pulses arrives after the peak force point. (c) A zoomed-in view of the force curve with laser pulses. Small vibrations present in the force curve, and a slow-varying background (black dashed curve) from polynomial fits can be isolated from the force curve. The background is offset vertically for a better comparison. (d) Extracted laser-induced vibrations of the cantilever, by subtracting the slow-varying background from the force curve in (c). Vibrations induced by the train of incident pulses with the repetition rate that matches the contact resonant frequency of the cantilever. (e) FFT of (d). A large peak around the contact resonance of 200 kHz is observed along with a series of multiples. Usually, the area underneath the first peak is used as the signal in LiPFIR.

The combination of the ATR geometry with PFIR is not as sound straightforward. For example, since IR pulses come from the bottom to form a total internal reflection condition at the water/Ge interface, the height of the sample stage should be held constant if the light path of incident beams is fixed. Another concern is the change of tip position. The focus spot of IR beams at the water/Ge interface has the diffraction-limited size of several microns, and the tip should always be positioned inside the focus spot to maximize and stabilize the tip-enhancement. Requirements mentioned above set a rule of thumb for the choice of AFM: for a scanning AFM, the sample stage should move in the XY-plane while

the cantilever should move along the Z-axis. In practice, a different AFM make (Bruker Bioscope Catalyst) is used to achieve the ATR scheme. Also, because Ge is opaque with the visible light, laser alignment in LiPFIR becomes an issue. Technical drawing of the LiPFIR setup, laser alignment methods, and other technical details are included in Appendix II.

4.3.2 Monitoring nanoscale surface reorganization of polymer blends

Polymer blends formed by spontaneous phase separation serve as a model system to test the capability of the LiPFIR method. Figure 4.6(a) shows the topography of the polymer blend film formed by polystyrene (PS) and polymethyl methacrylate (PMMA) in heavy water. Depending on parameters of the sample preparation, spin-coated PS:PMMA blends can take different phase-separated geometries that cannot be distinguished simply from topography. Two types of domains are noticeable in the topography: higher circular islands and a lower matrix region. To perform the chemical identification, the incident laser is tuned to infrared frequencies that correspond to vibrational resonances of PS and PMMA, respectively. Resulting infrared images are displayed in Figure 4.6(b-c). At 1492 cm^{-1}, PS domains exhibit a larger photothermal expansion signal as aromatic C=C bonds absorb strongly at this frequency. At 1725 cm^{-1}, PMMA domains are highlighted due to the absorption of the carbonyl C=O vibrations. Figures 4.6(b-c) allow chemical identification of the domain compositions in the liquid phase: the higher islands in the PS:PMMA blend polymer film are PMMA domains, and the lower matrix is the PS domain.

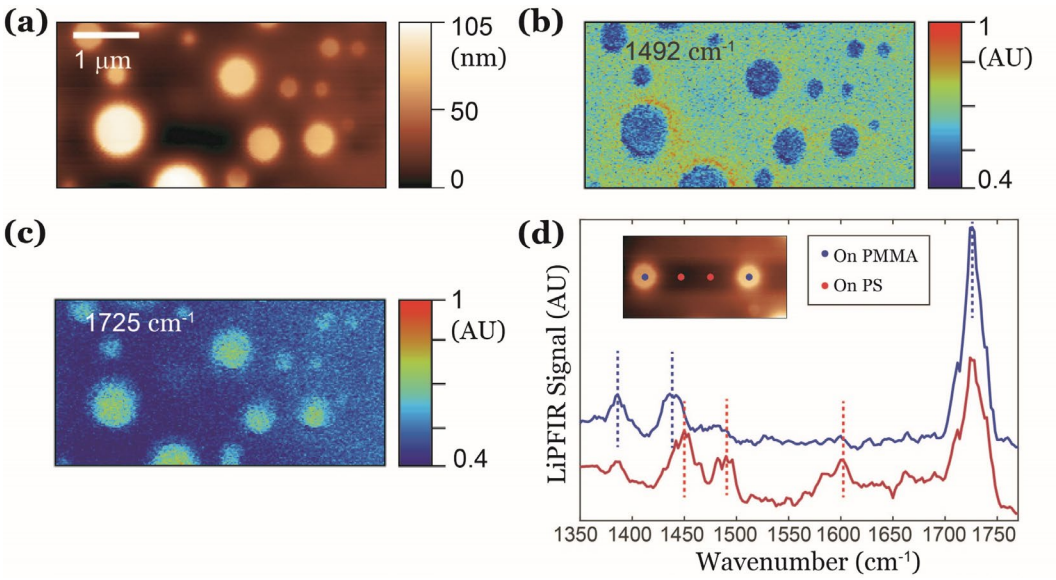

Figure 4. 6 LiPFIR imaging and spectroscopy on PS:PMMA blends. (a) AFM topography of the PS:PMMA polymer blend. Circular islands protrude from the lower matrix. (b-c) LiPFIR image of the same area at 1492 and 1725 cm^{-1}, respectively. PS and PMMA domains are highlighted separately. (d) LiPFIR spectra collected from multiple locations on the PS:PMMA blend film. Inset shows the topography of a 3×1.5 μm^2 area, where measuring locations are labeled as points. Two measurements on each domain were made and averaged spectra are shown. Spectra are offset from each other for a better comparison. Characteristic PS and PMMA absorption lines are marked by red and blue dashed lines, respectively.

Point spectra collected with LiPFIR are shown in Figure 4.6(d). When the AFM tip is fixed on circular islands, the averaged spectrum shows IR signatures of PMMA. Besides a strong carbonyl absorption peak at 1725 cm^{-1}, there are also two peaks at 1380 cm^{-1} (α-methyl group vibration) and 1445 cm^{-1} (methyl C-H vibrations). In comparison, the averaged spectrum obtained from the PS domain shows absorption peaks at 1450 cm^{-1}, 1495 cm^{-1}, and 1601 cm^{-1}, all from aromatic C=C vibrations of PS molecules. The distinctive spectra for PS and PMMA nanodomains indicate the succinct chemical sensitivity of LiPFIR. Note that the carbonyl peak at 1725 cm^{-1} of PMMA is also present in the PS domain, which is likely caused by bulk absorption of PMMA. The same effect was also observed in PS-b-

PMMA copolymers with standard PFIR,[28] as well as photoinduced force microscopy in the air.[27] These results demonstrate that LiPFIR is capable of distinguishing multi-component polymer domains through both infrared imaging and spectroscopy.

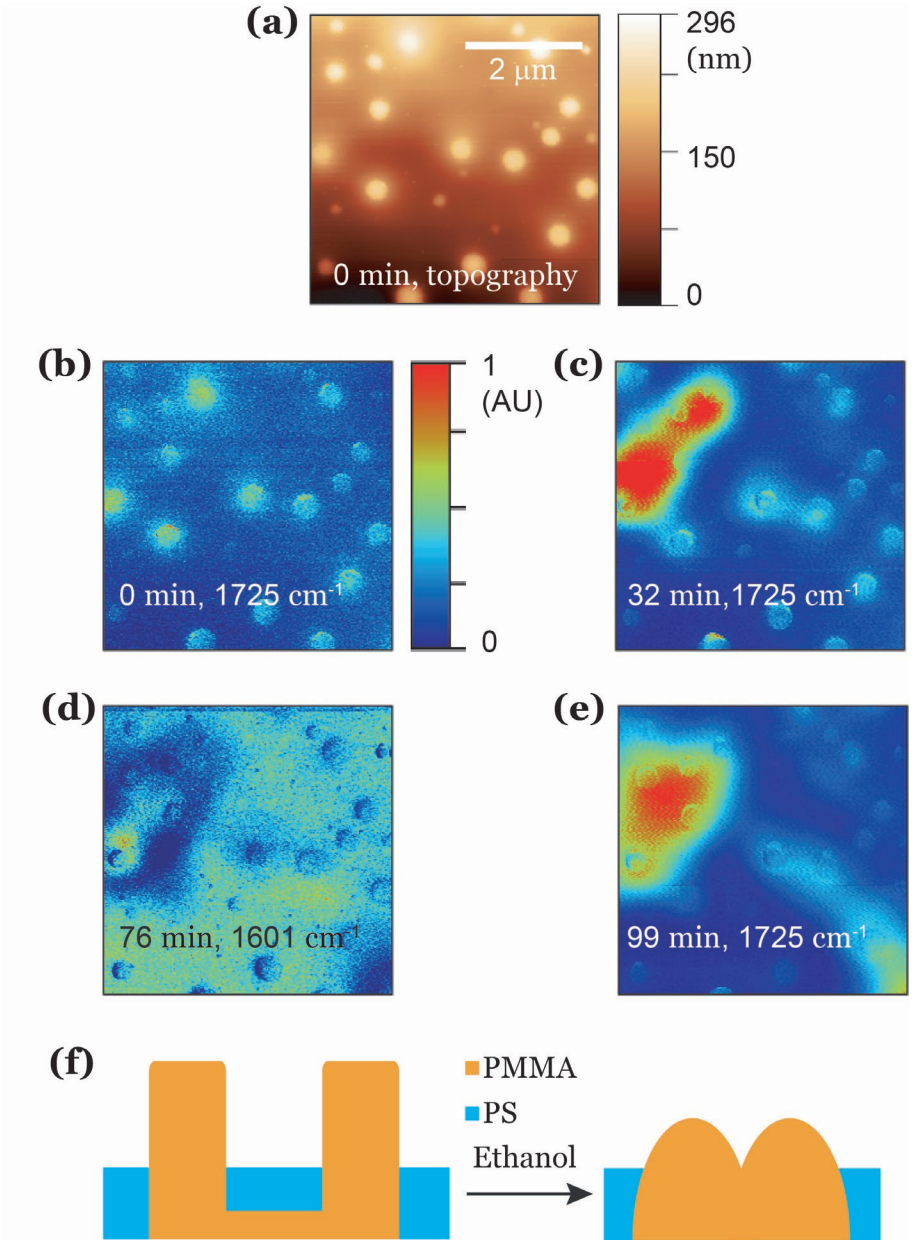

Figure 4. 7 Surface reorganization of PS:PMMA blends induced by ethanol.(a) Topography of PS:PMMA film in ethanol. (b-e) A series of LiPIFR images captured as a function of time after the immersion in ethanol. (f) Proposed mechanism of the surface reorganization.

In ethanol, PMMA can swell and rearrange motifs toward thermodynamic equilibrium between bulk ethanol and ethanol molecules dissolved in PMMA.[140] To illustrate this effect *in situ*, we use LiPFIR to monitor the surface reorganization of the PS:PMMA blend film. Figures 4.7(a-e) show the surface reorganization on a 5×5 μm^2 area of the PS:PMMA blend film as a function of immersion time. At the beginning, the topography of PS:PMMA blend film preserves the original phase-separated morphology in heavy water: islands are PMMA domains, and the lower matrix is the PS domain. This initial phase separation is confirmed by the infrared imaging at 1725 cm^{-1}. After 32 minutes, a larger PMMA domain emerges in the upper left corner. At 76 min, the infrared illumination is switched to 1601 cm^{-1}, and a PS-depleted region appears around the newly-formed large PMMA domain. After 99 min of immersion, a new large PMMA domain emerges in the lower right corner, while the area of the upper left PMMA domain is increased. As a result, the surface reorganization of the PS:PMMA blend film induced by ethanol propels the polymer blend pattern to evolve from its original configuration, to form larger phase-separated domains. The surface reorganization is dynamically captured by LiPFIR imaging. A schematic in Figure 4.7(f) is proposed to illustrate the swelling and coalescing process of PMMA domains.

4.3.3 Detecting H-D exchange on proteins *in situ*

Bovine serum albumin (BSA) is widely used as a model protein to study biological processes and applications.[141,142] The hydrogen-deuterium exchange (H-D exchange) method of proteins has found broad application in determining protein structure and solves questions related to protein interactions, energetics, and structural biology.[143] Infrared spectroscopy is suitable for studying the H-D exchange process since the replacement of hydrogen with deuterium significantly shifts the bond energy and changes

its infrared signatures.[144] However, most of the H-D exchange experiments are conducted with FTIR in bulk solutions, omitting the presence of nanoscale spatial heterogeneity.

LiPFIR is used to perform nano-imaging and spectroscopy of the H-D exchange process of BSA. Nanoscale infrared imaging of protein nanostructures is performed and shown in Figure 4.8. At room temperature, BSA proteins tend to form fibril structures in solution.[145,146] The Ge surface was silanized with APTES to immobilize proteins (see Methods and materials). AFM topography of a segment of a BSA fibril in 0.1×PBS buffer is shown in Figure 4.8(a). This single BSA fibril is 150 nm in height and 350 nm in width. LiPFIR images at 1630 cm^{-1} (amide I band, β-sheet) are shown in Figure 4.8(b-d) in water and heavy water environments. In water, a large infrared signal along the BSA fibril is observed, which distinguishes the protein fibril from the substrate. The spotty signals on the substrate are observed at interstices among the rough surface, where hot spots are created by strong field enhancements. In heavy water, amide I band infrared absorption is present in the fibril, although the signal intensity reduces compared to that in water. Another observation from Figure 4.8(c) is that a small region at the left end of the BSA fibril exhibits much reduced infrared signal at 1630 cm^{-1}. Figure 4.8(d) shows a zoomed-in image of this region. Such a difference indicates a change of protein secondary structure in this area.

To estimate the spatial resolution of LiPFIR imaging, a sectioned signal profile from the edge of the fibril is shown in Figure 4.8(e), and a spatial resolution of 8 nm is obtained for LiPFIR in water. By comparison, contact mode AFM-IR in water recently achieved a 20-25 nm resolution,[51,94] from a 100-nm spatial resolution in its early version.[93] The signal to noise ratio is estimated by dividing the average signal by the r.m.s of a small region (0.1 μm^2) on the fibril, and is calculated to be 34. Without any external plasmonic

enhancement, a signal to noise ratio of 34 surpasses the value of 5 obtained on the PMMA film in the resonance enhanced contact mode AFM-IR in heavy water.[51]

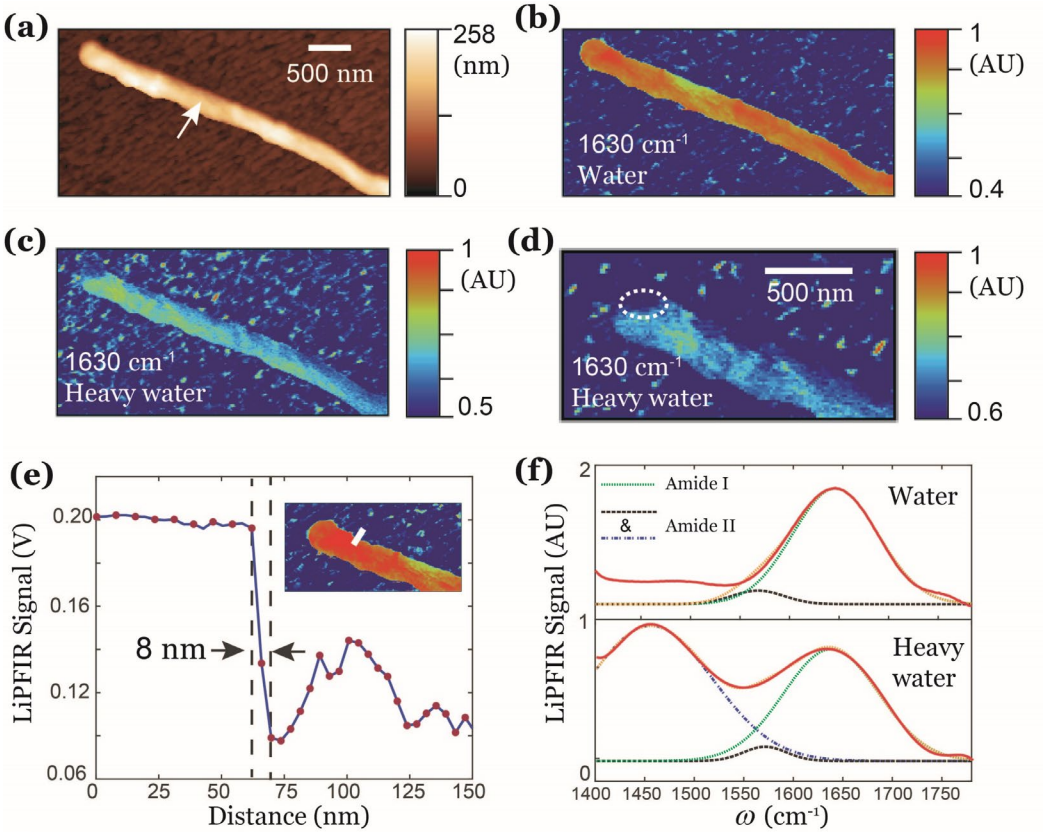

Figure 4. 8 LiPFIR imaging and spectroscopy study on H-D exchange of a BSA fibril.(a) Topography of a 150-nm high and 350-nm wide BSA fibril. (b) Infrared images of the BSA fibril in aqueous 0.1×PBS solution at 1630 cm^{-1}. (c) Infrared images of the same BSA fibril in heavy water at 1630 cm^{-1}. (d) Zoomed-in infrared image cropped from (c). The end of the fibril is indicated by an enclosure. (e) Signal profile from a high-resolution infrared image of the BSA fibril in water at 1630 cm^{-1} shown as the inset. A spatial resolution of 8 nm is obtained from the lateral distance between the signal maximum and minimum across the sharp edge of the fibril. (f) LiPFIR spectra of the BSA fibril in aqueous 0.1×PBS solution and heavy water. Infrared absorptions are deconvoluted into amide I (green) and amide II (black and blue) peaks. Measured spectra are shown in red, and modeled spectra from the peak deconvolution is shown in orange. The location of the spectral measurement is pointed by a white arrow in (a).

The H-D exchange is revealed by spectroscopic results obtained *in situ* on the same location of BSA fibril in water and heavy water. Measured infrared spectra are displayed in Figure 4.8(f). To reduce the background absorptions from water and heavy water, a baseline is obtained at a location on the substrate. It then is subtracted from BSA spectra. In both cases, a broad peak covering both amide I (1600 - 1700 cm^{-1}) and amide II bands (1500 - 1600 cm^{-1}) is observed. Because of the weak laser power of the QCL source at amide II band, a small amide II peak in water is obtained using the peak deconvolution method. When in heavy water, however, since the majority of amide II band absorption is from N-H bonds in proteins, the replacement of N-H with N-D bonds redshifts the amide II absorption from 1550 to 1460 cm^{-1}.[147] As a result, a strong amide II band of the BSA fibril is observed in heavy water, which centers around 1460 cm^{-1} and indicates the completion of H-D exchange.

4.3.4 Revealing protein denaturation induced by ethanol

Protein denaturation is a process in which higher-order protein structures decompose and lose their bio-functionality. The denaturation of proteins is often used in the biotechnology industry to purify protein products.[148] Ethanol, a widely available solvent, is a protein precipitant that is used in biomedical productions,[149,150] as well as used as a disinfectant. Ethanol does not have strong infrared absorptions around amide I and II bands and is miscible with water. Understanding the denaturation process at the nanoscale will bring fresh perspectives and insights into many related biochemical and biophysical processes. For example, the denaturation of protein can be triggered by a denaturant that facilitates the solvation of the hydrophobic region of proteins.[151] Infrared nano-imaging and spectroscopy of proteins that undergo the denaturation shall provide insights into the functions and activities of proteins.

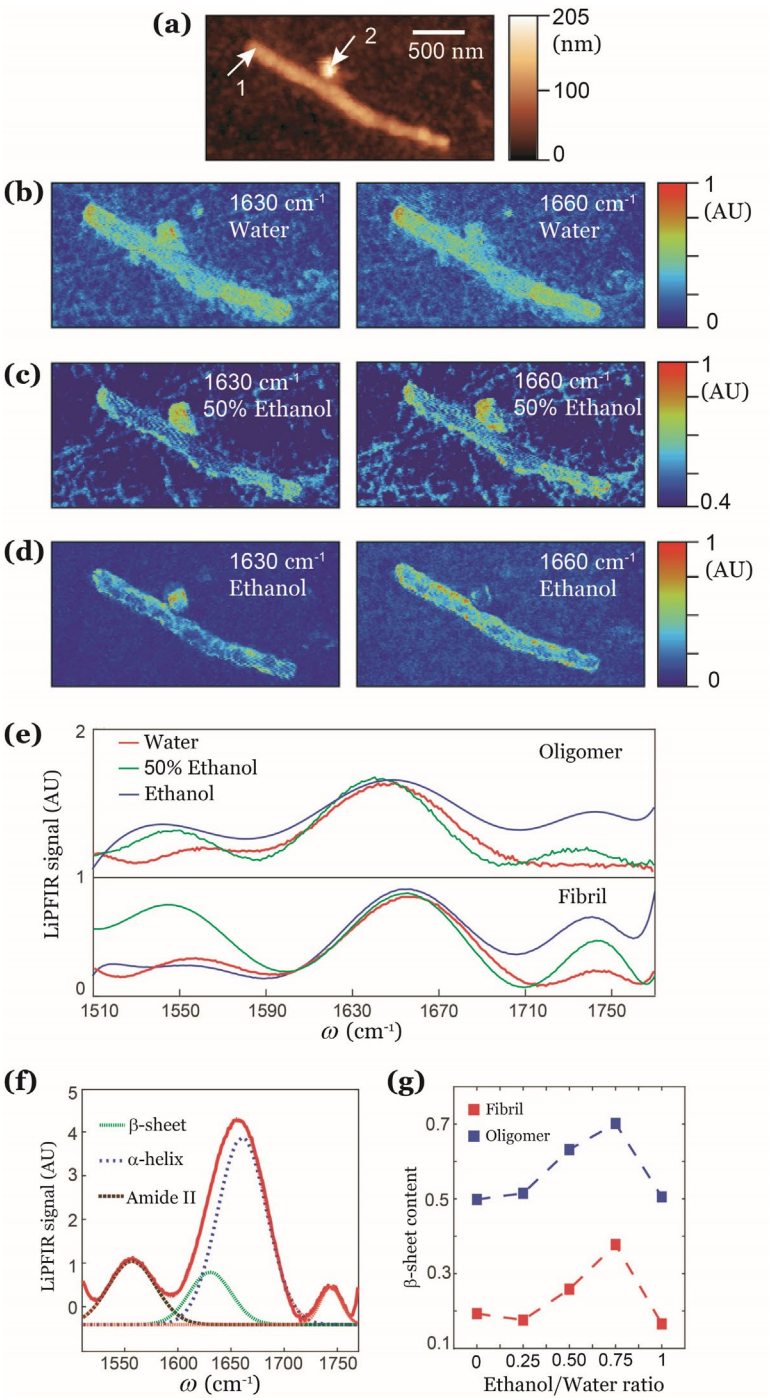

Figure 4. 9 BSA denaturation in ethanol. (a) Topography of a BSA fibril in water. The fibril is about 100 nm in height and 250 nm in width. A protein oligomer with a diameter of 200 nm is observed at the side of the fibril. (b-d) Infrared images at 1630 cm^{-1} (β-sheet) and 1660 cm^{-1} (α-helix) of the BSA fibril in water, ethanol/water 1:1, and 99% ethanol solutions. (e) Infrared spectra collected from two locations labeled in (a). Spectra are

normalized for optimal comparison. (f) Example of peak deconvolution. The infrared spectrum obtained in water is decomposed into four peaks around 1550 (amide II), 1630 (β-sheet), 1660 (α-helix), and 1740 cm^{-1} (carbonyl). (g) A plot of β-sheet content in amide I band vs. ethanol/water ratio. The β-sheet content is obtained from the deconvoluted peak area of 1630 cm^{-1} divided by the total peak area of amide I (1630 cm^{-1} and 1660 cm^{-1}).

The LiPFIR microscopy is used to study ethanol-induced protein denaturation *in situ*. Displayed in Figure 4.9 are infrared images and spectra of a BSA protein fibril undergoing denaturation with the addition of ethanol. Figure 4.9(a) shows AFM topography of a BSA fibril in water. The fibril has a dimension of 100 nm in height and 250 nm in width.

Figure 4.9(b-d) display the infrared images of the BSA fibril at two amide I frequencies under different ethanol/water compositions. Amide I absorption is mainly composed of C=O vibrations, which correlates with local environments of protein secondary structures. Infrared signatures of amide I band are widely used to determine secondary structures of proteins.[21] In our case, two major amide I peaks – one at 1630 cm^{-1} and the other at 1660 cm^{-1} – are used to respectively represent β-sheet components and α-helix components. In water (Figure 4.9(b)), the BSA fibril responds at both frequencies with uniformly-distributed IR absorptions. A small oligomer is also detected besides the fibril, with the signal at 1630 cm^{-1} slightly prominent than that at 1660 cm^{-1}, indicating this oligomer has more β-sheet contents. In 50% ethanol/water solution (Figure 4.9(c)), the signal intensity of both amide I peaks drops non-uniformly along the fibril, meaning that the secondary structure of the protein fibril has been affected. However, the oligomer's amide I absorption remains strong, indicating its secondary structure is still preserved under 50% ethanol/water solution. In 99% ethanol/water solution (Figure 4.9(d)), the signal intensity on the fibril at 1630 cm^{-1} is smaller than the intensity at 1660 cm^{-1}, suggesting that the BSA fibril becomes α-helix-rich in ethanol. In comparison, the oligomer exhibits

small signals at 1660 cm^{-1}, meaning that the α-helix conformation of the oligomer reduces in ethanol. The spatial and spectral variations in infrared images indicate that conformational change in the oligomer is different from that of the protein fibril when exposed to denaturation by ethanol. The oligomer is more resilient to the denaturation than the fibril at a medium ethanol concentration (50%), while the α-helix content in the oligomer is significantly reduced at a high ethanol concentration (99%).

Infrared spectra collected from the fibril (location 1 in Figure 4.9(a)) and the oligomer (location 2 in Figure 4.9(a)) are plotted in Figure 4.9(e). At both locations, a strong amide I band centering at 1650 cm^{-1} and an amide II band centering at 1550 cm^{-1} are revealed by LiPFIR. It is worthy to note that the addition of ethanol induces a band centering at 1740 cm^{-1}, possibly indicating the adsorption of molecules with carbonyl functional groups introduced by impurities inside the ethanol solvent. To quantitatively compare the conformational ratio between β-sheet and α-helix, the amide I band from the fibril (location 1) in water is deconvoluted at 1630 cm^{-1} (β-sheet) and 1660 cm^{-1} (α-helix), as shown in Figure 4.9(f). Spectra of the fibril and the oligomer in 25%, 50%, 75%, 99% ethanol are obtained, and the same deconvolution procedure is performed. The change of β-sheet content is plotted as a function of the ethanol/water ratio in Figure 4.9(g). The oligomer starts with 50% β-sheet content in water, while the β-sheet content of the fibril in water is only 20%. As the content of ethanol increases, the spectral response of the fibril and the oligomer exhibit a similar trend: the content of β-sheet firstly increases as more ethanol is added, peaks at 75% concentration, and then drops down at 99% ethanol concentration. This trend is consistent with the ethanol-induced conformational change obtained through ultraviolet circular dichroism spectroscopy.[152] Our observation suggests that the denaturation of protein nanostructures is not proportional to the ethanol concentration, and the most drastic conformational change is induced by 75% ethanol.

Similarly, the most effective ethanol concentration in killing bacteria and viruses is around 70%.[153]

4.3.5 Investigating yeast budding site in the liquid phase

Avoiding the destructive shear force means that the LiPFIR microscopy is suitable for imaging highly uneven soft matter samples with large height variations, such as structures from biological cells. Imaging such samples would otherwise be extremely difficult to achieve with the contact mode AFM-IR without causing surface damages. For instance, imaging artifacts were present in the contact mode AFM-IR (PTIR) images of a large living cell in water with a ~100 nm spatial resolution.[93] To demonstrate the capacity of LiPFIR in imaging large and soft biological samples, we use it to examine the chemical composition of large cell wall particles derived from the yeast *Saccharomyces cerevisiae*. These cell wall particles are often referred to as zymosan particles, which represents a group of naturally occurring immunomodulators for therapeutic applications.[154-156]

Zymosan particles exhibit different shapes in the air and the aqueous phase. Figure 4.10(a) shows the topography of a dried zymosan particle in the air. The dried zymosan particle exhibits a flattened disk-like shape with an average height of ~250 nm. In the dried form, the nucleus of the original yeast becomes noticeable and appears protruded from the center of the zymosan particle.[157,158] Another noticeable feature on the zymosan particle is the presence of a bud scar on the lower right. The bud scar is a ring-shaped fracture formed during the budding (division) process of yeast cells. We first perform air-phase peak force infrared microscopy on this zymosan particle. The sample is illuminated at 1030 cm^{-1} (C-O-C vibrations) and 1630 cm^{-1} (amide I band), to resolve the spatial distribution of polysaccharides and proteins spatially. As shown in Figure 4.10(b-c), the infrared image at 1030 cm^{-1} suggests that polysaccharide components, which mainly included β-glucan and mannan, are evenly distributed across the zymosan surface. In comparison, the

infrared image at 1630 cm^{-1} clearly shows the uneven distribution of proteins. Proteins are enriched in multiple scattered spots, the nucleus, and the bud scar. Other locations of the zymosan particle also exhibit a small infrared signal at 1630 cm^{-1}, indicating proteins are present together with polysaccharides on the rest area of zymosan surface.

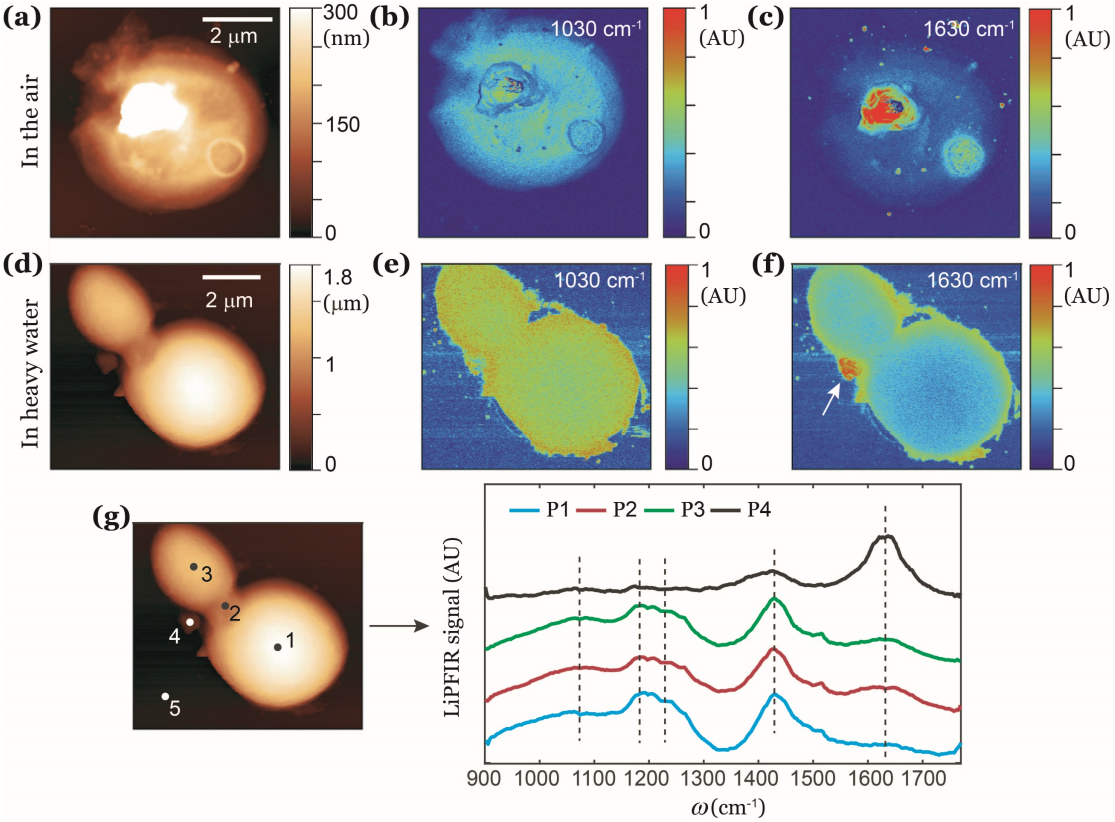

Figure 4. 10 LiPFIR imaging and spectroscopy on zymosan particles.(a) Topography of a zymosan particle in the air. The scale bar is cut off at 300 nm to provide better image contrast for the bud scar of low height. (b-c) Standard PFIR images of the zymosan particle in the air at 1030 cm^{-1} and 1630 cm^{-1}, respectively. (d) Topography of two zymosan particles in heavy water. (e-f) LiPFIR images of two zymosan particles in heavy water at 1030 cm^{-1} and 1630 cm^{-1}, respectively. (g) The left panel indicates four spots of measurement for point spectra (positions 1 to 4). Position 5 is used to collect the baseline. The right panel shows collected spectra from four different locations on the two zymosan particles. Peaks at 1080, 1190, 1220, 1430 and 1630 cm^{-1} are labeled with dashed lines.

Dried zymosan particles, after immersed in heavy water, restore to their native ellipsoidal shape with a height of larger than 1 μm. Figure 4.10(d) shows the topography of two zymosan particles in heavy water. The height of zymosan particles increases from 200~300 nm in the air to up to 1.8 μm in heavy water, and the large nucleus observed in the air disappears because it is now enclosed inside the shell of the zymosan particle. An unusual aspect of the AFM image of Figure 4.10(d) is that it captures two zymosan particles in the budding process with a septum formed in between. LiPFIR images are displayed in Figure 4.10(e-f). In Figure 5e, an even distribution of polysaccharides is observed. In Figure 4.10(f), the distribution of proteins also appears uniform, and slightly stronger signals present at peripherals, because the evanescent infrared field is stronger at lower heights from the Ge/water interface. Interestingly, strong 1630 cm^{-1} infrared absorptions that correspond to amide I are observed on a cluster of material close to the budding site, as indicated by the arrow in Figure 4.10(f). The cluster is connected with the budding septum from the bottom, as revealed by the LiPFIR images. Note that the chemical composition of the cluster cannot be simply determined as protein, chitin may also present, which also has strong infrared absorptions at amide I band and plays a role in the budding process.[159]

To further confirm the chemical composition of the cluster in the vicinity of the budding site, four point spectra are collected and shown in Figure 4.10(g). Positions 1 and 3 are taken on the two zymosan particles, and position 2 is on the septum. Locations 1-3 show similar infrared signatures of polysaccharides: The peak at 1190 cm^{-1} is attributed to the absorption of heavy water inside the zymosan particles; small infrared absorptions between 1000~1100 cm^{-1} and the peak at 1220 cm^{-1} are due to the C-O stretching, and the peak at 1430 cm^{-1} is attributed to C-H bending. The spectrum collected on position 4, which is the bright spot observed at 1630 cm^{-1}, however, does not show discernable

signatures of polysaccharide and chitin, which absorb around 1000~1100 cm^{-1}. Instead, a sole amide I band around 1630 cm^{-1} is observed. This finding confirms that the highlighted cluster observed at 1630 cm^{-1} is mainly composed of proteins, and a medium band around 1430 cm^{-1} is attributed to the H-D exchanged amide II band. The proteins in the cluster may participate in the synthesis of chitins during the budding process, as suggested by previous studies.[160]

4.4 Imaging phonon polaritons in water

4.4.1 Obstacles for operating s-SNOM in water

Our works in Chapter 3 are highly related to characterizing the vertical properties of phonon polaritons (PhPs) by using scattering-type methods such as the reconstruction s-SNOM and PF-SNOM. The excitation and detection of PhPs can potentially provide a route for nanoscale infrared sensing of molecular analytes,[161,162] as well as polariton-enhanced nanospectroscopy.[135,163] These studies should preferably be conducted in the liquid phase – ideally in water where most of the meaningful chemical reactions and biological transformations happen. Mass transportation in the liquid phase is higher than that in the air, allowing molecular analytes to reach PhP-active sensing sites quickly. However, either PF-SNOM or s-SNOM cannot be easily performed in water because difficulties of operating AFM in tapping mode and collecting scattering signals in water. Consequently, PhPs are only imaged in air conditions so far.

The challenge of using s-SNOM for probing mid-infrared PhPs in the aqueous phase is in three aspects. First, water strongly absorbs mid-infrared radiation. As a result, free-space delivery of mid-IR laser to the tip-sample junction, where tip-enhancement happens, is challenging. Second, s-SNOM requires optical detection of light scattered from the metallic AFM tip, which inevitably passes through water en route to the detector, strongly attenuating the signal. Third, the fluid creates a mechanical drag on the AFM cantilever

that makes its oscillation anharmonic in the tapping mode feedback.[164] Anharmonicity in the cantilever oscillations causes signal artifacts in the lock-in signal extraction of s-SNOM signals that requires pure harmonic cantilever oscillation. Similarly, if the incident optical field at the tip-sample region is non-uniform, e.g., in an evanescent field from total internal reflection illumination, even purely harmonic oscillation of the AFM cantilever can lead to background signals in the non-fundamental lock-in demodulation. Although s-SNOM can measure water-encapsulated biological samples covered with a layer of graphene in the air,[76] this bypassing approach is associated with complex operational procedures and is highly situational for certain types of samples. The direct and straightforward measurement in the aqueous phase for s-SNOM remains a challenge.

4.4.2 Imaging phonon polaritons in water by LiPFIR

On the other hand, plasmonic enhancement and PhPs are also detectable by measuring the photothermal expansion in PTIR, PiFM, and PFIR.[94,139,165-167] A rationale for this phenomenon is that a rapid change in the scattering indicates shifts in both the real and the imaginary part (loss) of the permittivity; thus local inhomogeneities in electromagnetic fields are detectable in both scattering (s-SNOM and PF-SNOM) and absorption (PTIR and FTIR) ways. By making use of the detection of photothermal absorption in water, which has been demonstrated for LiPFIR in the previous section, hyperbolic PhPs in *h*-BN are successfully imaged in water for the first time.[168]

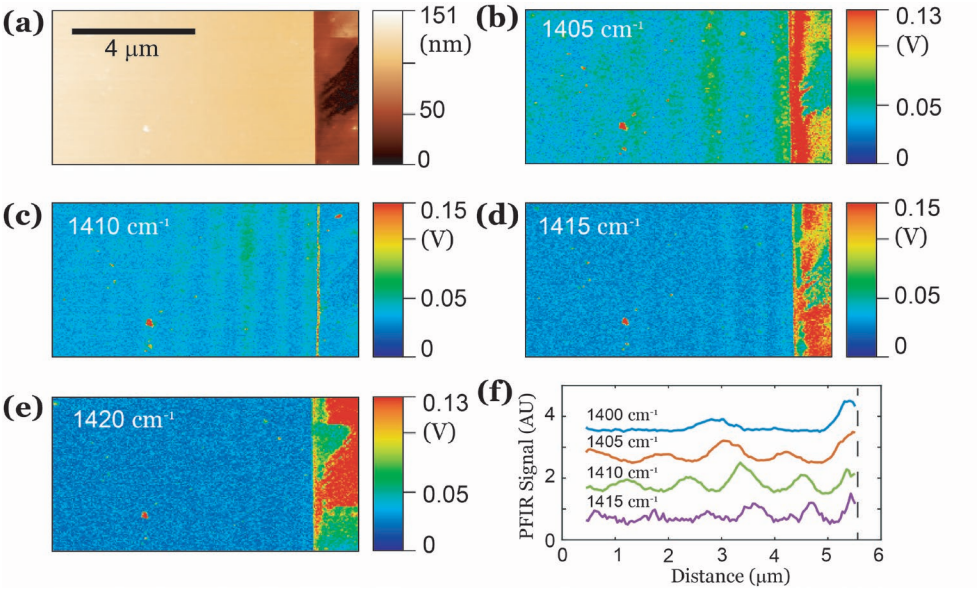

Figure 4. 11 LiPFIR images of phonon polaritons (PhPs) in water.(a) Topography of an *h*-^{10}BN flake with a thickness of 70 nm. (b-e) LiPFIR images at 1405, 1410, 1415, and 1420 cm^{-1}, respectively. Interference fringes of PhPs are noticeable in (b-d) but not in (e). (f) Averaged line scan profiles of observed PhP fringes.

Figure 4.11 displays LiPFIR images at a series of incident frequencies on a flake sample of *h*-^{10}BN. Isotopically pure *h*-^{10}BN is used because it supports PhPs with a much lower energy loss than naturally enriched *h*-BN and produces stronger photothermal expansion signals. Characteristic fringe patterns are detected in water from 1405 to 1415 cm^{-1} (Figure 4.11(b-d)). Above 1420 cm^{-1}, the fringes become too weak to detect (Figure 4.11(e)). The spacing of the interference fringes of PhPs decreases as the incident frequency increases, which is consistent with the general trend of the dispersion relation of PhPs. Averaged line scan profiles of the interference fringes from 1400 to 1415 cm^{-1} are shown in Figure 4.11(f), from which the spatial frequency of PhPs can be extracted. A bright dot on the lower left of the flake is observed in all LiPFIR images, which is likely a carbonate adhesive particle that absorbs strongly around 1400 cm^{-1} from the scotch tape used in the exfoliation process.[169] The same reason also explains strong signals observed on the substrate, because LiPFIR is also chemically sensitive.

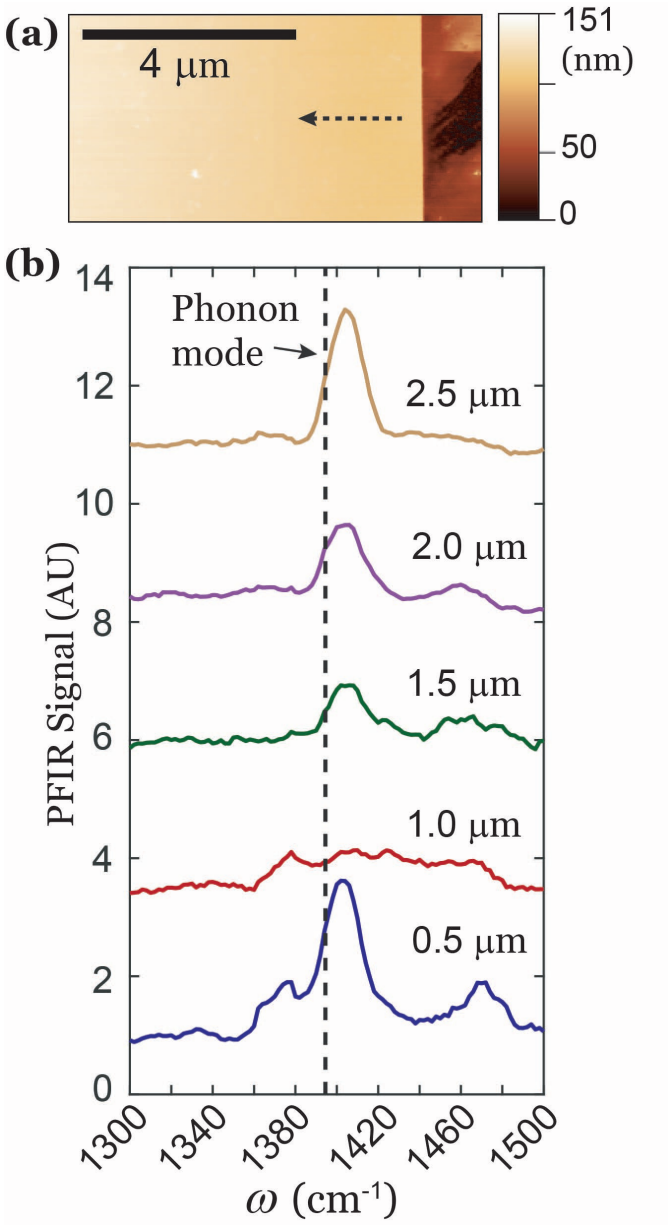

Figure 4. 12 Point spectra obtained from *h*-^{10}BN by LiPFIR. (a) AFM topography of the *h*-^{10}BN flake. Point spectra are collected at five different locations with a 500-nm interval along the black dashed arrow. The first point is 500-nm away from the edge. (b) Point spectra at five different locations on *h*-^{10}BN, which are offset vertically for better comparison. The black dashed line at 1395 cm^{-1} shows the intrinsic phonon mode of *h*-^{10}BN.

Point IR spectra are also collected by placing the AFM tip at specific locations and plotted in Figure 4.12. The main absorption peak at 1405 cm^{-1} is present at almost all probed

locations, which is off from the intrinsic phonon resonance at 1395 cm^{-1} of *h*-^{10}BN.[128] This offset is because PhPs are usually generated by the incident frequency that is higher than the phonon mode. When PhPs are generated in addition to the phonon resonance, the overall resonance profile shifts towards the blue side. This shift from the original phonon mode confirms that PhPs are detected by the LiPFIR. Moreover, a spatial variation of IR spectra at different probing locations is also observed. As the probing location progresses inward from the edge, the spectral response at 1405 cm^{-1} peak is maximized at 0.5 μm, drastically decreases at 1 μm, then gradual increases towards 2.5 μm. This modulation is caused by the spectral and distance dependence of the interference of phonon polaritons. As the tip brought from the edge to the left, it passes through crests and troughs of the first and the second interference fringes, thus different spectral response with high and low intensities at the peak of PhP are obtained. In the absence of PhPs, the spectra should be all the same across the homogeneous *h*-^{10}BN flake.

The dispersion relation of PhPs of *h*-^{10}BN is extracted through Fourier transforming spatial profiles in Figure 4.11(f) into the spatial frequency domain. Obtained PhP momenta are then correlated with the incident frequency. Figure 4.13 displays the experimentally observed dispersion relation of PhPs in water. The theoretical trend of the hyperbolic PhP dispersion relation in water is also provided as a false-color map in the same figure. Overall, the experimentally observed dispersion relation aligns well with the model prediction. In addition, the same *h*-^{10}BN is measured with the same LiPFIR apparatus in ambient conditions, and results are also shown in Figure 4.13. There is a clear difference between PhPs in the air and PhPs in water, suggesting that the dispersion relation of PhPs depends on surrounding dielectric environments. Different behaviors under different dielectric conditions form the basis of chemical sensing with PhPs.

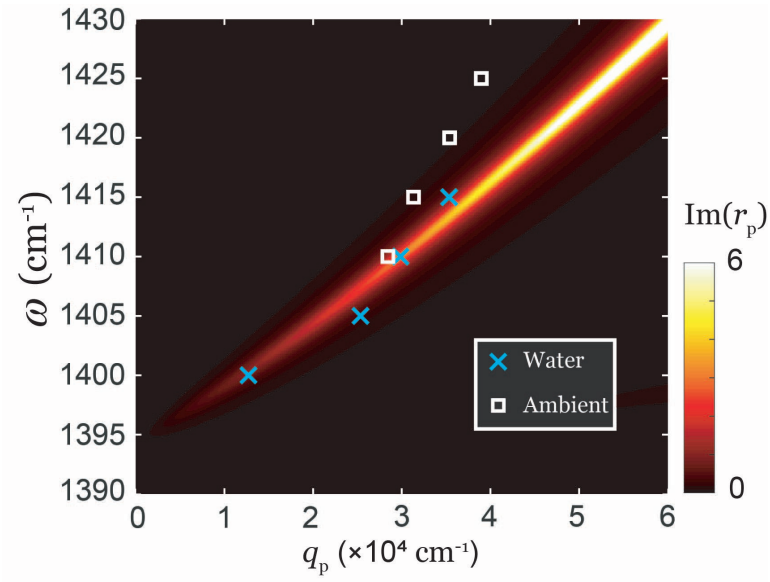

Figure 4. 13 Experimentally collected dispersion relation of hyperbolic phonon polaritons (PhPs) overlaid with the theoretical model.Experimental data collected by LiPFIR in water are shown as blue markers, and data collected in ambient conditions are shown as white squares. Note that PhPs of *h*-^{10}BN are not observable below 1410 cm^{-1} in the air, whereas they are not detectable by LiPFIR above 1415 cm^{-1} in water. Calculated dispersion relation of PhPs of *h*-^{10}BN in water is represented by the imaginary part of the reflectivity of an H_2O/*h*-^{10}BN/Ge structure. Details can be found in [129].

4.5 Summary and Outlook

The compatibility with liquid-phase environments, the high spatial resolution, and the chemical sensitivity enable LiPFIR to be a versatile platform for *in situ* monitoring of chemical transformations at solid/liquid interfaces in a non-intrusive and label-free fashion. Utilization of the fluid perfusion chamber permits the nano-infrared investigation on the same spot of interest under different aqueous conditions. This capability allows for studying a broad range of solid/liquid interfacial chemical and biological processes, such as heterogeneous chemical reactions and catalysis,[170] polymer membranes for biofouling mitigation,[171] DNA nanotechnology at the solid/liquid interface,[172] drug-protein interactions,[173] and functionalities of cell membranes.[174]

Nonetheless, there is still room for improvement. One of the immediate improvements over LiPFIR is to utilize a better working AFM system in water. Currently, we use the Bruker Bioscope Catalyst AFM, which only allows peak force tapping at maximal 1 kHz and has a noise level of r.m.s. 80 pm. A newer model named Bruker Bioscope Resolve has an improved noise level of 40 nm and can perform peak force tapping at 2 kHz. Combining these two factors, if we simply replace the AFM with the newer model, the signal to noise ratio of LiPFIR will be enhanced by a factor of 2.8 ($2\sqrt{2}$). Another improvement is to detect scattering light from the total internal reflection as well, as the addition of light detection can offer a direct comparison between the near-field scattering and photothermal expansion in the ATR geometry. Finally, although the requirement of a high-Q cantilever in LiPFIR is not as stringent as in PTIR, PiFM, and s-SNOM, since the multi-pulse excitation scheme is adopted to generate ringdown oscillations long enough during the short tip-sample in-contact time, a high-Q cantilever in water can still help improve the signal transduction in LiPFIR. Various methods can be used to change the interfacial property of cantilever and enhance its Q-factor in water,[175-178] which hints on the development of high-Q AFM cantilevers in the liquid phase.

The introduction of PFIR microscopy into liquid-phase systems enables many possibilities in method developments as well. The platinum AFM tip used in LiPFIR microscopy can be engineered to have unique catalytic properties; in this way, site-specific chemical reactions can be established and monitored through LiPFIR microscopy as the tip contacts and catalyzes the reactive sample surface. Another development would be introducing temperature control to the fluid chamber, allowing for studying the nanoscale chemical reactions under varying thermal conditions. One of the promising outlooks of LiPFIR would be its utilization in electrochemistry. The LiPFIR is fundamentally compatible with electric AFM by using conductive probe and substrate that are suited for liquid phases. By

using electrochemical approaches, many electrochemical reactions can be triggered and investigated *in situ* right underneath the tip.

Chapter 5 Developments beyond Current Techniques

In Chapters 3-4, we have built and benchmarked novel instruments with a radical shift from traditional contact and tapping modes to peak force tapping, to achieve 3D near-field characterization and in liquid IR spectro-microscopy. In this Chapter, additional works on renovations of existing methods will be introduced. The aim is to make two current techniques – standard s-SNOM and PFIR – "great again" through overhauling the existing methods from perspectives of signal acquisition and optics design. Throughout this chapter, we will prove that a pulsed laser source also works in standard s-SNOM. We will design a customized beam splitter with better stability for interferometric detections in s-SNOM. Finally, we will show that photovoltaic samples can be investigated with PFIR method simply by using a visible light source. As a result, applications of s-SNOM and PFIR are extended to a much broader range.

5.1 s-SNOM with a low-repetition-rate light source

5.1.1 Nyquist-Shannon sampling theorem in s-SNOM

As it has been already introduced in Section 2.2 and demonstrated in Section 3.2, the detection of scattering near-field signals in standard s-SNOM method relies on lock-in demodulations. In order to obtain demodulated outputs in the frequency domain, a continuous scattering signal in the time domain is needed as the input to the lock-in amplifier. Thus, a continuous wave (CW) laser is often used in the s-SNOM setup. A range of CW light sources has been used in s-SNOM, including gas lasers, free electron lasers, synchrotron radiation, heated thermal sources, and a plasma laser.[179-184] In these applications, the cantilever is oscillating at a fundamental frequency of several hundreds of kHz, and demodulated non-harmonic signals range from hundreds of kHz to several MHz.

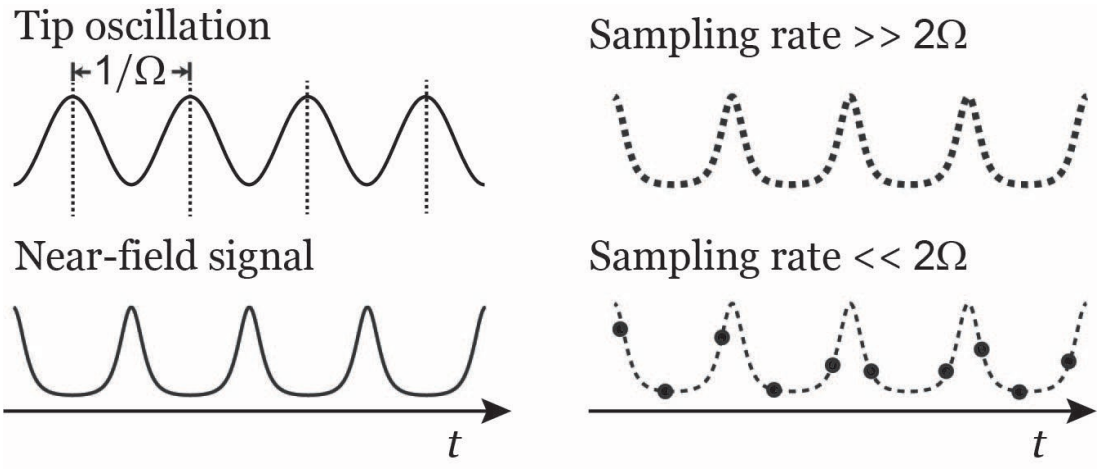

Figure 5. 1 Nyquist-Shannon sampling theorem in s-SNOM.In s-SNOM, the tip is oscillating at a frequency of Ω with a sinusoidal waveform, and the corresponding near-field signal also has a frequency of Ω. If one measures the near-field signal with a high sampling rate, important features such as crests and troughs in the original near-field signal can still be resolved nicely. However, if one uses a much lower sampling rate than 2Ω, obtained signals are only abstracts of the real signal, and information is lost.

According to the Nyquist-Shannon sampling theorem, for an effective sampling process, the sampling rate should be more than the critical rate, which is twice of the target frequency.[185] This theorem sets the lowest sampling rate for standard s-SNOM: to extract effective demodulated signals at $n\Omega$ Hz ($n \geq 2$), the repetition rate of the light source has to be at least $2n\Omega$ Hz. An illustration of Nyquist-Shannon sampling theorem is shown in Figure 5.1. Therefore, if one used a light source with a low repetition rate of less than $2n\Omega$ Hz in s-SNOM, the sampling rate would be insufficient to record enough sample data, and a faulty and noisy signal would be given by the lock-in amplifier.

However, low-repetition-rate light sources are beneficial for some applications. For example, the high per-pulse power of solid-state femtosecond sources at low repetition rates is suitable for frequency conversions through nonlinear processes, such as the difference frequency generation of mid-infrared radiation.[186] A general trend holds for ultrafast lasers: the higher the per-pulse power, the lower the repetition rate. For instance,

the mid-infrared outputs in the fingerprint region are on the order of a mere 1 mW from the solid-state Ti:Sapphire oscillator or Erbium fiber lasers with 40 or 80 MHz repetition rates.[187-189] In comparison, the output from an optical parametric amplifier pumped by a 250 kHz repetition rate Ti:Sapphire regenerative amplifier system could exceed 10 mW even 25 years ago.[190] The use of low-repetition-rate lasers with high per-pulse energy can enable many nonlinear optics effects to be pump-probed by s-SNOM.[77,191,192]

In the following section, we report a new signal acquisition scheme to make s-SNOM compatible with low-repetition-rate light sources. It turns out that Nyquist-Shannon sampling theorem can be fulfilled in the other way, and near-field signals from low-repetition-rate light sources are equivalent to those obtained with CW sources.

5.1.2 Principle and protocols of using low-repetition-rate light sources

In order to use a low-repetition-rate light source in s-SNOM and not break the rigorous Nyquist-Shannon theorem, it is important to reevaluate which portion of signals from the detected near-field scattering is really effective. In general s-SNOM operation, the sample surface gets scanned by the tip pixel-by-pixel. Consider obtaining a 256 × 256 pixel-size map in 22 mins and account for the trace and retrace motion at each scan line, the average time of the tip scanning on an individual pixel is about 10 ms. In terms of typing cycles, if the tip is tapping at 250 kHz, a 10-ms period will contain 2500 tapping cycles. Now, if we examine the waveform of near-field signals at a single pixel, this waveform should have a nice periodicity because the scattering signal is from the same spot of the sample. In other words, the 10-ms long waveform of the near-field signal is composed by replicating a short waveform from a single tapping cycle 2500 times in the time domain. Therefore, all near-field information is stored in this repeating waveform unit.

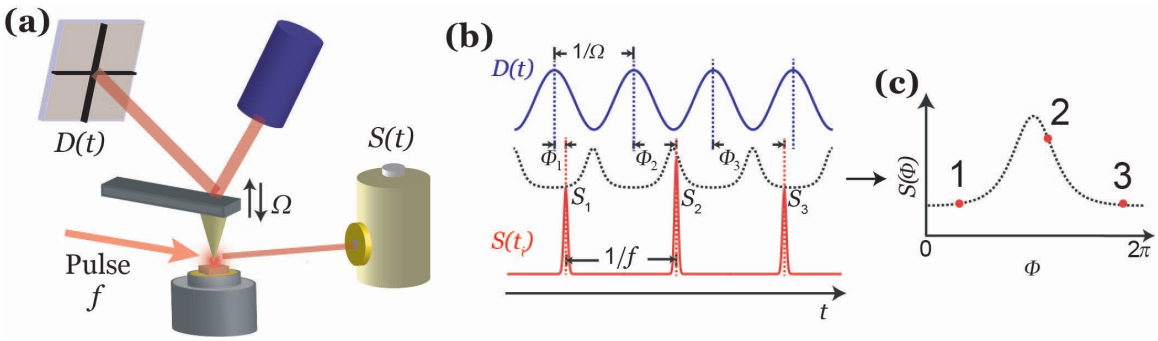

Figure 5. 2 Principle of detecting near-field signals with a low-repetition-rate source.(a) A simplified s-SNOM setup. The cantilever is driven at its mechanical frequency Ω, and its deflection $D(t)$ is recorded by a quadrant light detector. Pulsed scattering generated by incident pulses at the repetition rate of f is detected by a far-field light detector. (b) Simultaneously obtained $D(t)$ and scattering signal $S(t_i)$ ($i = 1,2,3, \ldots$) in the time domain. The actual CW near-field signal is drawn as the dashed curve. Light scattering from three pulses are detected in terms of intensity (S_1, S_2, S_3) and phase (ϕ_1,ϕ_2,ϕ_3). Then, three detected $S(\phi)$ are plotted in a graph in (c) to populate the near-field signal within the full phase range from 0 to 2π.

It is possible to detect the repeating waveform unit using a low-repetition-rate. Figure 5.2 presents the method of measuring this repeating waveform unit with a pulsed light source.[193] The AFM cantilever is oscillating at its mechanical frequency of Ω Hz, with a waveform equation in the time domain for the deflection $D(t)$:

$$D(t) = A_0 \sin(2\pi\Omega t + \phi_0) \qquad \textbf{(5.1)}$$

in which A_0 is the half amplitude of tapping and ϕ_0 is the tapping phase. $D(t)$ is a known waveform from the AFM tapping mode. The real-time phase factor ϕ inside the sine term is then:

$$\phi(t) = 2\pi\Omega t + \phi_0 = \sin^{-1}\frac{D(t)}{A_0} \qquad \textbf{(5.2)}$$

To squeeze all $\phi(t)$ that is larger than 2π into a single phase period within $[0, 2\pi]$, Equation 5.2 is recast as:

$$\phi(t) = \begin{cases} \frac{\pi}{2} + \sin^{-1}\frac{D(t)}{A_0}, & if\ \frac{dD(t)}{dt} \geq 0 \\ \frac{3\pi}{2} - \sin^{-1}\frac{D(t)}{A_0}, & if\ \frac{dD(t)}{dt} < 0 \end{cases} \quad \textbf{(5.3)}$$

The sign of the slope $dD(t)/dt$ is used to determine whether the phase $\Phi(t)$ is within the branches of $[3\pi/2\,, 2\pi]$ and $[0\,, \pi/2]$, or the branch of $[\pi/2\,, 3\pi/2]$, supposing a maximum near-field signal should appear at $\phi(t) = \pi$, and $\phi(0) = \phi_0 = \pi/2$. Equation 5.3 provides a way to calculate the real-time phase from experimentally observed cantilever deflection $D(t)$.

Depending on the moment when the pulse hits the tip, the light is scattered according to the real-time polarizability, which is dependent on the tip-sample distance (Equation 2.2), or equivalently, the instantaneous oscillation phase of the tip. Consequently, the pulsed scattering signal S has a dependence on the instantaneous oscillation phase ϕ of the cantilever motion $D(t)$. The scattering signal $S(t_i)$ measured at the time interval of $1/f$ is then correlated with the phase ϕ_i for a series of pulses from the light source. Once sufficiently large numbers of $(i \to \infty)$ the pulses are measured, many discrete $S(\phi_i)$ can compose a populated $S(\phi)$. As a result, discrete measurements in the time domain are converted into a pseudo-continuous signal in the phase domain. We call this method the phase domain sampling. This approach is conceptually similar to the procedure of sorting spectra with tip-sample distances that was used in the comb-FTIR s-SNOM.[194]

For $S(\phi)$ to accurately represent the CW near-field signal in the phase domain, ϕ_i should densely span the phase range $[0, 2\pi]$ with small intervals. This condition is achieved if the repetition rate f of the light source and the tip oscillation frequency Ω lack a common divisor, or their greatest common divisor is small. To illustrate this requirement, let us consider a train of laser pulses from the light source of a repetition rate of f Hz. The phase

difference $\Delta\phi$ between instantaneous phases of two consecutive pulses is spanned as $\Delta\phi = (2\pi\,\Omega/f \bmod 2\pi)$, with mod being the modulo operation, which provides the remainder of $2\pi\,\Omega/f$ when divided by 2π. For a pulse train consisting of n pulses, the $\Delta\phi$ domain is $\{(2\pi\,m\Omega/f + \phi_0) \bmod 2\pi\}$, with the integer m spans from 0 to $n-1$. If a common divisor q exists for f and Ω, the $\Delta\phi$ domain should consist of discrete values of $\{(2\pi\,lq/f + \phi_0) \bmod 2\pi\}$, where the integer l is from 0 to f/q. The larger the common divisor q is, the fewer l values are in the $\Delta\phi$ domain, which means there are less available non-repetitive phase values. For example, if the tip oscillation frequency is 248 kHz and the laser repetition rate is 10 kHz, the largest common divisor $q = 2$. If the initial phase Φ_0 is assumed to be $\pi/2$, the detectable phase domain would consist of $\{0.5\pi, 0.9\pi, 1.3\pi, 1.7\pi, 0.1\pi\}$. If the tip oscillation is at 249 kHz, then the phase domain consists of $\{0.5\pi, 0.7\pi, 0.9\pi, 1.1\pi, 1.3\pi, 1.5\pi, 1.7\pi, 1.9\pi, 0.1\pi, 0.3\pi\}$, which is twice as dense. In practice, unless specifically engineered, the possibility of the tip oscillation frequency Ω and laser repetition rate f to have a large common divisor is quite low. If a large common divisor exists, one can avoid it by driving the tip at a small detune within its mechanical resonance, to achieve a densely populated phase domain for ϕ between 0 and 2π.

The next step is to quantitatively extract near-field responses from $S(\phi)$. $S(\phi)$ contains every information that is needed to obtain near-field signals. For example, we can fit $S(\phi)$ within the phase domain with the form of $S(\phi) = \sum A_n \sin(n\phi + \phi_n)$ to obtain the amplitude A_n and the phase ϕ_n, for $n \geq 2$. The amplitude coefficient A_n is equivalent to values obtained from lock-in demodulation. Alternatively, we can repeat $S(\phi)$ many times between $-\infty$ and ∞, and perform Fourier analysis on the repeating waveform to obtain the non-fundamental harmonic components. A series of harmonics at the multiple of $1/2\pi$ frequencies with both amplitude A_n and phase ϕ_n can be extracted from $S(\phi)$. One of the

non-fundamental harmonic components can be used to represent the near-field response, analogous to the standard s-SNOM using lock-in detection.

5.1.3 Validation of phase domain sampling

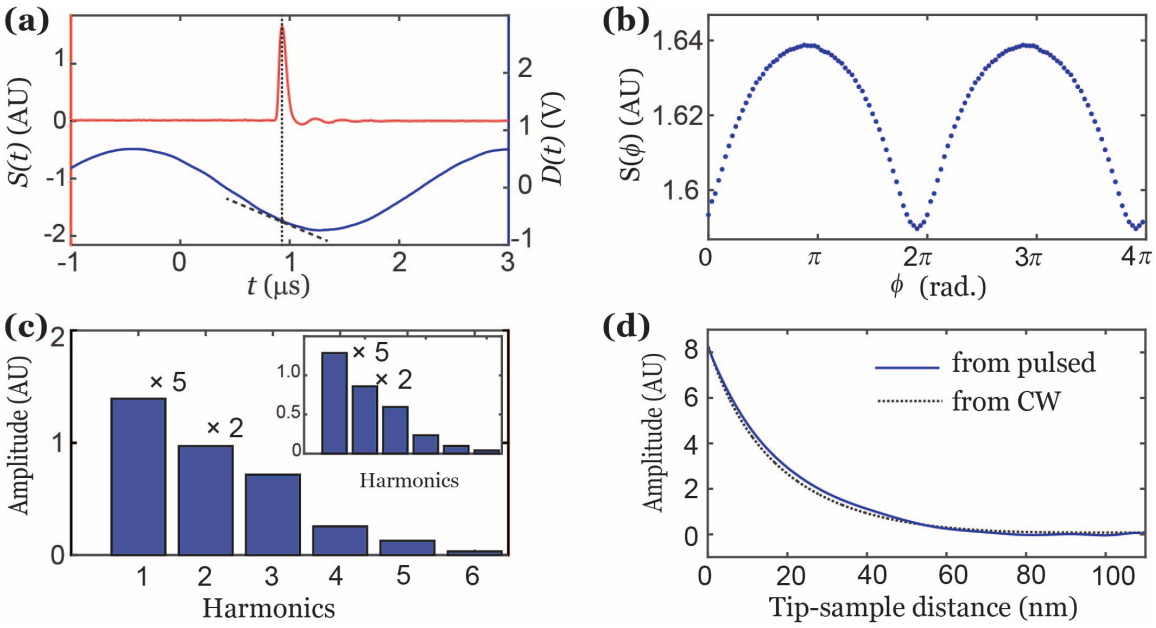

Figure 5. 3 Experimental validation of phase domain sampling.(a) Simultaneously collected $S(t)$ and $D(t)$ in the time domain. (b) Populated $S(\phi)$ by correlating the peak intensities with the calculated phases of 1×10^5 pulses. For a better illustration, two periods of $S(\phi)$ are shown. (c) Amplitudes of the harmonics by Fourier transforming the long waveform constructed by repeating the waveform in (b). The inset shows the same Fourier analysis from the lock-in demodulation using a CW laser. (d) Comparison of the vertical near-field curves obtained from 1×10^5 pulses and CW illumination.

We first demonstrate the phase domain sampling method on a strong reflecting gold substrate. The results are shown in Figure 5.3. Figure 5.3(b) shows the obtained phase-signal $S(\phi)$ binned in 64 phase values between 0 and 2π, converted from measurement events of 2×10^5 pulses with 5 nJ per-pulse energy from a quantum cascade laser (QCL), working in the pulsed mode of 10 kHz repetition rate. The nonlinear distance dependence of the tip-sample near-field interaction causes the curvature to deviate from the sinusoidal

shape. Fourier analysis on $S(\phi)$ with the procedure described above is shown in Figure 5.3(c). A series of non-fundamental harmonic components are obtained, which are characteristic of the near-field interaction. Lock-in demodulations from the CW measurement are shown as the inset for comparison. In addition, the amplitude and phase of the series of harmonics from the Fourier analysis can also be utilized to obtain the distance dependence of the tip-sample near-field interaction with a reconstruction algorithm described in Section 3.2. The results are shown in Figure 5.3(d). The $1/e$ decay range of the gold nearfield is found to be 19.3 nm, which is consistent with the reconstructed interaction curve obtained from 18 harmonics using the CW mode of QCL. In the CW measurement, the input laser energy within the lock-in time constant is around 13.1 mJ. In comparison, the total photon energy of 2×10^5 pulses with 20-ns duration is around 1 mJ, which is one order of magnitude smaller than that from the CW. Even with the smaller light energy, the signal to noise ratio obtained by the phase domain sampling is comparable to that obtained by the lock-in demodulation.

The phase domain sampling method has been tested effective for a series of low repetition rates of 1, 10, 100, and 400 kHz.[193] On the other hand, the principle of phase domain sampling does not require the repetition rate of pulses to be constant. In other words, pulses with a random or irregular repetition rate are also compatible with the phase domain sampling. Figure 5.4 performs a similar experiment to Figure 5.3 by using irregular laser pulses. In this case, the QCL laser is triggered by a noise waveform generated from a function generator. Again, a phase-domain near-field signal $S(\phi)$ can be constructed and converted to the near-field signal. The ability to work with irregular pulses ensures a stable signal acquisition for s-SNOM even when the light source has some jittering.

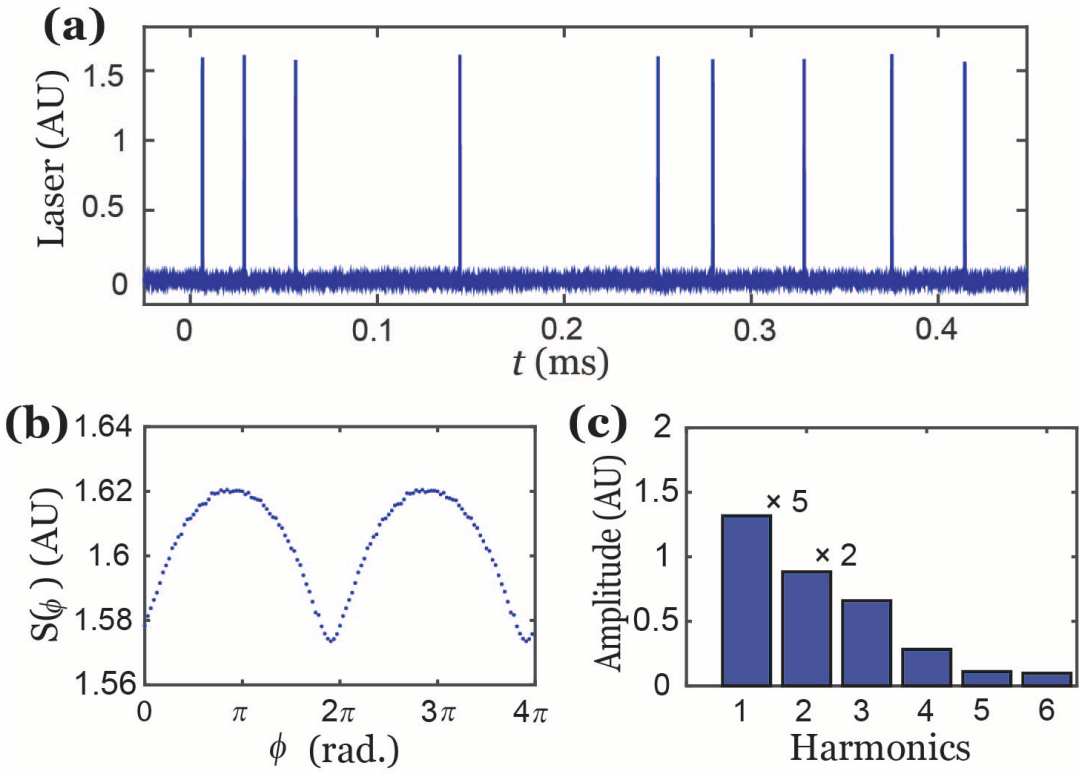

Figure 5. 4 Phase domain sampling with irregular-repetition-rate pulses.(a) Incident laser pulses with an irregular repetition rate. (b) Reconstructed $S(\phi)$ from 2×10^4 pulses. (c) Fourier analysis of reconstructed $S(\phi)$.

5.1.4 Applying low-repetition-rate pulses to measure polaritonic materials

We also carry out the s-SNOM measurement of more relevant materials of boron nitride nanotube (BNNT) and graphene nanoribbon with low-repetition-rate pulses. Figure 5.5 displays the results. Point measurements from 2×10^5 pulses with a rate of 10 kHz are compared side to side with near-field images obtained from the CW source. Moreover, a good overlap between two types of signals indicates that the phase domain sampling with low-repetition-rate light sources is also capable of near-field imaging. The high spatial resolution of s-SNOM is still preserved with scarcely distributed pulses.

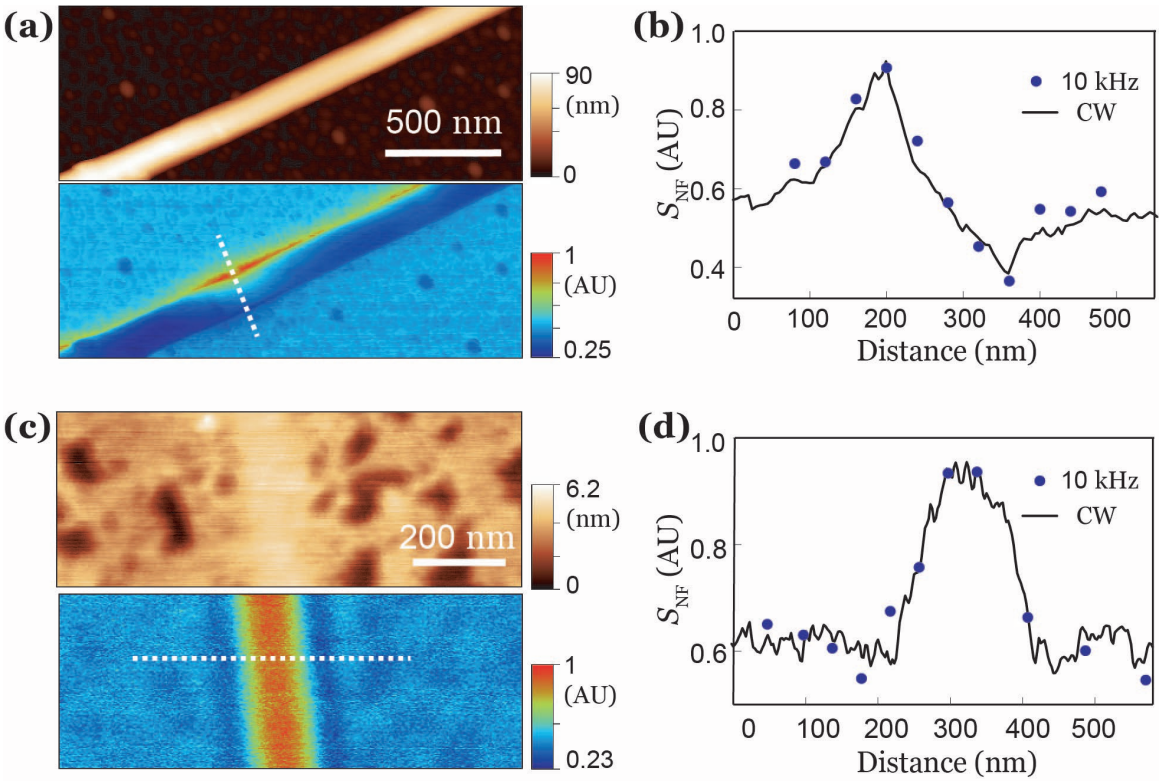

Figure 5. 5 Measuring polaritonic materials with low-repetition-rate pulses.(a) AFM topography and near-field image of a boron nitride nanotube at 1405 cm^{-1}. Phonon polaritons are resolved. The near-field image is obtained with a CW source. (b) A cross-section of the near-field image in (a) overlaid with point measurements with 10 kHz pulsed laser. (c) AFM topography and near-field image of a folded graphene multilayer (nanoribbon) at 1590 cm^{-1}. Strong near-field signals from graphene plasmons are resolved. (d) A cross-section of the near-field image in (c) overlaid with point measurements with 10 kHz pulses laser.

5.1.5 Summary

The phase domain sampling utilizes the mismatch between the cantilever's mechanical frequency and the repetition rate of the laser to convert scarcely distributed data points in the time domain into populated $S(\phi)$ in the phase domain. In a sense, Nyquist-Shannon theorem in the time domain is bypassed in this process. This claim is weak, however, since one can argue that a large number of pulses need to be measured to construct an effective $S(\phi)$, and Nyquist-Shannon sampling theorem still holds in the phase domain at the

expense of longer signal acquisition time. In practice, one of the problems that the phase domain sampling has is the long data acquisition time. For example, at a repetition rate of 10 kHz, if 2×10^4 pulses are needed to reconstruct a populated $S(\phi)$, the acquisition time per-pixel would be 2 seconds, which is fast enough for a line scan across a feature of interest, but very slow for generating a full-frame near-field image (e.g., a 128×128 pixel-size image would take 9.1 hours). This limitation can be alleviated with an increased repetition rate. At 100 kHz repetition rate, the sampling would be ten times faster, given that the hardware-level data acquisition and processing speed can keep up with the increased sampling rates.

Another drawback of the phase domain sampling is that it is susceptible to pulse-to-pulse instabilities. Since the near-field interaction is small compared with the far-field background, the pulse-to-pulse energy fluctuation is likely to be the dominant source of the noise. For example, measured pulse-to-pulse energy variations are roughly 1-3% for the QCL laser used in this experiment.[193] In Figure 5.3, for comparison, the amplitude of the second harmonic demodulation from the near-field signal on gold claims only 0.8% of the total scattering amplitude. In the presence of large pulse-to-pulse energy fluctuations, more pulses are inevitably required for averaging to obtain $S(\phi)$ for signal extraction, thus increasing the data acquisition time. On the other hand, the pulse-to-pulse fluctuations can be compensated by a far-field light detector that resolves the pulse energy for individual pulses.

In summary, the phase domain sampling method enables s-SNOM with low-repetition-rate pulsed light sources. Experimental results show near-field signals obtained from the pulsed source is equivalent to the traditional lock-in detection with the CW light source. The method expands the availability of light sources for s-SNOM and potentially permits the utilization of coherent radiation derived from the pulsed laser from popular amplified

ultrafast laser systems. With advanced low-repetition-rate light sources, it is easier to perform nanoscale spectroscopic investigations that require high instantaneous optical powers in the field of nonlinear nano-optics and pump-probe s-SNOM.

5.2 A stable homodyne device for s-SNOM

To fully map both amplitude and phase of optical nearfields, a Michelson interferometer is used in s-SNOM to enable interferometric detections, as shown in the setup Figure 2.4. However, the far-field Michelson interferometer is susceptible to external noises, such as thermal vibration and drift, because of the existence of mechanical instability. These noises can be destructive in s-SNOM, since the near-field signal is generally only a small portion of the total scattering. Moreover, it takes many efforts to align the signal beam to be colinear with the reference beam, because two beams take different paths at the incidence on a beam splitter.

The problem of mechanical instability can be alleviated by reducing the spatial length of the reference beam. Ideally, the signal beam and reference beam should be separated at a spatial location as close as possible to the sample. Therefore, the parabolic mirror used in the conventional s-SNOM to focus the light onto the tip-sample region can be engineered to also act as a beam splitter, since it provides the shortest light path in practice for the reference beam. Specifically, a small hole can be drilled through the parabolic mirror to allow a passage for the reference beam. Since the numeric aperture is large for parabolic mirrors, the energy lost in the small hole is still affordable if one uses an input beam with a large diameter. By putting a movable retroreflector on the path of the reference beam, the phase condition for the interferometric detection can be adjusted.

The s-SNOM experiment setup with a customized phase adjustable homodyne device is shown in Figure 5.6. In Figure 5.6(a), the reference arm of the traditional far-field

Michelson interferometer is replaced by a customized parabolic mirror, which not only focuses the beam onto the tip-sample region, but also permits a portion of the input beam to pass through. In Figure 5.6b, a small reflective mirror was mounted on a piezo actuator at the back of the parabolic mirror. By modifying the position of the piezo actuator, the phase of the reflected reference beam can be adjusted to achieve a homodyne detection. The actual apparatus is shown in Figure 5.6(c). To justify that the energy loss from the drilled parabolic mirror is negligible, numerical simulations of the focusing plane and the focus spot are carried out in Figure 5.6 (d-f). As a result, the focus spot preserves the desired Gaussian profile and keeps most of the energy, with a negligible phase distortion inside the beam profile.

The optical path of the retroreflected beam is adjusted by applying various voltages to the piezoelectric actuator. In our implementation, we operate the AFM in the interleave mode, in which the AFM tip scans the same line twice. The first scan is normal. In the second scan, a controllable output voltage is applied to the piezo actuator to produce a $\pi/2$ homodyne phase difference. In order to compare s-SNOM performance between the conventional reference arm and the customized homodyne device, the same voltage is applied to both piezoelectric actuators (same model), one is mounted on the back of the parabolic mirror and the other is mounted on the conventional reference arm. s-SNOM results for each case are obtained by blocking the other reference path, and dual-phase s-SNOM images from two configurations are taken sequentially.

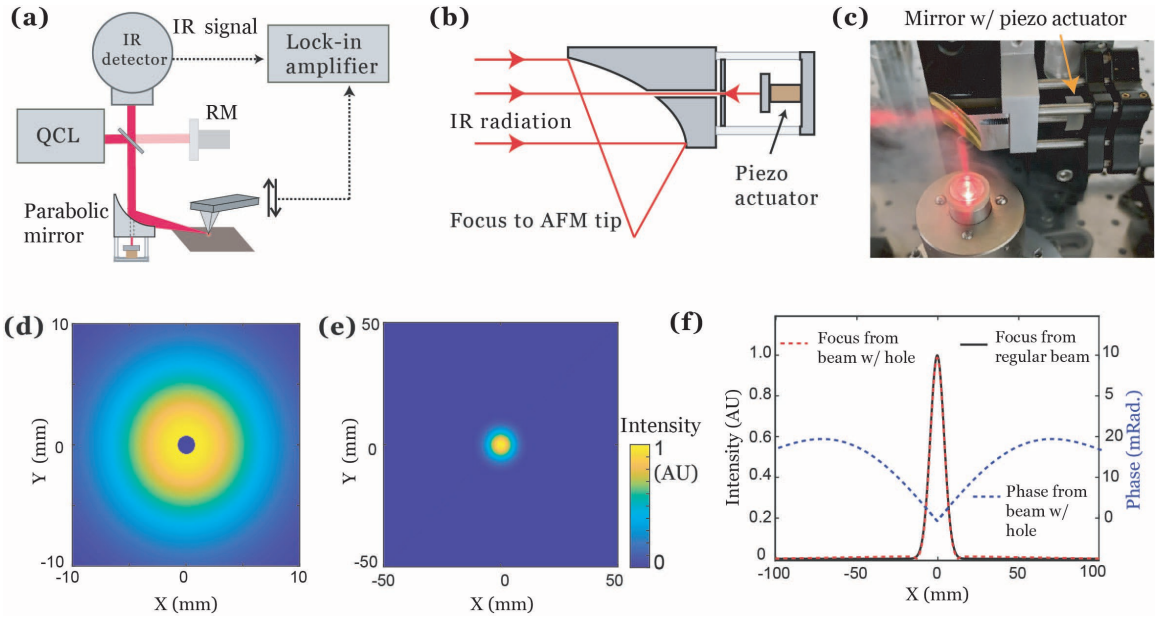

Figure 5. 6 s-SNOM with a phase adjustable homodyne device.(a) Schematic of s-SNOM with a phase adjustable self-homodyne configuration. A piezo-actuated mirror on the back of the partially transmissive parabolic mirror replaces the reference arm (RM) of the conventional Michelson interferometer. (b) Detailed illustration of the phase adjustable self-homodyne device. A retroreflector is mounted on the piezo actuator. (c) Photo of the real experimental setup. (d) Numerical simulation of a Gaussian beam incident on a parabolic mirror with a hole with a diameter of 1.5 mm. The resulting beam focus is shown in (e), assuming a 15-mm diameter of the 7-μm wavelength incident beam. (f) The profile of the focused beam along the X-axis. The intensity profile on the drilled parabolic mirror is almost the same as that from the normal focus (without hole). The phase distortion inside the beam profile is on orders of milliradian.

Two kinds of samples are measured: polaritonic boron nitride nanotubes (BNNTs) and a thin film of hexagonal boron nitride (*h*-BN). Side-by-side comparison between the customized homodyne device and the traditional reference arm is displayed in Figure 5.7. Near-field amplitude A_{NF} and phase P_{NF} images are calculated from s-SNOM results at ϕ_0 and $\phi_0 + \pi/2$ homodyne conditions according to Equation 5.4:

$$A_{\mathrm{NF}} = \sqrt{S_{\phi_0}^2 + S_{\phi_0+\pi/2}^2} \text{ and } P_{\mathrm{NF}} = \arctan(S_{\phi_0}/S_{\phi_0+\pi/2}) \quad \textbf{(5.4)}$$

in which S_{ϕ_0} and $S_{\phi_0+\pi/2}$ are s-SNOM intensities at the phase ϕ_0 and the phase $\phi_0 + \pi/2$.

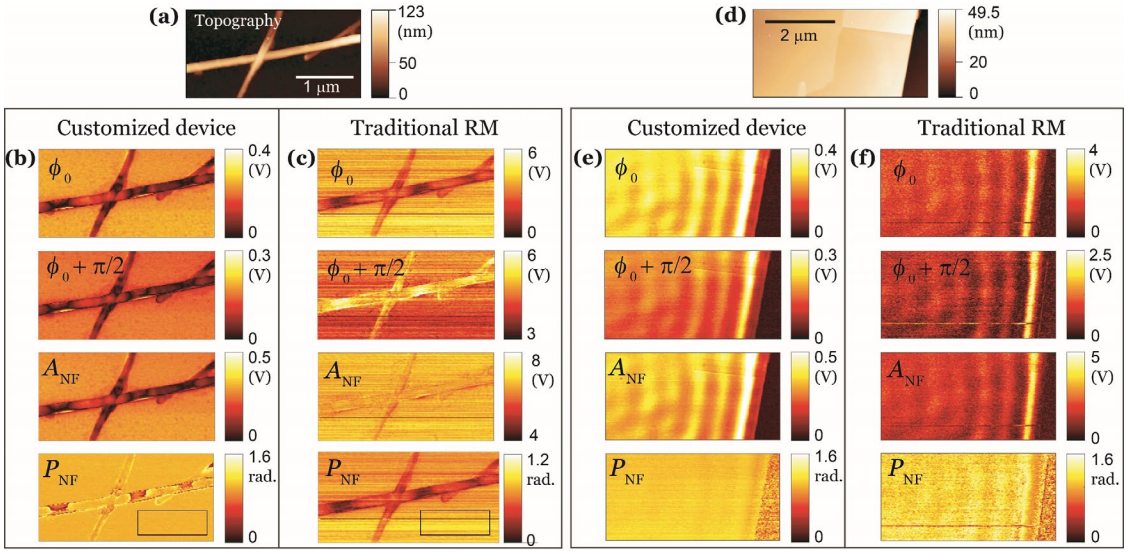

Figure 5. 7 Comparison between the customized homodyne device and the traditional reference arm.(a) Topography of BNNTs. (b-c) s-SNOM images at two phases from the 2nd harmonic demodulation, and near-field amplitude A_{NF} and phase P_{NF} images. The incident frequency is 1405 cm^{-1}. (d) Topography of a thin *h*-BN film with a thickness of 45 nm. (e-f) s-SNOM images at two phases from the 2nd harmonic demodulation, and near-field amplitude A_{NF} and phase P_{NF} images. The incident frequency is 1425 cm^{-1}. The size of each near-field image is 256×128 pixels, and the scanning time for each set of s-SNOM images is 15 min.

Compared with the traditional homodyne scheme that uses the reference arm, the customized homodyne device provides cleaner images and is less susceptible to mechanical noises and thermal drifts. Both near-field amplitude and phase signals can be resolved artifact-free in Figures 5.7(b) and (e). However, in Figure 5.7(c) and (f), imaging artifacts such as streaks are observed in near-field images obtained from the traditional reference arm. These artifacts are from the instability of the reference arm, as it has a longer optical path length, mechanical disturbances on the widely separated reference

arms during the experiment lead to significant disturbances and noisy images. The signal to noise ratio can be estimated from a rectangular area on the phase image as indicated in Figure 5.7(b-c), which is estimated to be 68 and 7 for the customized stable homodyne device and the traditional reference arm, respectively.

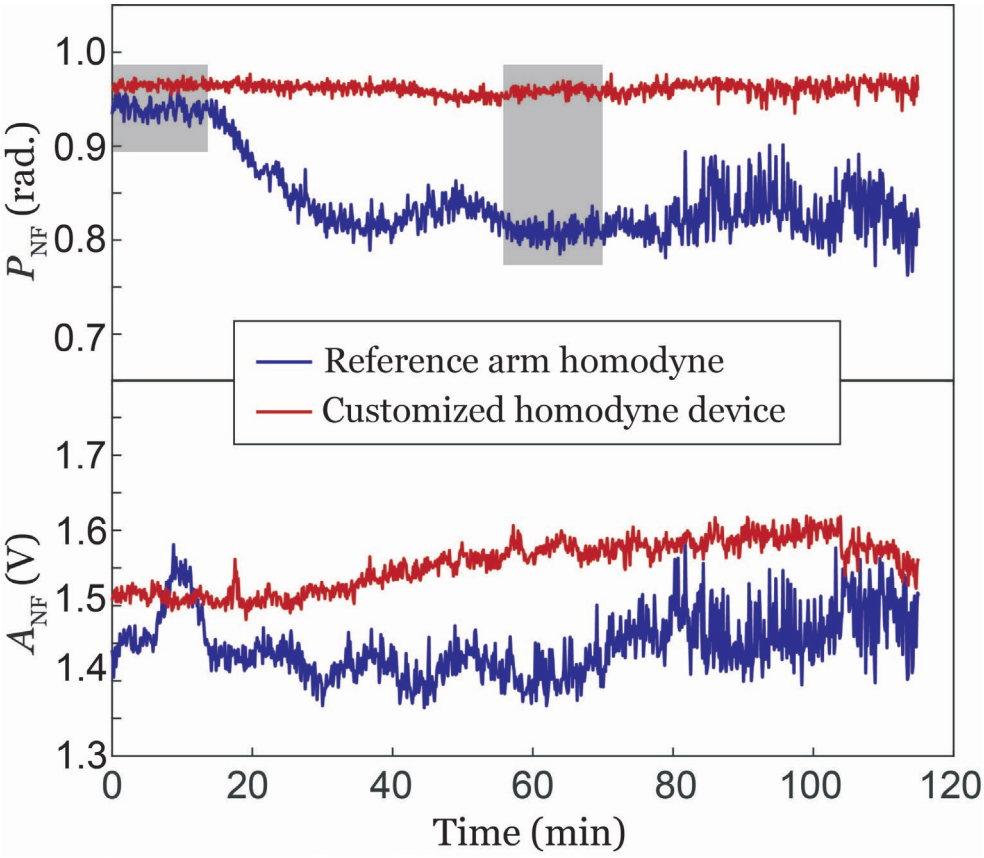

Figure 5. 8 Long-term stabilities of the customized homodyne device and traditional reference arm. Near-field amplitude and phase are obtained from the gold substrate with a mid-infrared incident frequency of 1600 cm^{-1}.

The long-term stability of each case is also estimated and compared in Figure 5.8. In this experiment, a 2-hour long s-SNOM dual-phase measurement on a smooth gold surface (with a surface roughness of 0.5 nm in a 500 × 500 nm^2 region) is performed for both the customized stable homodyne device and the conventional reference arm sequentially. The s-SNOM tip is parked on one fixed location, and 1024 × 1024 pixel size images of the s-

SNOM second demodulated amplitude are captured at $\phi_0 + \pi/2$ homodyne conditions over 115 min. Although two cases both show the drift of the near-field amplitude, it is observed that the customized homodyne device is more stable than the traditional reference arm. In the latter case, the near-field phase gradually drops within the first 30 minutes and jitters in the last 30 min. The peak-to-peak variation over 115 min is 0.2 radians. In comparison, the near-field phase obtained by the customized homodyne device remains stable over a long time with a much smaller peak-to-peak vibration of only 0.04 radian, with a large signal to noise ratio (SNR) of 149. For the reference arm, we pick two relatively smooth region (marked by two shaded areas in Figure 5.8, each is 15 min wide) to calculate SNRs, they are 32 and 67, respectively, which are consistently lower. These results demonstrate that the customized homodyne device shows better stability than the traditional reference arm, which is more susceptible to thermal drift/mechanical instability.

The advantage of the customized homodyne device based on a drilled parabolic mirror over the conventional reference arm is that the optical path of the interferometer is drastically reduced from tens of cm to several cm. The reduced optical path of the interferometer significantly reduces the instability of the optical phase in s-SNOM caused by thermal drift and vibrations. The compactness of the customized device also brings flexibility to the design of the s-SNOM instrument. For example, in low-temperature s-SNOM, the interferometer arrangement is dictated by other requirements such as temperature control and vacuum isolation. In that case, the external reference arm in the traditional Michelson configuration must be positioned outside the vacuum chamber, and thus a short and stable optical path length becomes nearly impossible. In comparison, the use of the customized homodyne device can enable putting the interferometer inside the vacuum chamber together with the parabolic mirror. This advantage may allow simple

conversion of a low-temperature stage-scanning AFM into a low-temperature s-SNOM instrument without a special design of the vacuum chamber.

As another advantage, the number of photons that are detected from the tip-sample near-field scattering process can also be enhanced by utilizing the customized homodyne device. In the conventional far-field reference arm configuration, a 50:50 R/T ratio beam splitter is typically used. Near-field scattered light from the tip-sample region after collimation must go through the same beam splitter before reaching the optical detector. Inevitably, the near-field scattered light loses 50% of the meaningful photons. On the other hand, in order to avoid sample damage from the laser exposure, the power of the incident light from the QCL often is attenuated in s-SNOM such that the incoming photon fluence at the tip-sample region is below the damaging threshold. In the customized homodyne design, the beam splitter (drilled parabolic mirror) can be engineered to give a 10:90 R/T ratio. In this case, the incident light can be attenuated to 10%, and 90% of the meaningful near-field scattered light will reach the optical detector. Given the same photon fluence at the tip-sample region, the customized homodyne device with a 10:90 R/T ratio will provide 80% more detectable signals to the detector.

Last but not least, rather than using two quadrature phases for homodyne detection, the sinusoidal phase modulation of the reference mirror behind the parabolic mirror can be used, according to the double demodulation technique of pseudo heterodyne.[80]

5.3 Peak force visible microscopy

A wide range of practical light-matter interactions is in the visible range, such as surface plasmon resonance of metallic nanoparticles,[195] fluorescence microscopy,[196] and photovoltaic technologies.[197] Investigating such processes at the nanoscale will bring new insights that are needed to unravel complex light-matter interactions at the fundamental level. To achieve nanoscale spatial resolution, a series of seminal works have been done

in the field of super-resolution fluorescence microscopy, including stimulated emission depletion (STED) microscopy,[198] saturated structured illumination microscopy (SSIM),[199] stochastic optical reconstruction microscopy (STORM),[200] photoactivated localization microscopy (PALM),[201] and fluorescence photoactivation localization microscopy (FPALM).[202] In STED, the optical focus spot is spatially modified with a donut shape to sharpen the point spread function (PSD) of individual emitters (fluorophores). In SSIM, a diffractive grating and a rotational scheme are used to reconstruct super-resolution images from saturated intensity maps of fluorescence. In STORM/PALM/FPALM, fluorophores are excited at different time points iteratively, allowing for the localization of single fluorophores by averaging many maps of PSDs.

However, super-resolution fluorescence methods rely on the large fluorescence cross-section of fluorophore molecules in the visible range, which is less applicable in a broader way than biological samples. A more general detection method is necessary to study materials that cannot be or should not be fluorophore-labeled. One of the promising candidates in the detection method is the photothermal effect, since it always accompanies the light-matter interactions, as introduced in Section 1.4.

Here, we use the same setup used in the peak force infrared (PFIR) microscopy to perform photothermal expansion measurements in the visible range. For simplicity, this technique is named as peak force visible (PF-vis) microscopy. The PF-vis microscopy is built up by replacing the IR laser source in PFIR setup with a 532-nm light source. The detection mechanism of PF-vis is the same as the regular PFIR (Figure 4.1).

5.3.1 Single-molecular sensitivity of PF-vis microscopy

Figure 5.9 shows PF-vis microscopy results of green fluorescence protein (GFP)-labeled virus-like particles (VLPs) in the ambient condition. AFM topography is shown in Figure 5.9(a), where the majority of VLPs have sizes of 30-80 nm and heights of 10-18 nm. Figure

5.9(b) displays the PF-vis image in the same region under 532-nm illumination. Individual GFP-labeled VLP particles, no matter the size, show photothermal expansion signals caused by light absorptions. On the other hand, Figure 5.9(b) suggests that the distribution of GFP on VLPs is not homogeneous.

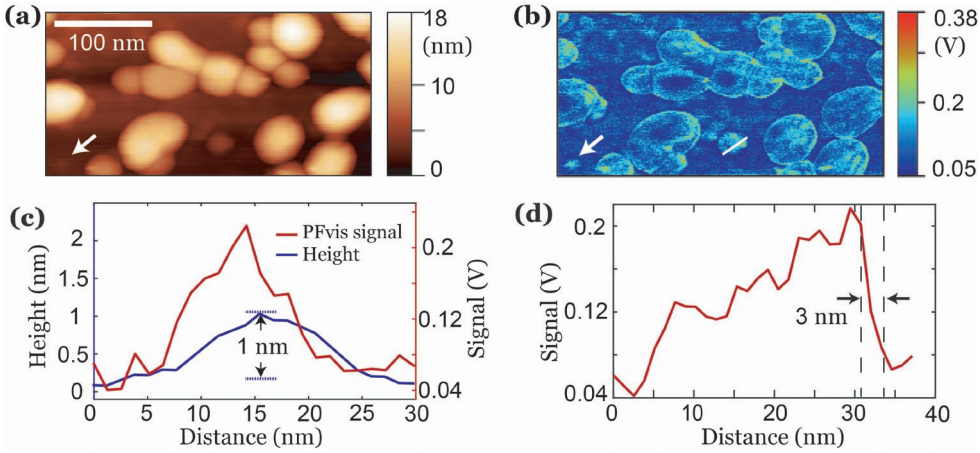

Figure 5. 9 PF-vis microscopy measurement on GFL-labeled VLPs.(a) Topography of GFP-labeled VLPs in the air. (b) PF-vis image at 532 nm. (c) Signal profiles across the small particle indicated by white arrows in (a) and (b). (d) Signal profiles across the VLP particle labeled by a white line in (b). A spatial resolution of 3 nm is obtained from the lateral distance between the 90%-10% signal maximum across the edge.

Interestingly, a small particle absorbing at 532 nm is observed in Figure 5.9(b), and the position is indicated by arrows in Figure 5.9(a-b). The signal profile across this particle is plotted in 5.9(c) along with the AFM height. A small height of 1 nm from the mica substrate indicates this particle could be a single adsorbed GFP molecule, which has a cylindrical shape of about 2.5 nm in diameter and 4 nm tall in free space.[203] The AFM width is measured to be roughly 20 nm for the particle since the lateral resolution of AFM is bound by the tip radius (~30 nm in this case). The PF-vis profile has a width of approximately 15 nm, which is ~17 times better than the diffraction limit.

To estimate the spatial resolution, the signal profile across a VLP is shown in Figure 5.7(d), and a spatial resolution of 3 nm is obtained from the width between 90%-10% of the maximal signal across the edge. The 3-nm spatial resolution exceeds 6-10 nm of the standard PFIR with an infrared laser source. Such a high spatial resolution and single-molecular sensitivity make PF-vis microscopy suitable for measuring fluorophores. Another advantage of the PF-vis microscopy is that it is not susceptible to fluorescence bleaching as a photothermal method.

5.3.2 PF-vis microscopy on organic photovoltaic samples

PF-vis microscopy is also applied to study polymer heterojunctions that are widely used in organic photovoltaics (OPVs). The key functional layer in OPV devices consists of spatially phase-separated donor and acceptor domains in a blend mixture. Excitons generated by photons diffuse towards donor-acceptor interfaces in the mixture and undergo charge separations to generate electric current. Phase-separated donor and acceptor domains are usually in the size of nanoscale, and the geometry of the phase separation plays an important role in effective light-current conversion. As we will see later, PF-vis microscopy provides a route to not only map nanoscale donor and acceptor domains, but also characterize the diffusion length of excitons, which is one of the key parameters in determining the photovoltaic performance of the device. Here, we use PF-vis microscopy to image and extract intrinsic exciton properties from OPV blends. In two investigated OPV blends, poly(3-hexylthiophene-2,5-diyl) (P3HT) and poly[(9,9-dioctylfluorenyl-2,7-diyl)-alt-(4,4′-(N-(4-sec-butylphenyl)diphenylamine)] (TFB) are used as donors, and [6,6]-phenyl C_{61} butyric acid methyl ester (PCBM) is used as the acceptor in both.

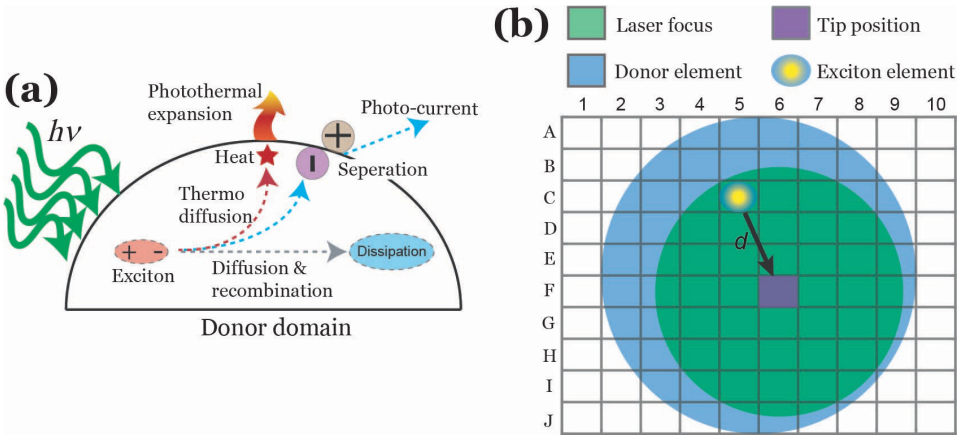

Figure 5. 10 Photothermal expansion generation in the donor domain. (a) Schematic of photothermal expansion generated by excitons. (b) Model of finite element analysis in a circular planar donor domain. Exciton generated from an element (C5) within the laser focus can travel a distance of *d* to the tip position (F6).

Figure 5.10(a) illustrates multiple routes that can be taken by excitons in the donor domain. Two major paths are used by excitons to diffuse the absorbed energy. First, excitons travel towards the interface between donor and acceptor. At the interface, the exciton dissociates into a pair of electron and hole and generates electric current by separating the electron-hole pair, this process is preferred for OPV applications. Secondly, the exciton undergoes the process of thermodiffusion to reach the dissipation state. In general, the heat generated during the second process can cause the donor domain to expand due to released thermal energy. The efficiency of both processes depends on the lifetime or the decay length of the exciton. The longer the decay length, the higher the possibility that the exciton can reach the interface, and the more the heat generation.[204] Moreover, the lifetime of excitons is in orders of ns,[204] which is much shorter than the μs-level cantilever vibrations detected in PF-vis microscopy (Figure 1c). What measured in PF-vis microscopy is then the net result of exciton distributions after the decay. Therefore, a finite element analysis can be applied to simulate exciton distributions on the donor

domain by treating every element as an exciton generation source and considering the decay length. The scheme of finite element analysis is shown in Figure 5.10(b).

In the finite element analysis shown in Figure 3b, the heat generated at each element is proportional to the local density of excitons both generated and diffused and can be written as:

$$I_{n,m} \propto \sum_{k=0}^{R} \sum_{j=0}^{R} I_{k,j} \exp(-d_{k,j}/L_{\mathrm{D}}) \qquad \textbf{(5.5)}$$

in which $I_{n,m}$ is the PF-vis signal intensity at the element (n, m), $I_{k,j}$ is the exciton density at the element (k, j), $d_{k,j}$ is the distance between the element (n, m) and (k, j), L_{D} is the exciton diffusion length, and D is the dimension of the donor domain. Note that Equation 1 is one of the simplest models for exciton decaying. It assumes a pure donor domain and does not account for the exciton reflection at the interface and heat generated elsewhere other than the exciton thermodiffusion. So, the diffusion length L_{D} in Equation 1 is apparent diffusion length. However, L_{D} is still meaningful in practice since it is directly derived from in operando PF-vis results.

In PF-vis operation, excitons are generated by the tip-enhanced light field. Thus, other factors related to the element-wise exciton generation should also be considered and added into Equation 5.5. These effects include the non-asymmetric illumination field due to the light incident direction (as shown in Figure 5.11), the limited size of the focus spot, and the actual geometry of donor domains. A modified Equation 5.5 is then written as:

$$I_{n,m} \propto \sum_{k=0}^{a} \sum_{j=0}^{b} A(k,j) I_{k,j,\mathrm{spot}} \exp(-d_{k,j}/L_{\mathrm{D}}) \qquad \textbf{(5.6)}$$

in which the donor domains are treated as ellipses, a and b are long and short axis length of the ellipse, $A(k,j)$ is the factor accounting for the asymmetry of the focus spot, and $I_{k,j,\text{spot}}$ is the exciton density at element (k,j). When (k,j) is inside the illumination spot, $I_{k,j,\text{spot}} = 1$. If (k,j) is outside the illumination spot, $I_{k,j,\text{spot}} = 0$.

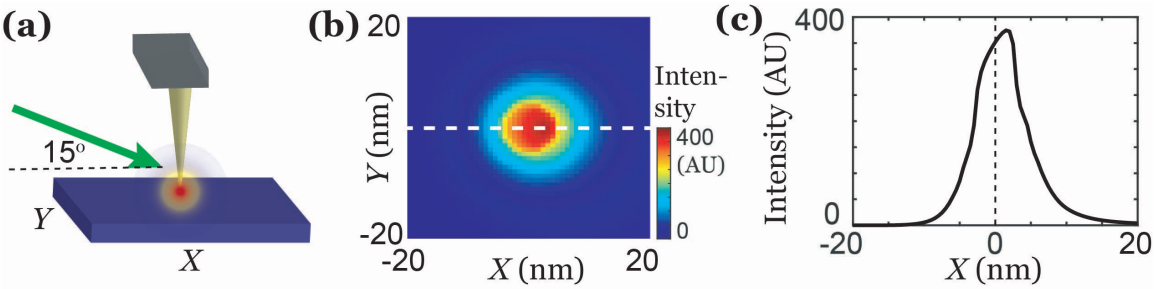

Figure 5. 11 Simulated non-symmetric focus spot. (a) Scheme used in PF-vis microscopy. A focused beam of 532-nm laser incidents from the side, at an angle of 15°. (b) FDTD simulation of the field intensity on the sample plane, when the tip-sample distance is 1 nm. The substrate is Si. (c) Line profile across the focused hot spot. The non-symmetricity is observed. The field intensity is stronger on the backside than on the front side. Such a non-symmetric shape of the focus spot is considered in the simulation in Figure 5.12.

PF-vis microscopy measurements on two kinds of OPV blend samples are shown in Figure 4. Nanoscale phase separations are observed in AFM topography images in Figure 5.12(a-b), but no further information can be extracted. In PF-vis images in Figure 5.12(c-d), two types of domains are present: one type of domain absorbs strongly at 532 nm, while the other type does not show a strong signal. In OPV blends, light energy is mostly absorbed by exciton donors. Since P3HT and TFB are used as donor molecules, and the same PCBM molecule is used as acceptor molecules in two blends, one can conclude that P3HT-rich and TFB-rich domains form higher islands in two blend films and PCBM-rich domains fill in lower interstices. This phase separation is further confirmed by modulus and adhesion images (not shown), as P3HT and TFB polymer films have lower modulus and adhesion values than PCBM. One difference between the two PF-vis images is present when

evaluating PF-vis signal distributions on donor domains in detail. For most P3HT domains, PF-vis signal distribution is roughly symmetric, with the center of domains holds higher intensity and lower intensity is observed at peripherals. In contrast, for most TFB domains, the signal distribution is asymmetric, with higher signal intensity locating towards the left side of domains. This signal distribution difference turns out to result from the asymmetric focus spot in PF-vis operation, and different domain geometries.

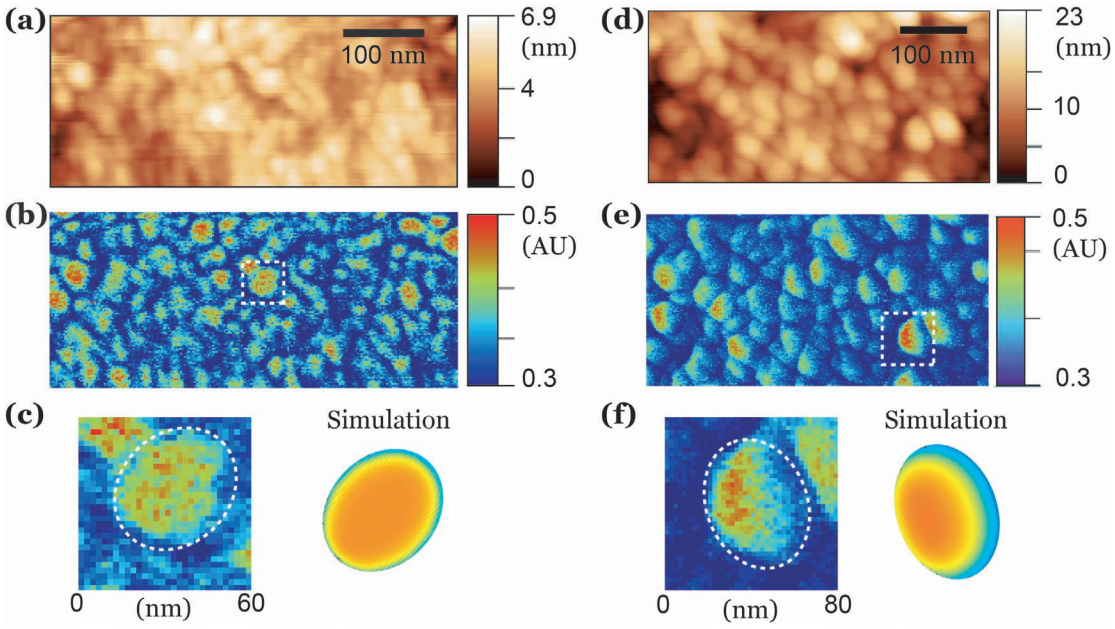

Figure 5. 12 PF-vis images of P3HT:PCBM and TFB:PCBM blend films.(a-b) Topography images of P3HT:PCBM blend film and TFB:PCBM blend film, respectively. (c-d) PF-vis images under 532-nm illumination of the same areas in (a) and (b). (e-f) Zoomed-in images of an observed P3HT-rich domain (enclosed by the white box in (c)) and a TFB-rich domain (enclosed by the white box in (d)). Simulations based on Equation 5.6 from the finite element analysis are also shown for comparisons.

Planar elliptical domain shapes are used in the simulation to account for the actual geometry. In the simulation of the P3HT-rich domain in Figure 5.12(e), an ellipse with the long axis of 60 nm and the short axis of 40 nm is used. In the simulation of the TFB-rich domain in Figure 5.12(f), an ellipse with the long axis of 80 nm and the short axis of 40

nm is used. In addition, the asymmetric factor $A(k,j)$ in Equation 5.6 is obtained by an FDTD simulation (Figure 5.11). The focus spot diameter is set as 30 nm, and diffusion lengths of 2.4 nm and 11 nm are used for P3HT and TFB-rich domains, respectively. These diffusion lengths are obtained by applying simulation fits to experimental data, as we will introduce later. As a result, a symmetric P3HT-rich domain and an asymmetric TFB-rich domain are reproduced, which accommodate the experimentally observed signal distributions. The simulations do not fully recover the experimental features because of the simplicity of the model. For example, Equation 5.6 assumes a pure donor domain. Nevertheless, in practice, the mixture of donor-acceptor pairs could exist at the molecular level.[205,206] Despite its simplicity, Equation 5.6 can still be used to extract meaningful values of the apparent exciton diffusion length L_{D} that agrees with values measured by conventional methods.

It is impractical to extract the apparent diffusion length L_{D} from the single-domain simulation, because experimentally obtained PF-vis images for single donor domains are subject to noises and insufficient spatial resolution. Therefore, we extract the L_{D} from statistical data in large-area images. Figure 5.13 shows plots of maximum signal intensity I_{max} of each donor domain as a function of effective domain radius r, overlapped with simulation results. By applying proper values of L_{D}, we observe that the best fit (within 1% of the maximum R-square) occurs with $L_{\mathrm{D}} = 2.0\sim2.8$ nm for P3HT domains and $L_D = 8\sim22$ nm for TFB domains. These results are in agreement with the diffusion lengths of 3 nm for P3HT and 9 nm for TFB measured by the conventional fluorescence quenching and transient absorption methods.[207,208]

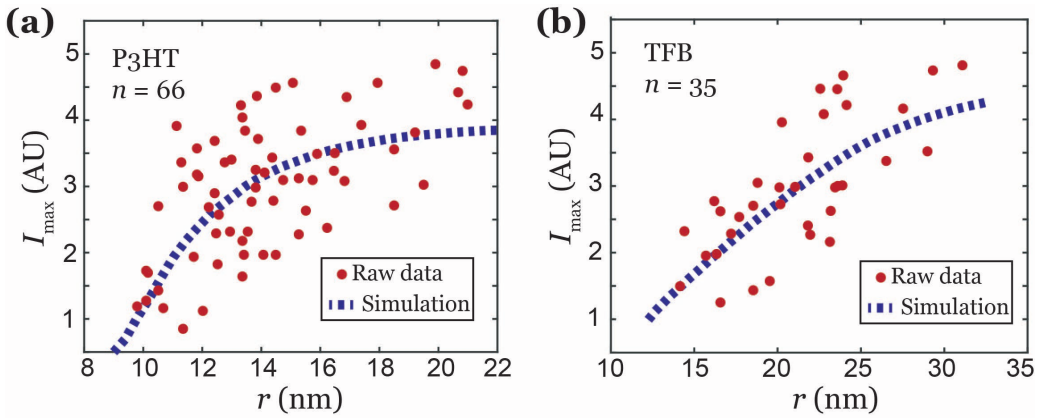

Figure 5. 13 Extraction of the apparent diffusion length. (a) The maximal signal intensity I_{max} of 66 donor domains from Figure 4c is plotted against the effective radius of each domain. The raw data are fitted with the simulation based on Equation 2 without the $A(k,j)$ term. The best fitting is obtained with L_D = 2.4 nm with an R-square value of 0.35. (b) The maximal signal intensity I_{max} of 35 donor domains from Figure 4d is plotted against the effective radius of each domain. The best fitting is obtained with L_D = 11 nm with an R-square value of 0.51.

Compared with other methods that are commonly used in determining the diffusion length L_D such as the photoluminescence quenching[208,209] and transient absorption spectroscopy,[207] PF-vis spectroscopy can directly measure the apparent diffusion length and requires fewer specialties in the sample preparation and less expensive laser sources. It does not need to work with thin films or crystals, but rather focus on in situ and in operando properties of photo-active donor-acceptor blends, thus providing more useful results for practical applications. Upon the completion of a single PF-vis microscopy scan, donor and acceptor domains can be distinguished and the apparent exciton diffusion length L_D can be estimated at the same time.

Further improvement on the accuracy of the measured apparent diffusion length L_D can be achieved by considering local morphology variations of the donor domains and applying a 3D finite element analysis. In the finite element analysis, the eclipse approximation used in our current model could be further modified domain by domain to

account for the actual geometry of each donor domain. An exciton reflection model can be further added into Equation 5.6 to better characterize signal intensity at domain peripherals. Besides, the feasibility of finite element analysis also allows for taking the exciton behaviors at domain interfaces into consideration and performing iterative calculations to reach a steady state at the expense of computational complexity.

REFERENCES

1. Novotny, L. & Hecht, B. *Principles of Nano-Optics*. (Cambridge University Press, 2006).
2. Powell, C. J. & Swan, J. B. Origin of the characteristic electron energy losses in aluminum. *Physical Review* **115**, 869, doi:10.1103/physrev.115.869 (1959).
3. Powell, C. J. & Swan, J. B. Origin of the characteristic electron energy losses in magnesium. *Physical Review* **116**, 81, doi:10.1103/physrev.116.81 (1959).
4. Yu, H., Peng, Y., Yang, Y. & Li, Z.-Y. Plasmon-enhanced light–matter interactions and applications. *npj Computational Materials* **5**, 1-14, doi:10.1038/s41524-019-0184-1 (2019).
5. Knobloch, H., Brunner, H., Leitner, A., Aussenegg, F. & Knoll, W. Probing the evanescent feld of propagating plasmon surface-polaritons by fluorescence and Raman spectroscopies. *Journal of Chemical Physics* **98**, 10093-10095, doi:10.1063/1.464398 (1993).
6. Knoll, W. Interfaces and thin films as seen by bound electromagnetic waves. *Annual Review of Physical Chemistry* **49**, 569-638, doi:10.1146/annurev.physchem.49.1.569 (1998).
7. Willets, K. A. & Van Duyne, R. P. Localized surface plasmon resonance spectroscopy and sensing. *Annual Review of Physical Chemistry* **58**, 267-297, doi:10.1146/annurev.physchem.58.032806.104607 (2007).
8. Polman, A. & Atwater, H. A. Plasmonics: optics at the nanoscale. *Materials Today* **8**, 56-56, doi:10.1016/S1369-7021(04)00685-6 (2005).
9. Okamoto, T. in *Near-field optics and surface plasmon polaritons* 97-123 (Springer, 2001).
10. Murray, W. A., Astilean, S. & Barnes, W. L. Transition from localized surface plasmon resonance to extended surface plasmon-polariton as metallic nanoparticles merge to form a periodic hole array. *Physical Review B* **69**, 165407, doi:10.1103/physrevb.69.165407 (2004).
11. Ye, Y.-H. *et al.* Localized surface plasmon polaritons in Ag/SiO2/Ag plasmonic thermal emitter. *Applied Physics Letters* **93**, 033113, doi:10.1063/1.2958215 (2008).
12. Sun, S., Chen, H. T., Zheng, W. J. & Guo, G. Y. Dispersion relation, propagation length and mode conversion of surface plasmon polaritons in silver double-nanowire systems. *Optics Express* **21**, 14591-14605, doi:10.1364/oe.21.014591 (2013).
13. Maier, S. A. *Plasmonics: Fundamentals and Applications*. (Springer Science & Business Media, 2007).
14. Mortazavi, D., Kouzani, A. Z., Kaynak, A. & Duan, W. Developing LSPR design guidelines. *Progress in Electromagnetics Research* **126**, 203-235, doi:10.2528/pier12011810 (2012).
15. Wang, X., Ruditskiy, A. & Xia, Y. N. Rational design and synthesis of noble-metal nanoframes for catalytic and photonic applications. *National Science Review* **3**, 520-533, doi:10.1093/nsr/nww062 (2016).
16. Yee, K. Numerical solution of initial boundary value problems involving Maxwell's equations in isotropic media. *IEEE Transactions on Antennas and Propagation* **14**, 302-307, doi:10.1109/tap.1966.1138693 (1966).
17. Gedney, S. *Introduction to the Finite-Difference Time-Domain (FDTD) Method for Electromagnetics*. Vol. 6 (Morgan & Claypool, 2011).
18. Abbe, E. Beiträge zur Theorie des Mikroskops und der mikroskopischen Wahrnehmung. *Archiv für mikroskopische Anatomie* **9**, 413-418 (1873).

19. Fleischmann, M., Hendra, P. J. & McQuillan, A. J. Raman spectra of pyridine adsorbed at a silver electrode. *Chemical Physics Letters* **26**, 163-166, doi:10.1016/0009-2614(74)85388-1 (1974).
20. Nie, S. & Emory, S. R. Probing single molecules and single nanoparticles by surface-enhanced Raman scattering. *Science* **275**, 1102-1106, doi:10.1126/science.275.5303.1102 (1997).
21. Singh, B. R. in *Infrared Analysis of Peptides and Proteins ACS Symposium Series* Ch. 1, 2-37 (ACS Publications, 2000).
22. Basov, D. N., Fogler, M. M. & De Abajo, F. J. G. Polaritons in van der Waals materials. *Science* **354**, aag1992, doi:10.1126/science.aag1992 (2016).
23. Binnig, G., Rohrer, H., Gerber, C. & Weibel, E. 7×7 reconstruction on Si (111) resolved in real space. *Physical Review Letters* **50**, 120, doi:10.1103/physrevlett.50.120 (1983).
24. Stöckle, R. M., Suh, Y. D., Deckert, V. & Zenobi, R. Nanoscale chemical analysis by tip-enhanced Raman spectroscopy. *Chemical Physics Letters* **318**, 131-136, doi:10.1016/S0009-2614(99)01451-7 (2000).
25. Hillenbrand, R., Taubner, T. & Keilmann, F. Phonon-enhanced light–matter interaction at the nanometre scale. *Nature* **418**, 159-162, doi:10.1038/nature00899 (2002).
26. Dazzi, A., Prazeres, R., Glotin, F. & Ortega, J. M. Local infrared microspectroscopy with subwavelength spatial resolution with an atomic force microscope tip used as a photothermal sensor. *Optics Letters* **30**, 2388-2390, doi:10.1364/ol.30.002388 (2005).
27. Nowak, D. *et al.* Nanoscale chemical imaging by photoinduced force microscopy. *Science Advances* **2**, e1501571, doi:10.1126/sciadv.1501571 (2016).
28. Wang, L. *et al.* Nanoscale simultaneous chemical and mechanical imaging via peak force infrared microscopy. *Science Advances* **3**, e1700255, doi:10.1126/sciadv.1700255 (2017).
29. Terazima, M. *et al.* Quantities, terminology, and symbols in photothermal and related spectroscopies (IUPAC Recommendations 2004). *Pure and Applied Chemistry* **76**, 1083-1118, doi:10.1351/pac200476061083 (2004).
30. Sumie, S. *et al.* A new method of photothermal displacement measurement by laser interferometric probe-its mechanism and applications to evaluation of lattice damage in semiconductors. *Japanese Journal of Applied Physics* **31**, 3575, doi:10.1143/jjap.31.3575 (1992).
31. Dazzi, A., Glotin, F. & Carminati, R. Theory of infrared nanospectroscopy by photothermal induced resonance. *Journal of Applied Physics* **107**, 124519, doi:10.1063/1.3429214 (2010).
32. Lu, F., Jin, M. & Belkin, M. A. Tip-enhanced infrared nanospectroscopy via molecular expansion force detection. *Nature Photonics* **8**, 307, doi:10.1038/nphoton.2013.373 (2014).
33. Hu, M. & Hartland, G. V. Heat dissipation for Au particles in aqueous solution: relaxation time versus size. *The Journal of Physical Chemistry B* **106**, 7029-7033, doi:10.1021/jp020581+ (2002).
34. Chen, X., Chen, Y., Yan, M. & Qiu, M. Nanosecond photothermal effects in plasmonic nanostructures. *ACS Nano* **6**, 2550-2557, doi:10.1021/nn2050032 (2012).
35. Dazzi, A. in *Thermal nanosystems and nanomaterials* 469-503 (Springer, 2009).
36. Dazzi, A., Deniset-Besseau, A. & Lasch, P. Minimising contributions from scattering in infrared spectra by means of an integrating sphere. *Analyst* **138**, 4191-4201, doi:10.1039/c3an00381g (2013).

37. Tsuda, S., Yamaguchi, S., Kanamori, Y. & Yugami, H. Spectral and angular shaping of infrared radiation in a polymer resonator with molecular vibrational modes. *Optics Express* **26**, 6899-6915, doi:10.1364/oe.26.006899 (2018).
38. Binnig, G., Rohrer, H., Gerber, C. & Weibel, E. Surface studies by scanning tunneling microscopy. *Physical Review Letters* **49**, 57, doi:10.1103/physrevlett.49.57 (1982).
39. Rugar, D. & Hansma, P. Atomic force microscopy. *Physics Today* **43**, 23-30, doi:10.1063/1.881238 (1990).
40. Giessibl, F. J. Advances in atomic force microscopy. *Reviews of Modern Physics* **75**, 949, doi:10.1103/revmodphys.75.949 (2003).
41. Schön, P. M., Gosa, M. & Vancso, G. J. Imaging of mechanical properties of soft matter. from heterogeneous polymer surfaces to single biomolecules. *Imaging & Microscopy* **15**, 43-46 (2013).
42. Cappella, B. & Dietler, G. Force-distance curves by atomic force microscopy. *Surface Science Reports* **34**, 1-104, doi:10.1016/S0167-5729(99)00003-5 (1999).
43. San Paulo, A. & García, R. High-resolution imaging of antibodies by tapping-mode atomic force microscopy: attractive and repulsive tip-sample interaction regimes. *Biophysical Journal* **78**, 1599-1605, doi:10.1016/S0006-3495(00)76712-9 (2000).
44. Kaemmer, S. B. Introduction to Bruker's ScanAsyst and PeakForce Tapping AFM Technology. *Bruker Application Note # 133* (2011).
45. Schmitz, I., Schreiner, M., Friedbacher, G. & Grasserbauer, M. Tapping-mode AFM in comparison to contact-mode AFM as a tool for in situ investigations of surface reactions with reference to glass corrosion. *Analytical Chemistry* **69**, 1012-1018, doi:10.1021/ac9607020 (1997).
46. Johnson, K. L. & Woodhouse, J. Stick–slip motion in the atomic force microscope. *Tribology Letters* **5**, 155-160, doi:10.1023/a:1019106127794 (1998).
47. Tamayo, J. & Garcia, R. Deformation, contact time, and phase contrast in tapping mode scanning force microscopy. *Langmuir* **12**, 4430-4435, doi:10.1021/la960189l (1996).
48. Magonov, S. N., Elings, V. & Whangbo, M. H. Phase imaging and stiffness in tapping-mode atomic force microscopy. *Surface Science* **375**, L385-L391, doi:10.1016/S0039-6028(96)01591-9 (1997).
49. Noy, A., Sanders, C. H., Vezenov, D. V., Wong, S. S. & Lieber, C. M. Chemically-sensitive imaging in tapping mode by chemical force microscopy: relationship between phase lag and adhesion. *Langmuir* **14**, 1508-1511, doi:10.1021/la970948f (1998).
50. Tamayo, J. & Garcı´a, R. Relationship between phase shift and energy dissipation in tapping-mode scanning force microscopy. *Applied Physics Letters* **73**, 2926-2928, doi:10.1063/1.122632 (1998).
51. Jin, M., Lu, F. & Belkin, M. A. High-sensitivity infrared vibrational nanospectroscopy in water. *Light: Science & Applications* **6**, e17096-e17096, doi:10.1038/lsa.2017.96 (2017).
52. Rosa-Zeiser, A., Weilandt, E., Hild, S. & Marti, O. The simultaneous measurement of elastic, electrostatic and adhesive properties by scanning force microscopy: pulsed-force mode operation. *Measurement Science and Technology* **8**, 1333, doi:10.1088/0957-0233/8/11/020 (1997).
53. Pittenger, B., Erina, N. & Su, C. Quantitative mechanical property mapping at the nanoscale with PeakForce QNM. *Application Note Veeco Instruments Inc*, 1-12 (2010).
54. Trtik, P., Kaufmann, J. & Volz, U. On the use of peak-force tapping atomic force microscopy for quantification of the local elastic modulus in hardened cement paste.

Cement and Concrete Research **42**, 215-221, doi:10.1016/j.cemconres.2011.08.009 (2012).
55. Li, C., Ostadhassan, M., Guo, S., Gentzis, T. & Kong, L. Application of PeakForce tapping mode of atomic force microscope to characterize nanomechanical properties of organic matter of the Bakken Shale. *Fuel* **233**, 894-910, doi:10.1016/j.fuel.2018.06.021 (2018).
56. Alsteens, D. *et al.* High-resolution imaging of chemical and biological sites on living cells using peak force tapping atomic force microscopy. *Langmuir* **28**, 16738-16744, doi:10.1021/la303891j (2012).
57. Schillers, H., Medalsy, I., Hu, S., Slade, A. L. & Shaw, J. E. PeakForce tapping resolves individual microvilli on living cells. *Journal of Molecular Recognition* **29**, 95-101, doi:10.1002/jmr.2510 (2016).
58. Lorenzoni, M. *et al.* Assessing the local nanomechanical properties of self-assembled block copolymer thin films by peak force tapping. *Langmuir* **31**, 11630-11638, doi:10.1021/acs.langmuir.5b02595 (2015).
59. Rico, F., Su, C. & Scheuring, S. Mechanical mapping of single membrane proteins at submolecular resolution. *Nano Letters* **11**, 3983-3986, doi:10.1021/nl202351t (2011).
60. Adamcik, J. *et al.* Measurement of intrinsic properties of amyloid fibrils by the peak force QNM method. *Nanoscale* **4**, 4426-4429, doi:10.1039/c2nr30768e (2012).
61. Zhao, B. *et al.* Mechanical mapping of nanobubbles by PeakForce atomic force microscopy. *Soft Matter* **9**, 8837-8843, doi:10.1039/c3sm50942g (2013).
62. Walczyk, W., Schön, P. M. & Schönherr, H. The effect of PeakForce tapping mode AFM imaging on the apparent shape of surface nanobubbles. *Journal of Physics: Condensed Matter* **25**, 184005, doi:10.1088/0953-8984/25/18/184005 (2013).
63. Richter, M. & Deckert, V. Scanning near-field optical microscopy (SNOM). *Surface and Thin Film Analysis* **152**, 481-497, doi:10.1111/j.1365-2818.1988.tb01458.x (2011).
64. Ocelic, N. *Quantitative near-field phonon-polariton spectroscopy*, Technische Universität München, (2007).
65. Keilmann, F. & Hillenbrand, R. Near-field microscopy by elastic light scattering from a tip. *Philosophical Transactions of the Royal Society of London. Series A: Mathematical, Physical and Engineering Sciences* **362**, 787-805, doi:10.1098/rsta.2003.1347 (2004).
66. Taubner, T., Hillenbrand, R. & Keilmann, F. Nanoscale polymer recognition by spectral signature in scattering infrared near-field microscopy. *Applied Physics Letters* **85**, 5064-5066, doi:10.1063/1.1827334 (2004).
67. Jones, A. C. *et al.* Mid-IR plasmonics: near-field imaging of coherent plasmon modes of silver nanowires. *Nano Letters* **9**, 2553-2558, doi:10.1021/nl900638p (2009).
68. Amarie, S. *et al.* Nano-FTIR chemical mapping of minerals in biological materials. *Beilstein Journal of Nanotechnology* **3**, 312-323, doi:10.3762/bjnano.3.35 (2012).
69. Mattis Hoffmann, J., Hauer, B. & Taubner, T. Antenna-enhanced infrared near-field nanospectroscopy of a polymer. *Applied Physics Letters* **101**, 193105, doi:10.1063/1.4766178 (2012).
70. Andryieuski, A. *et al.* Direct characterization of plasmonic slot waveguides and nanocouplers. *Nano Letters* **14**, 3925-3929, doi:10.1021/nl501207u (2014).
71. Dominguez, G. *et al.* Nanoscale infrared spectroscopy as a non-destructive probe of extraterrestrial samples. *Nature Communications* **5**, 1-10, doi:10.1038/ncomms6445 (2014).
72. Dai, S. *et al.* Tunable phonon polaritons in atomically thin van der Waals crystals of boron nitride. *Science* **343**, 1125-1129, doi:10.1126/science.1246833 (2014).

73. Fehrenbacher, M. *et al.* Plasmonic superlensing in doped GaAs. *Nano Letters* **15**, 1057-1061, doi:10.1021/nl503996q (2015).
74. Dai, S. *et al.* Graphene on hexagonal boron nitride as a tunable hyperbolic metamaterial. *Nature Nanotechnology* **10**, 682-686, doi:10.1038/nnano.2015.131 (2015).
75. Ni, G. X. *et al.* Plasmons in graphene moiré superlattices. *Nature Materials* **14**, 1217-1222, doi:10.1038/nmat4425 (2015).
76. Khatib, O. *et al.* Graphene-based platform for infrared near-field nanospectroscopy of water and biological materials in an aqueous environment. *ACS Nano* **9**, 7968-7975, doi:10.1021/acsnano.5b01184 (2015).
77. Ni, G. X. *et al.* Ultrafast optical switching of infrared plasmon polaritons in high-mobility graphene. *Nature Photonics* **10**, 244-247, doi:10.1038/nphoton.2016.45 (2016).
78. Etxeberria-Benavides, M. *et al.* High performance mixed matrix membranes (MMMs) composed of ZIF-94 filler and 6FDA-DAM polymer. *Journal of Membrane Science* **550**, 198-207, doi:10.1016/j.memsci.2017.12.033 (2018).
79. Xu, X. G., Gilburd, L. & Walker, G. C. Phase stabilized homodyne of infrared scattering type scanning near-field optical microscopy. *Applied Physics Letters* **105**, 263104, doi:10.1063/1.4905207 (2014).
80. Hillenbrand, R. & Keilmann, F. Complex optical constants on a subwavelength scale. *Physical Review Letters* **85**, 3029, doi:10.1103/physrevlett.85.3029 (2000).
81. Schnell, M., Carney, P. S. & Hillenbrand, R. Synthetic optical holography for rapid nanoimaging. *Nature Communications* **5**, 3499, doi:10.1038/ncomms4499 (2014).
82. Huth, F. *et al.* Nano-FTIR absorption spectroscopy of molecular fingerprints at 20 nm spatial resolution. *Nano Letters* **12**, 3973-3978, doi:10.1021/nl301159v (2012).
83. Knoll, B. & Keilmann, F. Enhanced dielectric contrast in scattering-type scanning near-field optical microscopy. *Optics Communications* **182**, 321-328, doi:10.1016/S0030-4018(00)00826-9 (2000).
84. Cvitkovic, A., Ocelic, N. & Hillenbrand, R. Analytical model for quantitative prediction of material contrasts in scattering-type near-field optical microscopy. *Optics Express* **15**, 8550-8565, doi:10.1364/oe.15.008550 (2007).
85. Govyadinov, A. A. *et al.* Recovery of permittivity and depth from near-field data as a step toward infrared nanotomography. *ACS Nano* **8**, 6911-6921, doi:10.1021/nn5016314 (2014).
86. Wang, H., Wang, L., Jakob, D. S. & Xu, X. G. Tomographic and multimodal scattering-type scanning near-field optical microscopy with peak force tapping mode. *Nature Communications* **9**, 1-11, doi:10.1038/s41467-018-04403-5 (2018).
87. Centrone, A. Infrared imaging and spectroscopy beyond the diffraction limit. *Annual Review of Analytical Chemistry* **8**, 101-126, doi:10.1146/annurev-anchem-071114-040435 (2015).
88. Zhang, L. M. *et al.* Near-field spectroscopy of silicon dioxide thin films. *Physical Review B* **85**, 075419, doi:10.1103/physrevb.85.075419 (2012).
89. Dazzi, A. *et al.* AFM–IR: combining atomic force microscopy and infrared spectroscopy for nanoscale chemical characterization. *Applied Spectroscopy* **66**, 1365-1384, doi:10.1366/12-06804 (2012).
90. Dazzi, A. & Prater, C. B. AFM-IR: technology and applications in nanoscale infrared spectroscopy and chemical imaging. *Chemical Reviews* **117**, 5146-5173, doi:10.1021/acs.chemrev.6b00448 (2017).

91. Marcott, C., Lo, M., Kjoller, K., Prater, C. & Gerrard, D. P. Applications of AFM-IR—diverse chemical composition analyses at nanoscale spatial resolution. *Microscopy Today* **20**, 16-21, doi:10.1017/S1551929512000776 (2012).
92. Milosevic, M. On the nature of the evanescent wave. *Applied Spectroscopy* **67**, 126-131, doi:10.1366/12-06707 (2013).
93. Mayet, C. *et al.* Sub-100 nm IR spectromicroscopy of living cells. *Optics Letters* **33**, 1611-1613, doi:10.1364/ol.33.001611 (2008).
94. Ramer, G., Ruggeri, F. S., Levin, A., Knowles, T. P. J. & Centrone, A. Determination of polypeptide conformation with nanoscale resolution in water. *ACS Nano* **12**, 6612-6619, doi:10.1021/acsnano.8b01425 (2018).
95. Katzenmeyer, A. M., Aksyuk, V. & Centrone, A. Nanoscale infrared spectroscopy: improving the spectral range of the photothermal induced resonance technique. *Analytical Chemistry* **85**, 1972-1979, doi:10.1021/ac303620y (2013).
96. Jarzembski, A., Shaskey, C. & Park, K. Tip-based vibrational spectroscopy for nanoscale analysis of emerging energy materials. *Frontiers in Energy* **12**, 43-71, doi:10.1007/s11708-018-0524-8 (2018).
97. Jahng, J. *et al.* Linear and nonlinear optical spectroscopy at the nanoscale with photoinduced force microscopy. *Accounts of Chemical Research* **48**, 2671-2679, doi:10.1021/acs.accounts.5b00327 (2015).
98. Jahng, J., Kim, B., Lee, E. S. & Potma, E. O. Quantitative analysis of sideband coupling in photoinduced force microscopy. *Physical Review B* **94**, 195407, doi:10.1103/physrevb.94.195407 (2016).
99. Yang, H. U. & Raschke, M. B. Resonant optical gradient force interaction for nano-imaging and-spectroscopy. *New Journal of Physics* **18**, 053042, doi:10.1088/1367-2630/18/5/053042 (2016).
100. Wang, L., Wang, H., Vezenov, D. & Xu, X. G. Direct measurement of photoinduced force for nanoscale infrared spectroscopy and chemical-sensitive imaging. *Journal of Physical Chemistry C* **122**, 23808-23813, doi:10.1021/acs.jpcc.8b09107 (2018).
101. Jahng, J., Potma, E. O. & Lee, E. S. Tip-enhanced thermal expansion force for nanoscale chemical imaging and spectroscopy in photoinduced force microscopy. *Analytical Chemistry* **90**, 11054-11061, doi:10.1021/acs.analchem.8b02871 (2018).
102. Tumkur, T. U. *et al.* Photoinduced force mapping of plasmonic nanostructures. *Nano Letters* **16**, 7942-7949, doi:10.1021/acs.nanolett.6b04245 (2016).
103. Fu, D. *et al.* Nanoscale infrared imaging of zeolites using photoinduced force microscopy. *Chemical Communications* **53**, 13012-13014, doi:10.1039/c7cc06832h (2017).
104. Ambrosio, A., Devlin, R. C., Capasso, F. & Wilson, W. L. J. A. P. Observation of nanoscale refractive index contrast via photoinduced force microscopy. *ACS Photonics* **4**, 846-851, doi:10.1021/acsphotonics.6b00911 (2017).
105. Murdick, R. A. *et al.* Photoinduced force microscopy: A technique for hyperspectral nanochemical mapping. *Japanese Journal of Applied Physics* **56**, 08LA04, doi:10.7567/jjap.56.08la04 (2017).
106. Gu, K. L. *et al.* Nanoscale domain imaging of all-polymer organic solar cells by photo-induced force microscopy. *ACS Nano* **12**, 1473-1481, doi:10.1021/acsnano.7b07865 (2018).
107. Liu, J. *et al.* Near-Field characterization of graphene plasmons by photo-Induced force microscopy. *Laser & Photonics Reviews* **12**, 1800040, doi:10.1002/lpor.201800040 (2018).
108. Rotenberg, N. & Kuipers, L. Mapping nanoscale light fields. *Nature Photonics* **8**, 919, doi:10.1038/nphoton.2014.285 (2014).

109. Raschke, M. B. & Lienau, C. Apertureless near-field optical microscopy: Tip–sample coupling in elastic light scattering. *Applied Physics Letters* **83**, 5089-5091, doi:10.1063/1.1632023 (2003).
110. Olmon, R. L. *et al.* Determination of electric-field, magnetic-field, and electric-current distributions of infrared optical antennas: a near-field optical vector network analyzer. *Physical Review Letters* **105**, 167403, doi:10.1103/physrevlett.105.167403 (2010).
111. Li, Y., Zhou, N., Raman, A. & Xu, X. Three-dimensional mapping of optical near field with scattering SNOM. *Optics Express* **23**, 18730-18735, doi:10.1364/oe.23.018730 (2015).
112. Wang, H., Wang, L., Jakob, D. S. & Xu, X. G. Mapping three-dimensional near-field responses with reconstruction scattering-type scanning near-field optical microscopy. *AIP Advances* **7**, 055118, doi:10.1063/1.4984924 (2017).
113. Wang, L. & Xu, X. G. Scattering-type scanning near-field optical microscopy with reconstruction of vertical interaction. *Nature Communications* **6**, 8973, doi:10.1038/ncomms9973 (2015).
114. Xu, X. G. *et al.* One-dimensional surface phonon polaritons in boron nitride nanotubes. *Nature Communications* **5**, 1-6, doi:10.1038/ncomms5782 (2014).
115. Petryayeva, E. & Krull, U. J. Localized surface plasmon resonance: nanostructures, bioassays and biosensing—A review. *Analytica Chimica Acta* **706**, 8-24, doi:10.1016/j.aca.2011.08.020 (2011).
116. Purcell, E. M., Torrey, H. C. & Pound, R. V. Resonance absorption by nuclear magnetic moments in a solid. *Physical Review* **69**, 37, doi:10.1103/physrev.69.37 (1946).
117. Anger, P., Bharadwaj, P. & Novotny, L. Enhancement and quenching of single-molecule fluorescence. *Physical Review Letters* **96**, 113002, doi:10.1103/physrevlett.96.113002 (2006).
118. Park, K.-D., Jiang, T., Clark, G., Xu, X. & Raschke, M. B. Radiative control of dark excitons at room temperature by nano-optical antenna-tip Purcell effect. *Nature Nanotechnology* **13**, 59-64, doi:10.1038/s41565-017-0003-0 (2018).
119. Le Gall, J., Olivier, M. & Greffet, J. J. Experimental and theoretical study of reflection and coherent thermal emissionby a SiC grating supporting a surface-phonon polariton. *Physical Review B* **55**, 10105, doi:10.1103/physrevb.55.10105 (1997).
120. Taubner, T., Keilmann, F. & Hillenbrand, R. Nanomechanical resonance tuning and phase effects in optical near-field interaction. *Nano Letters* **4**, 1669-1672, doi:10.1021/nl0491677 (2004).
121. Ghoshal, A. & Kik, P. G. Excitation of propagating surface plasmons by a periodic nanoparticle array: Trade-off between particle-induced near-field excitation and damping. *Applied Physics Letters* **94**, 251102, doi:10.1063/1.3156862 (2009).
122. Kats, M. A., Yu, N., Genevet, P., Gaburro, Z. & Capasso, F. Effect of radiation damping on the spectral response of plasmonic components. *Optics Express* **19**, 21748-21753, doi:10.1364/oe.19.021748 (2011).
123. Bosman, M. *et al.* Surface plasmon damping quantified with an electron nanoprobe. *Scientific Reports* **3**, 1-7, doi:10.1038/srep01312 (2013).
124. Rivera, N., Christensen, T. & Narang, P. Phonon polaritonics in two-dimensional materials. *Nano Letters* **19**, 2653-2660, doi:10.1021/acs.nanolett.9b00518 (2019).
125. Xue, M. *et al.* Tin diselenide van der Waals materials as new candidates for mid-infrared waveguide chips. *Nanoscale* **11**, 14113-14117, doi:10.1039/c9nr04264d (2019).

126. Li, P. *et al.* Hyperbolic phonon-polaritons in boron nitride for near-field optical imaging and focusing. *Nature Communications* **6**, 1-9, doi:10.1038/ncomms8507 (2015).
127. Giles, A. J. *et al.* Imaging of anomalous internal reflections of hyperbolic phonon-polaritons in hexagonal boron nitride. *Nano Letters* **16**, 3858-3865, doi:10.1021/acs.nanolett.6b01341 (2016).
128. Giles, A. J. *et al.* Ultralow-loss polaritons in isotopically pure boron nitride. *Nature Materials* **17**, 134-139, doi:10.1038/nmat5047 (2018).
129. Wang, H., Li, J., Edgar, J. H. & Xu, X. G. Three-dimensional near-field analysis through peak force scattering-type near-field optical microscopy. *Nanoscale* **12**, 1817-1825, doi:10.1039/c9nr08417g (2020).
130. Filter, R., Qi, J., Rockstuhl, C. & Lederer, F. Circular optical nanoantennas: an analytical theory. *Physical Review B* **85**, 125429, doi:10.1103/physrevb.85.125429 (2012).
131. Wang, T., Li, P., Hauer, B., Chigrin, D. N. & Taubner, T. Optical properties of single infrared resonant circular microcavities for surface phonon polaritons. *Nano Letters* **13**, 5051-5055, doi:10.1021/nl4020342 (2013).
132. Tamagnone, M. *et al.* Ultra-confined mid-infrared resonant phonon polaritons in van der Waals nanostructures. *Science Advances* **4**, eaat7189, doi:10.1126/sciadv.aat7189 (2018).
133. Sumikura, H. *et al.* Highly confined and switchable mid-infrared surface phonon polariton resonances of planar circular cavities with a phase change material. *Nano Letters* **19**, 2549-2554, doi:10.1021/acs.nanolett.9b00304 (2019).
134. Raman, C. V. & Kumar, S. Musical drums with harmonic overtones. *Nature* **104**, 500-500, doi:10.1038/104500a0 (1920).
135. Autore, M. *et al.* Boron nitride nanoresonators for phonon-enhanced molecular vibrational spectroscopy at the strong coupling limit. *Light: Science & Applications* **7**, 17172, doi:10.1038/lsa.2017.172 (2018).
136. Jakob, D. S., Wang, L., Wang, H. & Xu, X. G. Spectro-mechanical characterizations of kerogen heterogeneity and mechanical properties of source rocks at 6 nm spatial resolution. *Analytical Chemistry* **91**, 8883-8890, doi:10.1021/acs.analchem.9b00264 (2019).
137. Li, W., Wang, H., Xu, X. G. & Yu, Y. Simultaneous nanoscale imaging of chemical and architectural heterogeneity on yeast cell wall particles. *Langmuir*, doi:10.1021/acs.langmuir.0c00627 (2020).
138. Mirabella, F. M. *Internal Reflection Spectroscopy: Theory and Applications*. Vol. 15 (CRC Press, 1992).
139. Wang, L. *et al.* Revealing phonon polaritons in hexagonal boron nitride by multipulse peak force infrared microscopy. *Advanced Optical Materials* **8**, 1901084, doi:10.1002/adom.201901084 (2019).
140. Papanu, J. S., Hess, D. W., Soane, D. S. & Bell, A. T. Swelling of poly(methyl methacrylate) thin films in low molecular weight alcohols. *Journal of Applied Polymer Science* **39**, 803-823, doi:10.1002/app.1990.070390404 (1990).
141. Comby, S. & Gunnlaugsson, T. Luminescent lanthanide-functionalized gold nanoparticles: exploiting the interaction with bovine serum albumin for potential sensing applications. *ACS Nano* **5**, 7184-7197, doi:10.1021/nn201992z (2011).
142. Zhang, W., Zhao, Q. & Yuan, J. Porous polyelectrolytes: the interplay of charge and pores for new functionalities. *Angewandte Chemie International Edition* **57**, 6754-6773, doi:10.1002/anie.201710272 (2018).

143. Englander, S., Mayne, L., Bai, Y. & Sosnick, T. Hydrogen exchange: the modern legacy of Linderstrøm-Lang. *Protein Science* **6**, 1101-1109, doi:10.1002/pro.5560060517 (1997).
144. Englander, S. W., Downer, N. W. & Teitelbaum, H. Hydrogen exchange. *Annual Review of Biochemistry* **41**, 903-924, doi:10.1146/annurev.bi.41.070172.004351 (1972).
145. Pearce, F. G., Mackintosh, S. H. & Gerrard, J. A. Formation of amyloid-like fibrils by ovalbumin and related proteins under conditions relevant to food processing. *Journal of Agricultural and Food Chemistry* **55**, 318-322, doi:10.1021/jf062154p (2007).
146. de la Arada, I., Seiler, C. & Mäntele, W. Amyloid fibril formation from human and bovine serum albumin followed by quasi-simultaneous Fourier-transform infrared (FT-IR) spectroscopy and static light scattering (SLS). *European Biophysics Journal* **41**, 931-938, doi:10.1007/s00249-012-0845-1 (2012).
147. Blout, E. R., De Loze, C. & Asadourian, A. The deuterium exchange of water-soluble polypeptides and proteins as measured by infrared spectroscopy. *Journal of the American Chemical Society* **83**, 1895-1900, doi:10.1021/ja01469a028 (1961).
148. Zellner, M. *et al.* Quantitative validation of different protein precipitation methods in proteome analysis of blood platelets. *Electrophoresis* **26**, 2481-2489, doi:10.1002/elps.200410262 (2005).
149. Schroeder, D. D. & Mozen, M. M. Australia antigen: distribution during Cohn ethanol fractionation of human plasma. *Science* **168**, 1462-1464, doi:10.1126/science.168.3938.1462 (1970).
150. Okuda, M., Uemura, Y. & Tatsumi, N. A new method of purifying fibrinogen with both biological and immunological activity from human plasma. *Preparative Biochemistry and Biotechnology* **33**, 239-252, doi:10.1081/pb-120025368 (2003).
151. England, J. L. & Haran, G. Role of solvation effects in protein denaturation: from thermodynamics to single molecules and back. *Annual Review of Physical Chemistry* **62**, 257-277, doi:10.1146/annurev-physchem-032210-103531 (2011).
152. Yoshikawa, H., Hirano, A., Arakawa, T. & Shiraki, K. Effects of alcohol on the solubility and structure of native and disulfide-modified bovine serum albumin. *International Journal of Biological Macromolecules* **50**, 1286-1291, doi:10.1016/j.ijbiomac.2012.03.014 (2012).
153. Block, S. S. *Disinfection, Sterilization, and Preservation*. (Lippincott Williams & Wilkins, 2001).
154. Novak, M. & Vetvicka, V. β-Glucans, history, and the present: immunomodulatory aspects and mechanisms of action. *Journal of Immunotoxicology* **5**, 47-57, doi:10.1080/15476910802019045 (2008).
155. De Smet, R. *et al.* β-Glucan microparticles are good candidates for mucosal antigen delivery in oral vaccination. *Journal of Controlled Release* **172**, 671-678, doi:10.1016/j.jconrel.2013.09.007 (2013).
156. Pan, Y. *et al.* Efficient delivery of antigen to DCs using yeast-derived microparticles. *Scientific Reports* **5**, 10687, doi:10.1038/srep10687 (2015).
157. Lombard, Y., Giaimis, J., Makaya-Kumba, M., Fonteneau, P. & Poindron, P. A new method for studying the binding and ingestion of zymosan particles by macrophages. *Journal of Immunological Methods* **174**, 155-165, doi:10.1016/0022-1759(94)90018-3 (1994).
158. Jawhara, S. *et al.* Modulation of intestinal inflammation by yeasts and cell wall extracts: strain dependence and unexpected anti-inflammatory role of glucan fractions. *PloS One* **7**, e40648, doi:10.1371/journal.pone.0040648 (2012).
159. Fleet, G. H. in *Current Topics in Medical Mycology* 24-56 (Springer, 1985).

160. Cabib, E. & Durán, A. Synthase III-dependent chitin is bound to different acceptors depending on location on the cell wall of budding yeast. *Journal of Biological Chemistry* **280**, 9170-9179, doi:10.1074/jbc.m414005200 (2005).
161. Neuner, B. *et al.* Midinfrared index sensing of pL-scale analytes based on surface phonon polaritons in silicon carbide. *Journal of Physical Chemistry C* **114**, 7489-7491, doi:10.1021/jp9114139 (2010).
162. Berte, R. *et al.* Sub-nanometer thin oxide film sensing with localized surface phonon polaritons. *ACS Photonics* **5**, 2807-2815, doi:10.1021/acsphotonics.7b01482 (2018).
163. Autore, M., Mester, L., Goikoetxea, M. & Hillenbrand, R. Substrate matters: surface-polariton enhanced infrared nanospectroscopy of molecular vibrations. *Nano Letters* **19**, 8066-8073, doi:10.1021/acs.nanolett.9b03257 (2019).
164. Basak, S. & Raman, A. Dynamics of tapping mode atomic force microscopy in liquids: theory and experiments. *Applied Physics Letters* **91**, 064107, doi:10.1063/1.2760175 (2007).
165. Ambrosio, A. *et al.* Mechanical detection and imaging of hyperbolic phonon polaritons in hexagonal boron nitride. *ACS Nano* **11**, 8741-8746, doi:10.1021/acsnano.7b02323 (2017).
166. Ambrosio, A. *et al.* Selective excitation and imaging of ultraslow phonon polaritons in thin hexagonal boron nitride crystals. *Light: Science & Applications* **7**, 1-9, doi:10.1038/s41377-018-0039-4 (2018).
167. Wang, L. *et al.* Generalized Heterodyne Configurations for Photoinduced Force Microscopy. *Analytical Chemistry* **91**, 13251-13259, doi:10.1021/acs.analchem.9b03712 (2019).
168. Wang, H., Janzen, E., Wang, L., Edgar, J. H. & Xu, X. G. Probing mid-infrared phonon polaritons in the aqueous phase. *Nano Letters* **20**, 3986-3991, doi:10.1021/acs.nanolett.0c01199 (2020).
169. Zięba-Palus, J., Nowińska, S. & Kowalski, R. Application of infrared spectroscopy and pyrolysis gas chromatography for characterisation of adhesive tapes. *Journal of Molecular Structure* **1126**, 232-239, doi:10.1016/j.molstruc.2015.11.050 (2016).
170. Fechete, I., Wang, Y. & Védrine, J. C. The past, present and future of heterogeneous catalysis. *Catalysis Today* **189**, 2-27, doi:10.1016/j.cattod.2012.04.003 (2012).
171. Gule, N. P., Begum, N. M. & Klumperman, B. Advances in biofouling mitigation: A review. *Critical Reviews in Environmental Science and Technology* **46**, 535-555, doi:10.1080/10643389.2015.1114444 (2016).
172. Wang, W. *et al.* Bioapplications of DNA nanotechnology at the solid–liquid interface. *Chemical Society Reviews* **48**, 4892-4920, doi:10.1039/c8cs00402a (2019).
173. Ye, C. & Chi, H. A review of recent progress in drug and protein encapsulation: Approaches, applications and challenges. *Materials Science and Engineering: C* **83**, 233-246, doi:10.1016/j.msec.2017.10.003 (2018).
174. López-Lorente, Á. I. & Mizaikoff, B. Mid-infrared spectroscopy for protein analysis: potential and challenges. *Analytical and Bioanalytical Chemistry* **408**, 2875-2889, doi:10.1007/s00216-016-9375-5 (2016).
175. Li, Y. *et al.* in *SENSORS*. 809-813 (IEEE).
176. Eroglu, D. & Kulah, H. Quality factor enhancement of lateral microresonators in liquid media by hydrophobic coating. *Journal of Microelectromechanical Systems* **20**, 1068-1070, doi:10.1109/jmems.2011.2160936 (2011).
177. Oesterschulze, E. *et al.* Tailoring the interface of hybrid microresonators in viscid fluids enhances their quality factor by two orders of magnitude. *Lab on a Chip* **12**, 1316-1319, doi:10.1039/c2lc21260a (2012).

178. Linden, J. & Oesterschulze, E. Improving the quality factor of cantilevers in viscous fluids by the adaptation of their interface. *Applied Physics Letters* **100**, 113511, doi:10.1063/1.3694264 (2012).
179. Akhremitchev, B. B., Sun, Y., Stebounova, L. & Walker, G. C. Monolayer-sensitive infrared imaging of DNA stripes using apertureless near-field microscopy. *Langmuir* **18**, 5325-5328, doi:10.1021/la025700r (2002).
180. Kehr, S. C. *et al.* Anisotropy contrast in phonon-enhanced apertureless near-field microscopy using a free-electron laser. *Physical Review Letters* **100**, 256403, doi:10.1103/physrevlett.100.256403 (2008).
181. Hermann, P. *et al.* Near-field imaging and nano-Fourier-transform infrared spectroscopy using broadband synchrotron radiation. *Optics Express* **21**, 2913-2919, doi:10.1364/oe.21.002913 (2013).
182. Bechtel, H. A., Muller, E. A., Olmon, R. L., Martin, M. C. & Raschke, M. B. Ultrabroadband infrared nanospectroscopic imaging. *Proceedings of the National Academy of Sciences* **111**, 7191-7196, doi:10.1073/pnas.1400502111 (2014).
183. Huth, F., Schnell, M., Wittborn, J., Ocelic, N. & Hillenbrand, R. Infrared-spectroscopic nanoimaging with a thermal source. *Nature Materials* **10**, 352-356, doi:10.1038/nmat3006 (2011).
184. Wagner, M. *et al.* Ultrabroadband nanospectroscopy with a laser-driven plasma source. *ACS Photonics* **5**, 1467-1475, doi:10.1021/acsphotonics.7b01484 (2018).
185. Shannon, C. E. Communication in the presence of noise. *Proceedings of the IRE* **37**, 10-21, doi:10.1109/jrproc.1949.232969 (1949).
186. Cerullo, G. & De Silvestri, S. Ultrafast optical parametric amplifiers. *Review of Scientific Instruments* **74**, 1-18, doi:10.1063/1.1523642 (2003).
187. Ehret, S. & Schneider, H. Generation of subpicosecond infrared pulses tunable between 5.2 μm and 18 μm at a repetition rate of 76 MHz. *Applied Physics B: Lasers and Optics* **66**, 27-30, doi:10.1007/s003400050352 (1998).
188. Ichimura, T., Hayazawa, N., Hashimoto, M., Inouye, Y. & Kawata, S. Tip-enhanced coherent anti-Stokes Raman scattering for vibrational nanoimaging. *Physical Review Letters* **92**, 220801, doi:10.1103/physrevlett.92.220801 (2004).
189. Keilmann, F. & Amarie, S. Mid-infrared frequency comb spanning an octave based on an Er fiber laser and difference-frequency generation. *Journal of Infrared, Millimeter, and Terahertz Waves* **33**, 479-484, doi:10.1007/s10762-012-9894-x (2012).
190. Reed, M. K. & Shepard, M. K. S. Tunable infrared generation using a femtosecond 250 kHz Ti: sapphire regenerative amplifier. *IEEE Journal of Quantum Electronics* **32**, 1273-1277, doi:10.1109/3.511538 (1996).
191. Wagner, M. *et al.* Ultrafast and nanoscale plasmonic phenomena in exfoliated graphene revealed by infrared pump–probe nanoscopy. *Nano Letters* **14**, 894-900, doi:10.1021/nl4042577 (2014).
192. Gilburd, L., Xu, X. G., Bando, Y., Golberg, D. & Walker, G. C. Near-field infrared pump–probe imaging of surface phonon coupling in boron nitride nanotubes. *Journal of Physical Chemistry Letters* **7**, 289-294, doi:10.1021/acs.jpclett.5b02438 (2016).
193. Wang, H., Wang, L. & Xu, X. G. Scattering-type scanning near-field optical microscopy with low-repetition-rate pulsed light source through phase-domain sampling. *Nature Communications* **7**, 1-8, doi:10.1038/ncomms13212 (2016).
194. Brehm, M., Schliesser, A. & Keilmann, F. Spectroscopic near-field microscopy using frequency combs in the mid-infrared. *Optics Express* **14**, 11222-11233, doi:10.1364/oe.14.011222 (2006).

195. Link, S. & El-Sayed, M. A. Optical properties and ultrafast dynamics of metallic nanocrystals. *Annual Review of Physical Chemistry* **54**, 331-366, doi:10.1146/annurev.physchem.54.011002.103759 (2003).
196. Huang, B., Bates, M. & Zhuang, X. Super-resolution fluorescence microscopy. *Annual Review of Biochemistry* **78**, 993-1016, doi:10.1146/annurev.biochem.77.061906.092014 (2009).
197. Parida, B., Iniyan, S. & Goic, R. A review of solar photovoltaic technologies. *Renewable and Sustainable Energy Reviews* **15**, 1625-1636, doi:10.1016/j.rser.2010.11.032 (2011).
198. Klar, T. A. & Hell, S. W. Subdiffraction resolution in far-field fluorescence microscopy. *Optics Letters* **24**, 954-956, doi:10.1364/ol.24.000954 (1999).
199. Gustafsson, M. G. L. Nonlinear structured-illumination microscopy: wide-field fluorescence imaging with theoretically unlimited resolution. *Proceedings of the National Academy of Sciences* **102**, 13081-13086, doi:10.1073/pnas.0406877102 (2005).
200. Rust, M. J., Bates, M. & Zhuang, X. Sub-diffraction-limit imaging by stochastic optical reconstruction microscopy (STORM). *Nature Methods* **3**, 793-796, doi:10.1038/nmeth929 (2006).
201. Betzig, E. *et al.* Imaging intracellular fluorescent proteins at nanometer resolution. *Science* **313**, 1642-1645, doi:10.1126/science.1127344 (2006).
202. Hess, S. T., Girirajan, T. P. K. & Mason, M. D. Ultra-high resolution imaging by fluorescence photoactivation localization microscopy. *Biophysical Journal* **91**, 4258-4272, doi:10.1529/biophysj.106.091116 (2006).
203. Remington, S. J. Green fluorescent protein: a perspective. *Protein Science* **20**, 1509-1519, doi:10.1002/pro.684 (2011).
204. Mikhnenko, O. V., Blom, P. W. M. & Nguyen, T.-Q. Exciton diffusion in organic semiconductors. *Energy & Environmental Science* **8**, 1867-1888, doi:10.1039/c5ee00925a (2015).
205. Treat, N. D. *et al.* Interdiffusion of PCBM and P3HT reveals miscibility in a photovoltaically active blend. *Advanced Energy Materials* **1**, 82-89, doi:10.1002/aenm.201000023 (2011).
206. Collins, B. A., Tumbleston, J. R. & Ade, H. Miscibility, crystallinity, and phase development in P3HT/PCBM solar cells: toward an enlightened understanding of device morphology and stability. *Journal of Physical Chemistry Letters* **2**, 3135-3145, doi:10.1021/jz2014902 (2011).
207. Bruno, A., Reynolds, L. X., Dyer-Snaith, C., Nelson, J. & Haque, S. A. Determining the exciton diffusion length in a polyfluorene from ultrafast fuorescence measurements of polymer/fullerene blend films. *Journal of Physical Chemistry C* **117**, 19832-19838, doi:10.1021/jp404985q (2013).
208. Sim, M. *et al.* Dependence of Exciton diffusion length on crystalline order in conjugated polymers. *Journal of Physical Chemistry C* **118**, 760-766, doi:10.1021/jp409776s (2014).
209. Irkhin, P. & Biaggio, I. Direct imaging of anisotropic exciton diffusion and triplet diffusion length in rubrene single crystals. *Physical Review Letters* **107**, 017402, doi:10.1103/physrevlett.107.017402 (2011).

APPENDIX I PF-SNOM Technical Details

Technical drawing

Figure A1 shows the technical drawing of the PF-SNOM setup:

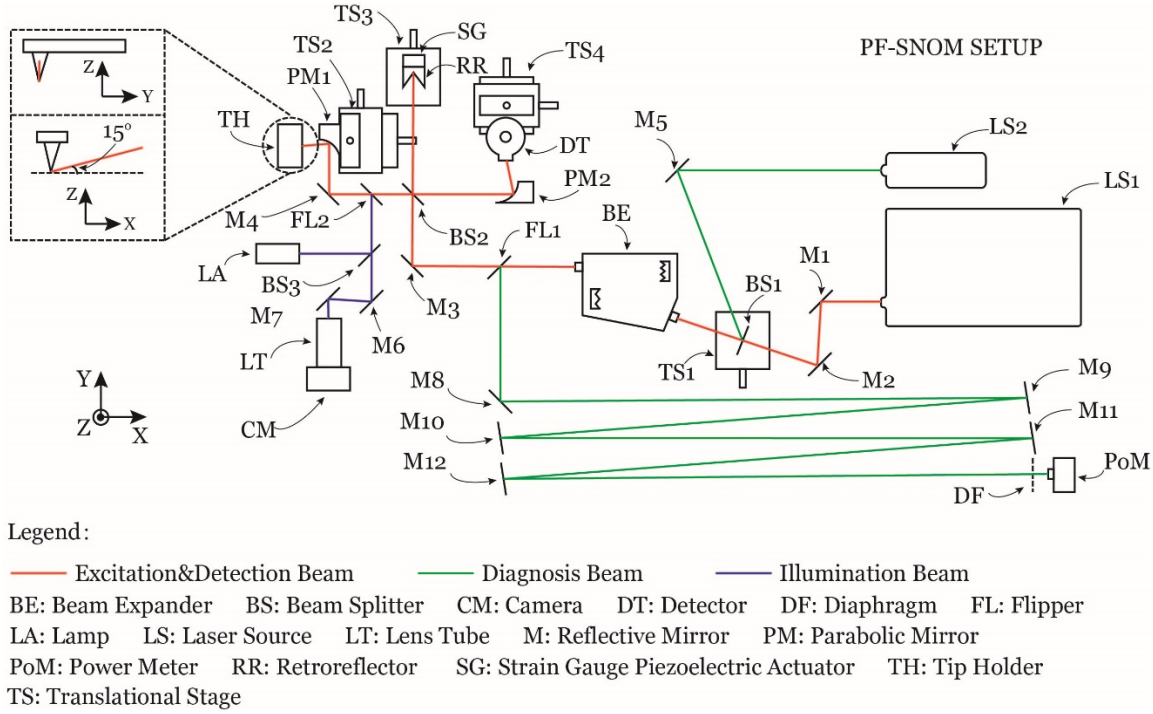

Figure A1 Technical drawing of PF-SNOM setup.

The parts or similar parts used in PF-SNOM are listed in Table A1.

Table A1 Parts in PF-SNOM setup.

Part name	Part number	Vendor & note
BE	BE06R	Thorlabs, beam expander
BS1		Thorlabs, long pass dichroic mirror
BS2	BSW510	Thorlabs, 50/50 mid-infrared beam splitter
BS3	N/A	Glass coverslip
CM	DCC1545M	Thorlabs, CMOS camera
DT	N/A	MCT detector, KLD series, Kolmartech
DF	ID25	Thorlabs, post-mounted iris diaphragms
FL1	FM90	Thorlabs. Mount with a silver mirror PF10-03-P01
FL2	FM90	Thorlabs. Mount with a pellicle beam splitter BP145B4
LA	QTH10	Thorlabs, quartz tungsten-halogen lamp
LS1	N/A	Daylight Solutions, MIRcat
LS2	HNLS008R	Thorlabs, HeNe laser

Part name	Part number	Vendor & note
LT	SM1L40	Thorlabs, lens tubes
M1-M4	PF10-03-M02	Thorlabs, mid-infrared enhanced gold mirror
M5-M12	PF10-03-P01	Thorlabs, silver mirror
PM	#37-296	Edmund Optics, gold 90° off-axis mirror with 1' RFL
PoM	N/A	Infrared power meter
RR		Thorlabs. Mounted on a piezo actuator PA3JEAW
SG	N/A	Thorlabs, NF15AP25, K-Cube piezo controller and strain gauge reader
TH	N/A	Bruker Multimode 8 AFM
TS	XR50C	Thorlabs

Data acquisition

The data acquisition is achieved through two two-channel data acquisition cards. One is the two-channel PXI-5122 data acquisition card (National Instruments) with trigger and the other is the two-channel PXI-4461 data acquisition card (National Instruments) for analog inputs. For simplicity, input channels are demoted as I1 and I2 for PXI5122, and I3 and I4 for PXI 4461. In PF-SNOM experiment, the deflection curve (A-B signal) from the AFM quadrant detector is routed to I1, the optical signal from the MCT detector is routed to I2, and X-piezo and Y-piezo voltages from AFM are connected to I3 and I4. The same trigger at peak force tapping frequency is shared for all inputs. Using customized LabVIEW code, the data are stored in an n by m 2D matrix in ASCII format, which is shown in Figure A2. The first two columns are used to store X and Y voltage data, and the rest columns are used to store deflection data $D(t)$ and optical data $S(t)$ in the time domain. X voltage and $D(t)$ data are stored in odd rows, while Y voltage and $S(t)$ data are stored in even rows. Each pair of odd/even rows shares the same timestamp.

X voltage	X voltage	$D(1)$	$D(2)$	$D(3)$	$\ldots\ldots^{m}$
Y voltage	Y voltage	$S(1)$	$S(2)$	$S(3)$	
n ⋮					

Figure A2 Structure of PF-SNOM raw data.

Usually, m is around 200 (with 50 MHz sampling rate and the average of 60). Note that well-defined snap-in and peak force points must be contained in $D(t)$ data since they are key to retrieve accurate tip-sample distances. The row number n is determined by the scanning time of one frame, which is close to 200000 if one uses a 0.1 Hz scan rate to capture a 256×256 pixel-size image. The raw data is then processed by a MATLAB code shown below:

```
clear
warning('off','all')
data = load('PFSNOM_1425_0.1Hz_60mean.txt'); % specify the raw data name
dim = size(data);
dim1 = dim(1);

%%seperate data files
X_data = (data(1:2:end,1)+data(1:2:end,2))/2;
Y_data = (data(2:2:end,1)+data(2:2:end,2))/2;
AB_data = data(2:2:end,3:end); %even rows are AFM A-B data and Yscan data
SL_data = data(1:2:end,3:end); %odd rows are scattering light data and Xscan data
dim = size(AB_data);
dim2 = dim(2);

X_data_tr = ones(round(dim1/4)+2000,1); X_data_rt = ones(round(dim1/4)+2000,1); % generate arrays to store separated trace and retrace data
Y_data_tr = ones(round(dim1/4)+2000,1); Y_data_rt = ones(round(dim1/4)+2000,1);
AB_data_tr = ones(round(dim1/4)+2000,dim2); AB_data_rt = ones(round(dim1/4)+2000,dim2);
SL_data_tr = ones(round(dim1/4)+2000,dim2); SL_data_rt = ones(round(dim1/4)+2000,dim2);
a = 1; b = 1;
for n = 1:dim1/2-1
   if X_data(n+1) >= X_data(n)
      X_data_tr(a) = X_data(n);
      Y_data_tr(a) = Y_data(n);
      AB_data_tr(a,:) = AB_data(n,:);
      SL_data_tr(a,:) = SL_data(n,:);
      a = a + 1;
   else
      X_data_rt(b) = X_data(n);
      Y_data_rt(b) = Y_data(n);
      AB_data_rt(b,:) = AB_data(n,:);
      SL_data_rt(b,:) = SL_data(n,:);
      b = b + 1;
   end
```

```
end

X_data_tr(a:end) = [];
Y_data_tr(a:end) = [];
AB_data_tr(a:end,:) = [];
SL_data_tr(a:end,:) = [];

X_data_rt(b:end) = [];
Y_data_rt(b:end) = [];
AB_data_rt(b:end,:) = [];
SL_data_rt(b:end,:) = [];

X_data = X_data_tr;
Y_data = Y_data_tr;
AB_data = AB_data_tr;
SL_data = SL_data_tr;
dim = size(X_data);
dim1 = dim(1);

%%start processing
AB_use = mean(AB_data(500:1000,:)); %pick 500 sets of D(t) curves to get an averaged D(t) curve to retrieve tip-sample distance information
TSD = TSDrecover(AB_use, 31.47, 150, 3.906, 5);
Snap_ix = find(TSD == 0);
x = 1:round(dim2/5); %linear background fit range, starting from the first quarter
gap = linspace(max(x), Snap_ix, 6); % 6 values defines 5 ranges
gap = round(gap);
Dx = TSD(1:Snap_ix)'; %fit range for exponential decay

slope = zeros(1,dim2); intercept = zeros(1,dim2); background = zeros(dim1, dim2);
signal_gap1 = zeros(dim1, 1); signal_gap2 = zeros(dim1, 1); signal_gap3 = zeros(dim1, 1); signal_gap4 = zeros(dim1, 1);signal_gap5 = zeros(dim1, 1);
psignal_gap1 = zeros(dim1, 1); psignal_gap2 = zeros(dim1, 1); psignal_gap3 = zeros(dim1, 1); psignal_gap4 = zeros(dim1, 1);psignal_gap5 = zeros(dim1, 1);
vsignal = zeros(dim1, Snap_ix); pvsignal = zeros(dim1, Snap_ix); decay_b = zeros(dim1, 1); decay_a = zeros(dim1, 1);

for n = 1:dim1
   y = SL_data(n, x);
   f = polyfit(x, y, 1);
   slope(n) = f(1);
   intercept(n) = f(2);
   background(n,:)= (1:dim2).*slope(n)+intercept(n);
   signal_gap1(n) = (mean(SL_data(n,gap(1):gap(2))-background(n,gap(1):gap(2))));
   signal_gap2(n) = (mean(SL_data(n,gap(2):gap(3))-background(n,gap(2):gap(3))));
   signal_gap3(n) = (mean(SL_data(n,gap(3):gap(4))-background(n,gap(3):gap(4))));
   signal_gap4(n) = (mean(SL_data(n,gap(4):gap(5))-background(n,gap(4):gap(5))));
   signal_gap5(n) = (mean(SL_data(n,gap(5):gap(6))-background(n,gap(5):gap(6))));
   vsignal(n, :) = SL_data(n, 1:Snap_ix) - background(n, 1:Snap_ix);
end
```

```
%% start imaging results
dt = delaunayTriangulation(X_data,Y_data) ;
tri = dt.ConnectivityList ;
xi = dt.Points(:,1) ; yi = dt.Points(:,2) ;
F1 = scatteredInterpolant(X_data, Y_data,  -(signal_gap1)) ; % a minus sign to convert
data to positive
F2 = scatteredInterpolant(X_data, Y_data,  -(signal_gap2)) ;
F3 = scatteredInterpolant(X_data, Y_data,  -(signal_gap3)) ;
F4 = scatteredInterpolant(X_data, Y_data,  -(signal_gap4)) ;
F5 = scatteredInterpolant(X_data, Y_data,  -(signal_gap5)) ;

z1=F1(xi,yi);
z2=F2(xi,yi);
z3=F3(xi,yi);
z4=F4(xi,yi);
z5=F5(xi,yi);

figure
subplot(3,2,1)
plot(TSD(1:Snap_ix),vsignal(24000,:),'.')

subplot(3,2,2)
pbaspect([1,1,1]);
trisurf(tri,xi,yi,z1)
view(2)
shading interp
colormap(jet);
colorbar;
title(['d =' ,num2str(TSD(round((gap(1)+gap(2))/2))), 'nm'])

subplot(3,2,3)
pbaspect([1,1,1]);
trisurf(tri,xi,yi,z2)
view(2)
shading interp
colormap(jet);
colorbar;
title(['d =' ,num2str(TSD(round((gap(2)+gap(3))/2))), 'nm'])

subplot(3,2,4)
pbaspect([1,1,1]);
trisurf(tri,xi,yi,z3)
view(2)
shading interp
colormap(jet);
colorbar;
title(['d =' ,num2str(TSD(round((gap(3)+gap(4))/2))), 'nm'])

subplot(3,2,5)
```

```
pbaspect([1,1,1]);
trisurf(tri,xi,yi,z4)
view(2)
shading interp
colormap(jet);
colorbar;
title(['d =' ,num2str(TSD(round((gap(4)+gap(5))/2))), 'nm'])

subplot(3,2,6)
pbaspect([1,1,1]);
trisurf(tri,xi,yi,z5)
view(2)
shading interp
colormap(jet);
colorbar;
title(['d =' ,num2str(TSD(round((gap(5)+gap(6))/2))), 'nm'])
```

The function TSDrecover used in the MATLAB code is a customized function to retrieve the tip-sample distance from the $D(t)$ curve, and is shown below:

```
function [TSD_time] = TSDrecover(PF_curve, DF_sens, PF_amp, PF_freq, SP_rate)
% Input unit: PF_curve in V, DF_sens in nm/V, PF_amp in nm, PF_freq in kHz, SP_rate in MHz
PF_freq = PF_freq .* 1000;
SP_rate = SP_rate .* 1e6;

Peak_position = find(PF_curve == max(PF_curve));
Peak_position = Peak_position(1); % in case that there are more than one maxima in the tip_deflection plot
Snapin_position = find(PF_curve == min(PF_curve(10:Peak_position)));
Snapin_position = Snapin_position(1);
phase = pi/2 - 2*pi*PF_freq*Peak_position/SP_rate;
number = 1:length(PF_curve);
TSD_time = PF_amp.*sin(2.*pi.*number.*PF_freq./SP_rate + phase);
TSD_time = PF_amp - TSD_time + DF_sens.*(PF_curve - PF_curve(Snapin_position));
TSD_time = TSD_time - TSD_time(Snapin_position);
end
```

Finally, six output panels are shown in Figure A3.

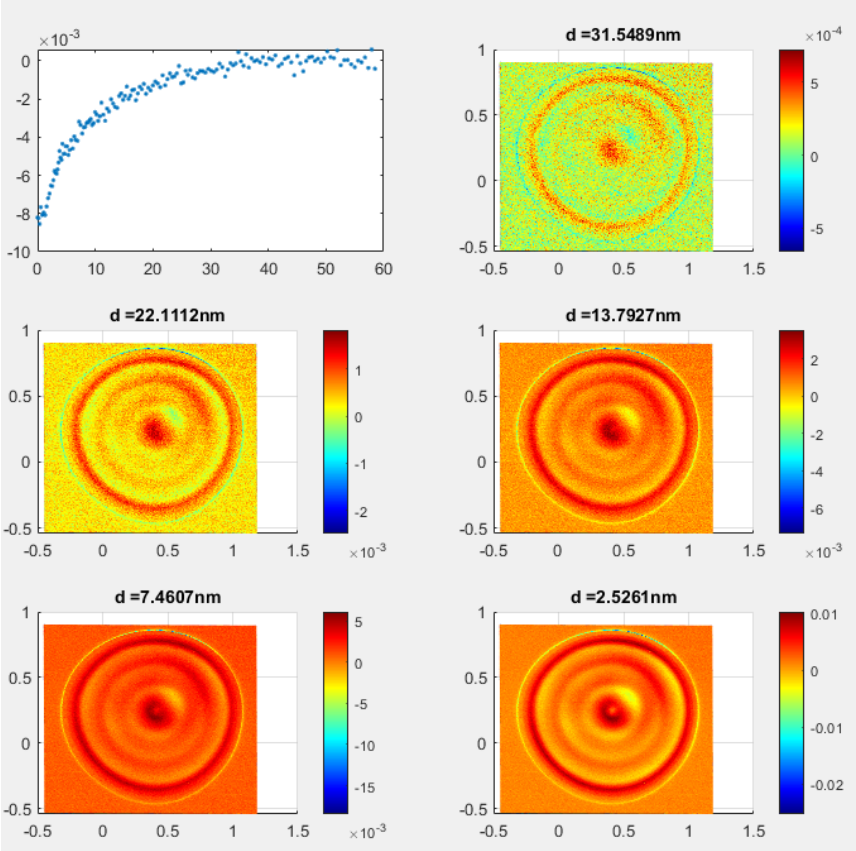

Figure A3 Output images from the MATLAB code.

APPENDIX II LiPFIR Technical Details

Technical Drawing

The technical drawing of LiPFIR is shown in Figure A4.

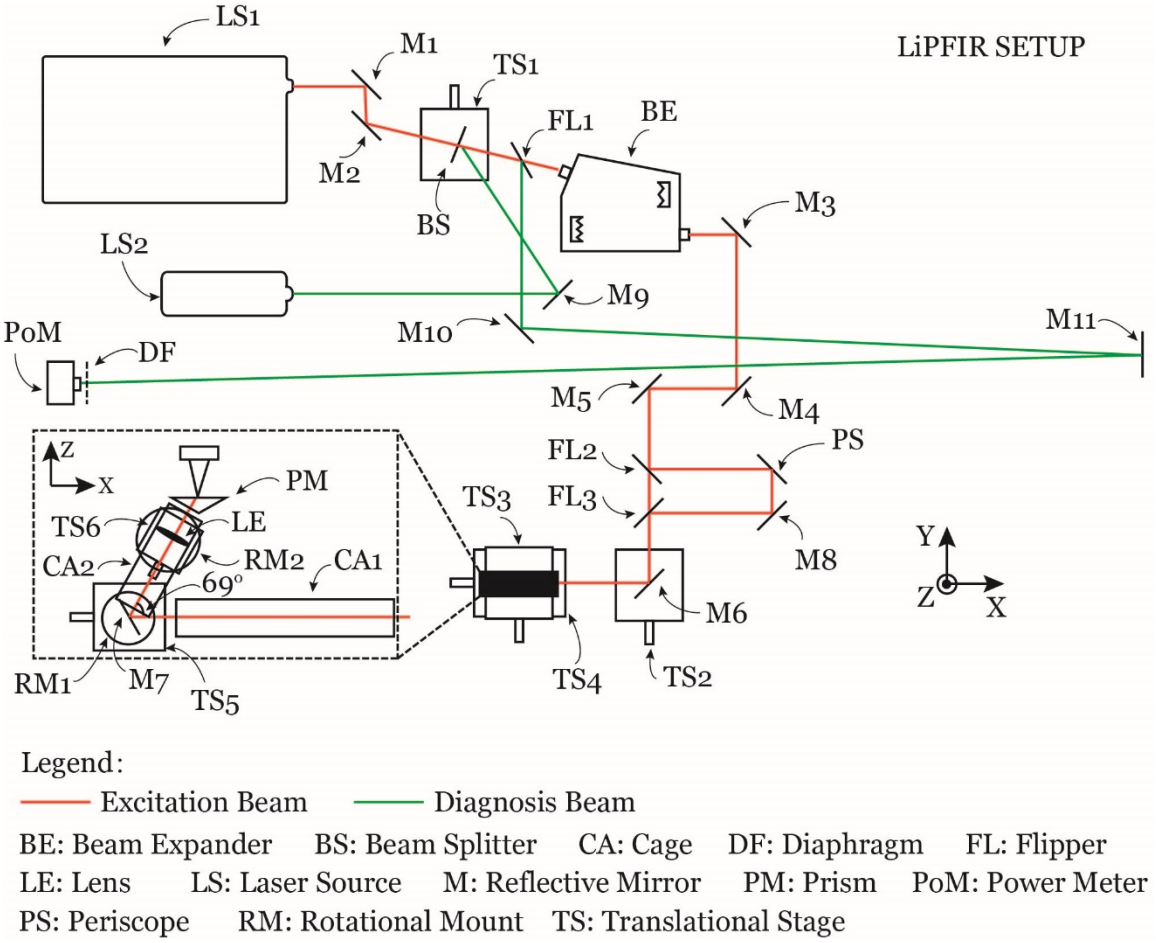

Figure A4 Technical drawing of LiPFIR setup.

The parts or similar parts used in LiPFIR are listed in Table A2.

Table A2 Parts in LiPFIR setup.

Part name	Part number	Vendor & note
BE	BE04R	Thorlabs, beam expander
BS		Thorlabs, long pass dichroic mirror
CA	N/A	Thorlabs, 30 mm cage system
DF	ID25	Thorlabs, post-mounted iris diaphragms
FL1	FM90	Thorlabs. Mount with a silver mirror PF10-03-P01

Part name	Part number	Vendor & note
FL2-FL3	FM90	Thorlabs. Mount with a mid-infrared enhanced gold mirror PF10-03-M02
LE	#69-637	Edmund Optics, germanium plano-convex lens with 25 mm FL
LS1	N/A	Daylight Solutions, MIRcat
LS2	HNLS008R	Thorlabs, HeNe laser
LT	SM1L40	Thorlabs, lens tubes
M1-M8	PF10-03-M02	Thorlabs, mid-infrared enhanced gold mirror
M9-M11	PF10-03-P01	Thorlabs, silver mirror
PM	N/A	20×15 mm germanium with a wedge angle of 22°
PoM	N/A	Infrared power meter
PS	N/A	Composed of two right-angle reflective prisms, Thorlabs, PS704
RM1	RP01	Thorlabs
RM2	PRM1	Thorlabs
TS1, TS5-TS6	XR50C	Thorlabs. TS6 is driven by a motorized actuator, Thorlabs ZST213
TS2-TS4	LNR25M, LNR25D, LNR50D	Thorlabs. All stages are driven by trapezoidal stepper motor actuator Thorlabs DRV225

Laser alignment

Laser alignment for opaque Ge prism is achieved by motorized stages TS2-TS4 and TS6 in XYZ directions. Among them, TS2 and TS3 are always synchronized to maintain a constant incident angle in the XY-plane. The XZ incident angle is fixed at 21° for Ge prism by manually adjusting RM1 and RM2. To roughly place the beam on to AFM tip, one can place the AFM tip holder on the sample stage and remove the Ge lens and Ge prism to let co-linearized HeNe beam shine on the cantilever by adjusting XY stages (TS2-TS4). Then, the Ge lens and prism should be put back into their original positions for further alignment.

Before LiPFIR measurement, it is desirable to firstly use a “standard” sample (e.g. spin-coated PS:PMMA blend with a strong 1725 cm^{-1} absorption) or first locate a micrometer-sized sample patch on the substrate by using a top optical camera. In the air, engage the AFM tip onto the sample. After the engage is finished, retract the tip back to free space by

roughly 40 μm. Perform the thermal tune to the cantilever and find the first mechanical frequency Ω of the cantilever. Then, tune the laser to one of the strong sample absorptions (e.g. 1725 cm^{-1} for PS:PMMA blends) and tune the repetition rate to match Ω. Note that the repetition rate of QCL cannot be tuned to exactly match Ω, usually, a small offset exists between actual Ω and QCL repetition rate Ω_L. Route A-B signal from AFM into a lock-in amplifier (HFLi or MFLi, Zurich instruments) and manually input the demodulation frequency as Ω_L.

Next, turn on the laser and monitor the temporal change of amplitude of first harmonic. If the focus spot is close to the cantilever, the photoacoustic wave generated by the sample's periodic photothermal expansion will kick the cantilever to oscillate as well. Adjusting TS2-TS4, and TS6 to maximize the demodulated amplitude. Note that multiple local maxima may exist for multiple XYZ stage combinations, so the adjustment of XYZ stage positions can be iterative. One of the traits of the global maximum is it is sensitive to 10 μm displacement in all XYZ directions, an obvious first harmonic amplitude drop should be observed when offset one of the stages by only 10 μm. Another rule of thumb is if there are multiple maxima for different Z location, always choose the lowest Z.

Once the focus spot has been determined, one can replace the standard sample with a sample of interest (Note that when changing the sample, retract the AFM tip more than 40 μm to avoid tip scratching!) or move the XY stage of Bioscope Catalyst to find a proper location to measure. The same alignment procedure could be repeated once more if one exchanges the sample or apply a large XY offset to the AFM sample stage. Nevertheless, the adjustment of XYZ stages (TS2-TS4, and TS6) should be mild and much easier this time. The final XYZ stages adjustment could be made when in peak force tapping, the LiPFIR signal can be directly used for signal optimization in this case.

Curriculum Vitae

Haomin Wang

ADDRESS & CONTACT	6 East Packer Avenue, Bethlehem, PA 18015, USA	Mobile: 1-484-774-0098 Email: haw515@lehigh.edu

EDUCATION	Sept. 2015–Aug. 2020 (Expected)	Ph. D. of chemistry. Department of Chemistry, Lehigh University, Bethlehem, PA, USA Research: AFM-based light microscopy and spectroscopy Advisor: Prof. Xiaoji G. Xu
	Sept. 2011– July 2015	B. S. of chemistry, GPA 3.45/4, Peking University, Beijing, China Research: Fabrication and characterization of carbon nanoelectrodes, liquid/liquid interfacial electron/ion transfer Advisor: Prof. Yuanhua Shao

PUBLICATIONS *As first author (* stands for equal contribution):*

1. **Wang, H.**, Wang, L., Shang, Y., Yazdanparast Tafti, S., Cao, W., Ning, Z., Zhang, X. F., & Xu, X. G. (2020). Peak force visible microscopy. Submitted.
2. **Wang, H.**, González-Fialkowski, J. M., Li, W., Yu, Y., & Xu, X. G. (2020). Liquid-phase peak force infrared microscopy. Under review.
3. **Wang, H.**, Wang, L., Janzen, E., Edgar, J. H., & Xu, X. G. (2020). Total internal reflection peak force infrared microscopy. Under review.
4. Li, W., **Wang, H.***, Xu, X. G., & Yu, Y. (2020). Simultaneous nanoscale imaging of chemical and architectural heterogeneity on yeast cell wall particles. *Langmuir,* 2020, 36, 22, 6169–6177.
5. **Wang, H.**, Janzen, E., Wang, L., Edgar, J. H., & Xu, X. G. (2020). Probing mid-infrared phonon polaritons in the aqueous phase. *Nano Letters,* 2020, 20, 5, 3986–3991.
6. **Wang, H.**, Li, J., Edgar, J. H., & Xu, X. G. (2020). Three-dimensional near-field analysis through peak force scattering-type near-field optical microscopy. *Nanoscale,* 2020, 12, 1817-1825.
7. **Wang, H**., Wang, L., Jakob, D. S., & Xu, X. G. (2018). Tomographic and multimodal scattering-type scanning near-field optical microscopy with peak force tapping mode. *Nature Communications*, 9(1), 2005.
8. **Wang, H.**, Wang, L., Jakob, D. S., & Xu, X. G. (2017). Mapping three-dimensional near-field responses with reconstruction scattering-type scanning near-field optical microscopy. *AIP Advances*, 7(5), 055118.

9. **Wang, H.**, Wang, L., & Xu, X. G. (2016). Scattering-type scanning near-field optical microscopy with low-repetition-rate pulsed light source through phase-domain sampling. *Nature Communications*, 7, 13212.

As co-author:

1. Jakob, D. S., **Wang, H.**, & Xu, X. G. (2020). Peak Force Infrared – Kelvin Probe Force Microscopy. *Angewandte Chemie Int. Ed.,* In press.

2. Jakob, D. S., **Wang, H.**, & Xu, X. G. (2020). Pulsed force kelvin probe force microscopy. *ACS Nano,* 14, 4, 4839−4848.

3. Wang, L., Wagner, M., **Wang, H.**, Pau-Sanchez, S., Li, J., Edgar, J. H., & Xu, X. G. (2019). Revealing phonon polaritons in hexagonal boron nitride by multipulse peak force infrared microscopy. *Advanced Optical Materials*. 8(5), 1901084.

4. Wang, L., Jakob, D. S., **Wang, H.**, Apostolos, A., Pires, M. M., & Xu, X. G. (2019). Generalized heterodyne configurations for photoinduced force microscopy. *Analytical Chemistry*, 91(20), 13251-13259.

5. Jakob, D. S., Wang, L., **Wang, H.**, & Xu, X. G. (2019). Spectro-mechanical characterizations of kerogen heterogeneity and mechanical properties of source rocks at 6 nm spatial resolution. *Analytical Chemistry*. 91(14), 8883-8890.

6. Wang, L., **Wang, H.**, Vezenov, D., & Xu, X. G. (2018). Direct measurement of photoinduced force for nanoscale infrared spectroscopy and chemical-sensitive imaging. *The Journal of Physical Chemistry C*, 122(41), 23808-23813.

7. Wang, L., **Wang, H.**, Wagner, M., Yan, Y., Jakob, D. S., & Xu, X. G. (2017). Nanoscale simultaneous chemical and mechanical imaging via peak force infrared microscopy. *Science Advances*, 3(6), e1700255.

8. Zhang, X., **Wang, H.**, Morris, C., Gu, C., Li, M., Baker, L., & Shao, Y. (2016). Probing electron-transfer and ion-transfer coupling processes at liquid/liquid interfaces with pipette electrodes. *ChemElectroChem*, 3(12), 2153-2159.

FELLOWSHIPS

Horner Fellowship, Lehigh University, 2018
Pangu Fellowship, CCME, Peking University, 2014

CONFERENCES

Talk, PITTCON Conference & Expo, Philadelphia, 2019

Attendee, Workshop: Optical Scanning Probe Microscopy of 2D Quantum Materials, CNS, Harvard University, 2018

Talk, 256th ACS National Meeting & Exposition, Boston, 2018

Poster, ACS Mid Atlantic Regional Meeting, Bethlehem, 2018

Attendee, 252nd ACS National Meeting & Exposition, Philadelphia, 2016